Transport Processes in 2-D Plasma-Liquid Systems

by

Janis Ching-Yin Lai

A dissertation submitted in partial fulfillment
of the requirements for the degree of
Doctor of Philosophy
(Nuclear Engineering and Radiological Sciences)
in the University of Michigan
2019

Doctoral Committee:

Professor John E. Foster, Chair
Assistant Professor José F. Alfaro
Dr. Isaiah M. Blankson, NASA Glen
Professor Mark J. Kushner
Professor Annalisa Manera

It's a dangerous business, Frodo, going out your door... You step into the Road, and if you don't keep your feet, there is no knowing where you might be swept off to.

J.R.R. Tolkien, Lord of the Rings

Janis Ching-Yin Lai

janislai@umich.edu

ORCID iD: 0000-0002-9806-0591

Acknowledgments

First, I would like to express my deepest gratitude to my advisor Professor John Foster, whose passion for scientific discovery, intellectual curiosity and vast knowledge have been a constant inspiration for me over the past six years. I am especially grateful for his guidance, assistance and conversation during many lengthy experiments.

Secondly, I would like to thank my committee members, Professor Mark Kushner, Professor Annalisa Manera, Professor José Alfaro and Dr. Isaiah Blankson for their valuable support throughout my time at Michigan.

Some of the experimental work in this dissertation was the result of collaborative research efforts. The construction of 2-D discharge cells would not be possible without the machining expertise and guidance of David Carter, James Tice and Scott Webster at the LSA Scientific Instrument Shop. Dr. Victor Petrov from the Experimental and Computational Multiphase Flow Laboratory in Michigan provided preliminary particle image velocimetry (PIV) measurements reported in Chapter. 6 and advised us on our subsequent PIV set up. The supply of lake water from Lake Erie and quantification of levels of microcystin-LR using ELISA tests were generously supported by Dr. Alicia Ritzenthaler and Dr. Tim Davis from NOAA - Great Lakes Environmental Research Laboratory in Ann Arbor. Samples preparation and preliminary HPLC analysis reported in Chapter. 10 were assisted by Tom Yavaraski from the Department of Civil and Environmental Engineering.

I also want to thank my past and present labmates who have supported me through challenging courses and shared many fun adventures during conferences. Special thanks to Ken-

neth Engeling, who was always willing to help me with my experiments; Yao Kovach, who always shared her course notes with me and cheered me on before conference presentations; and Joseph Groele, who sat with me for hours when we waited for COD measurements. I would also like to thank my first undergraduate assistants Levi Welch and KayCe Duggan for the enthusiasm and talent they brought weekly over the past year.

This work will not be possible if not for the financial support from various institutions. This work was supported by the National Science Foundation and the Department of Energy. Tuition and travel funds were also provided by the Rackham Graduate School and the Department of Nuclear Engineering and Radiological Sciences. I would like to thank these institutions for their generous support.

Next, I would like to thank assistant dean Dr. John Godfrey for his invaluable conversations and guidance during my tenure at Graduate Rackham International. Founding GRIN was a profound experience in both personal growth and leadership, and I am grateful for the opportunity to speak for my fellow graduate students as a student leader. It would be remiss if I do not thank everyone who contributed significant amount of time and effort in GRIN, especially Abhinav, Nitin, Mina, Kumar, Kunisuke, Max, and Andrew.

It is impossible to reach the finish line of graduate school without the support of my friends. Abhinav, thank you for pushing me to adopt a grow mindset, and all the work sessions involving Sushi Town and beef rice. Kevin, thank you for cooking countless dishes with me, in real life and in Overcooked. Dorothy, thank you for being there for me all the time even though there are more than 9,000 miles between us. Rex, thank you for always listening to me and our annual Disney trips. Martin and Aster, you guys are my extended family and I am eternally grateful for that. Amina, Lesley and Rosa, thank you for being my support system here in Michigan. Above all, I would like to thank Juliusz, for being the best sounding board there is.

Special thanks belong to all the furry companions I have the privilege to care for, Lyra, Vela, Marigold and Theodore, who always remind me to go outside to smell the grass and feel the sun.

Last but not least, I am forever indebted to my parents, Keith and Candy, who have always believed in me to forge my own path and supported me every step of the way.

Table of Contents

List of Tables

List of Figures

Abstract

The interaction of atmospheric pressure plasmas with liquids is currently being investigated for a wide range of environmental remediation applications, such as drinking water and wastewater treatments. Plasmas in contact with water can drive advanced oxidation processes at the gas-liquid interface directly and indirectly in the bulk liquid. These processes produce reactive species, such as hydroxyl radicals, ozone and hydrogen peroxide, that can degrade organic pollutants and microorganisms in water. As such, maximizing the plasma-liquid interfacial contact area can optimize the production and transport of these reactive species into the target liquid. The production of plasma in gas bubbles constitutes one approach to both increase the plasma-liquid contact area and reduce the electric field required for breakdown, thus optimizing the energy efficiency of production of plasma-derived reactive species in liquids.

However, bubbles in liquids do not lend itself well to optical diagnostics. The surrounding liquid obscures the bubble volume, which prevents the direct interrogation of gas phase plasma parameters, such as the characterization of plasma species using optical emission spectroscopy. In addition, imaging of spherical bubbles inherently projects 3-D structure inside the bubble onto a 2-D plane, and leads to the loss of inherent spatial features that might provide valuable insight. A 2-D discharge cell was designed and constructed to enable direct simultaneous imaging of the liquid, gas and interface region. A thin layer of liquid is trapped between two clear plates, in which a single bubble is injected using a precision syringe. Plasmas are excited inside the bubble using nanosecond pulsed power sup-

plies.

Chemical probes were used in the 2-D cell to visualize the production and transport of plasma-derived species at the interface and in the bulk liquid. We observed the formation of large-scale circulation patterns, which drove the transport of oxidative species, such as hydroxyl radicals, and induced fluid mixing. Absorption spectrophotometry was used with a chemical probe to characterize the production of ozone in water, and led to the observation of plasma-driven capillary waves on the bubble surface. These traveling waves distorted the shape of the air bubble into a star polygon. The resulting shape was found to be dependent on bubble diameter and plasma excitation frequency. The bubble surface deformation led to self-organization of subsequent plasma discharges. This coupling between self-organization of plasma and interfacial capillary waves appeared synergistic.

Bulk liquid conditions can also impact discharge conditions and resulting streamer propagation in bubbles. We investigated the effects of liquid conductivity on discharge morphology inside the bubble and plasma-driven fluid flow in the bulk liquid. Fast ICCD imaging showed that high liquid conductivity can increase refraction of electric field lines at the interface and reduce charge relaxation time, which led to the development of intense surface hugging streamers. Energy dissipation scaled positively with liquid conductivity as well, and can lead to increased thermal effects at the interface at high conductivity. Local temperature gradients can induce surface tension gradients in the liquid and drive Marangoni flow. Plasma-driven flow was measured using particle image velocimetry (PIV), and a positive correlation was found between liquid conductivity and flow speeds in the bulk. This result points to the possibility of high contribution of Marangoni effects in plasma-driven fluid flow.

Chapter 1

Introduction

The physics and chemistry at interfaces in plasma-liquid systems can be studied by reducing dimensionality of such systems from three to two dimensions.

1.1 Introduction

Plasma is commonly termed the fourth state of matter. Consider the first phase, solid, at atmospheric pressure. At high density and low temperature, its constituent molecules are tightly packed. As temperature increases, molecules gain energy and undergo a phase transition to become a liquid. In this state, molecules can move around each other, giving liquid a mobile structure which conforms to its container. Further temperature increase gives molecules sufficient kinetic energy to overcome the binding force and undergo another phase transition, becoming a gas. Characterized by much larger intermolecular separation,

molecules can expand to fill the volume of the container. If more energy is supplied, energetic molecules can undergo collisions that can lead to ionization. The rate of ionization scales positively with temperature, at a critical point where ionization exceeds that of ion and electron recombination, a collective of these charged and neutral particles is called a plasma.

Plasmas can exist over a large range of temperature and number density. Plasmas are characterized by their density, temperature, and degrees of ionization.

Ionization is inherent to plasma formation, but the degree of ionization can vary greatly. Generally, plasmas can be either fully or partially (weakly) ionized. Fully ionized plasmas contain only ions and electrons; one commonly known example is that at the core of stars, where high temperature supplies sufficient energy to ionize all particles. Weakly ionized plasmas contain ions, electrons and neutral particles, and are often found in industrial applications, such as neon signs and fluorescent lights.

Temperature of electron, ions and neutral particles can be defined by their kinetic energies. However, due to the disparity in mass, electrons slowly transfer kinetic energy to ions or neutral particles, thus leading to variation in electron, ion and gas temperatures. In thermal plasmas, all particles are at thermal equilibrium with each other. In non-thermal (low temperature) plasmas, the disparity in masses results in much higher electron temperature than ion temperature. In some cases, ion temperature can be as low as ambient gas tempera-

ture.

In this thesis, we will focus on non-thermal weakly ionized plasmas.

1.2 Non-thermal weakly ionized plasmas

One does not have to look far to find the products of plasma processing technology in their daily life. Plasma-based surface processes, such as etching and deposition, is indispensable for the production of microchips used in everyday electronics. Capable of modifying surfaces over length scales of sub-micrometer, plasmas are used to fabricate integrated circuits at a much smaller scale than attainable using conventional liquid chemical means. Material properties can also be altered; hydrophobic properties are often added to clothing materials used to make athletic apparel in order to wick moisture quickly and help the wearer remain cool.

These surface processes are often performed in low pressure environments. Reducing pressure decreases the total amount of particles in the system, thus energy applied in the system is used mostly to excite electrons and ions. Since energy is not used to heat up neutral gas particles, plasma reactivity is delivered to surfaces more efficiently.

Installing large-scale low pressure systems is costly. Given plasma-based processes are highly controllable and reactive, recently there is increased interest in using atmospheric pressure plasmas to modify surfaces that cannot be contained in a pressurized system. How-

ever, at atmospheric pressure, the number density of neutral gas particles is high, which leads to high rate of collisions with energetic electrons and ions. These collisions can excite neutral gas particles, leading to more complex chemistry both in the gas phase and at the surface.

One particular medium that is amenable to surface activation but is difficult to contain is liquid.

1.3 Plasma-liquid systems

Plasma processing of liquids has the potential to enable a wide range of technological applications, ranging from environmental remediation to agriculture.

Water purification is an area of environmental remediation that can potentially be addressed using plasmas [1, 2, 3, 4, 5]. Due to the effects of global warming and fertilizer runoffs from streams, Lake Erie has seen large-scale harmful algal blooms, which are overgrowth of cyanobacteria [6, 7]. These bacteria can produce different types of toxins that are harmful to humans and animals [8, 9]. Conventional means of water purification, such as ozone and hydrogen peroxide, cannot effectively remove these bacteria and their associated toxins [10, 11]. Plasmas produce highly reactive species, such as hydroxyl radicals and ultraviolet photons, and have been shown to be effective against organic pollutants resistant to conventional treatment [5].

Agriculture is another area where atmospheric pressure plasmas has the potential to solve ongoing challenges. Recently published studies have shown that plasma treatment can increase the germination rate of seeds and enhance plant growth [12, 13, 14]. Alternatively, plasma treatment of water can sequester extra nitrogen from the atmosphere into water in the form of nitrates, which is an essential nutrient for plant growth [14, 15]. These studies indicate that plasma can potentially boost food production on an industrial scale, and help solve the growing demand of food.

Fundamental studies on how plasma interacts with liquid surfaces are crucial. These applications can only be properly designed and implemented by quantifying plasma's reactivity.

Plasmas can be applied to liquids in different ways. A common method to distinguish between various plasma-liquid systems is divided into three main types, which comprises of: 1) direct liquid phase discharges, 2) gas phase plasmas in contact with liquid phase, and 3) multiphase plasmas (e.g. droplets and aerosols).

Direct liquid phase discharges involve transient discharges produced entirely in the liquid. This is often achieved by initiating a strong electric field between two submerged electrodes. Due to liquid's high density, it is easy to see that bringing liquid phase into plasma phase would be more energy intensive than beginning in the gas phase. As such, the electric field required is in the order of 10^3 kV/cm [16]. Currently there is no comprehensive

consensus on the mechanisms of how direct liquid phase discharges form. Two prevailing theories support the notion of 1) the presence of pre-existing micro bubbles and 2) the formation of bubbles due to applied voltage pulses. While direct liquid phase discharges are not scalable for industrial uses because of high energy intensity, it remains an active field of research to understand how plasmas fundamentally behave and exist in liquids, and can be particularly useful for applications where production of gas phase is simply not feasible, such as space applications.

Gas phase plasmas in contact with liquid usually have distinct liquid and plasma phases with a well-defined interface. Two commonly used methods are atmospheric pressure plasma jets (APPJs) and dielectric barrier discharges (DBDs). APPJs comprise of a plasma producing region contained in a tube with a gas outlet. The electrodes can be contained in or outside of the tube, or submerged in the liquid. Plasma formed inside the tube and exits the tube as a plume, which can be in contact with the bulk liquid. DBDs comprise of two electrode separated by a layer of dielectric and often a gaseous region and targeted liquid. They are often distinguished by transient discharge filaments excited between electrodes. Gas phase plasmas have been extensively used in medical applications. APPJs, like kINpen, have been used in wound healing, where plasma plume coming in contact with target treatment area can disinfect and induce wound healing [17]. DBDs have been used to study plasma-induced cell apoptosis in cancer treatment [18, 19]. As tumor cell lines are

incubated on Petri dishes, DBDs remain a favorable method to treat these cells plated on agar surfaces [20]. However, for treatment of a large volume of liquids, APPJs and DBDs are surface-limited and thus do not lend itself for scaling up, but remain great tools to understand plasma-liquid interactions.

Multiphase plasmas most often describe 1) aerosols - gas phase plasmas with dispersed liquid phase, and 2) bubbles - gas phase plasmas dispersed in liquid phase. With aerosols, liquids are sprayed through a plasma treatment region as mist. This is commonly used in agriculture where crops and fruits are sprayed with plasma activated water to fertilize crops and improve shelf-life of fruits [21, 22]. Discharges in bubbles are excited by initiating a high electric field inside the bubble through electrodes in or in contact with the liquid region. As bubble floats in liquids and can thus travel long distance in liquids, it can also improve mixing in the liquid and transfer plasma-derived reactivity far away from the treatment region. This allows for a high throughput system to plasma treat large volumes of liquids [23]. One notable application is drinking water and wastewater treatment for municipalities. Multiphase plasmas are uniquely favorable for use in industrial and environmental applications because plasma-liquid contact area is maximized as the gas and liquid regions are interspersed. Additionally, the voltage required to initiate breakdown is lower in gas phase, which can reduce energy usage of any large-scale system. Increased mixing between gas and liquid phases also improves the transfer of plasma-derived reactivity into target liquids.

In this thesis, we primarily focus on transfer mechanisms in multiphase plasmas.

1.4 Plasma-liquid interactions

The pathways of which plasmas produce and transfer reactivity into liquids can be generally described as the study of plasma-liquid interactions, which describe the chemical and physical processes that take place when plasma comes into contact with liquids. Understanding and characterizing these processes is crucial to any plasma-based applications that serves to activate the liquid for a specific end purpose, such as destroying pollutants for water purification and producing nitrates for plasma activated water. Precise control and application of plasma reactivity demand the disentangling of all the complexities of plasma-liquid interactions through both experiments and modeling.

Various plasma diagnostics methods have been used to characterize plasmas' behavior near liquids and subsequent induced reactions at the interface and in the liquid. Probing the associated physics and chemistry at play gives insight on the fundamental understanding of plasma-liquid interactions. Recently, there is interest in developing real-time in-situ diagnostics methods to determine crucial plasma and liquid parameters for use in both experiments and applications. Spatial and temporally resolved information on plasma parameters is favorable for many applications which demand fine tuning of the production and transport of plasma-derived reactivity.

There are associated limitations on chemical and optical diagnostics when studying plasma-liquid interactions. When liquids are doused with chemical probes to quantify production and transport of plasma-derived reactive species, the probes actively change the properties of the liquid. Thus chemical diagnostics methods often do not remain passive, and can interfere with the measurement itself. Optical diagnostics, while passive, are often spatially limited. For optical diagnostics like imaging, captured images are often integrated onto a plane, thus lack depth; for other methods such as optical emission spectroscopy (OES), measurements are often limited to a small spot. In addition, application of optical diagnostics methods on plasma-based technologies is often not feasible due to the lack of access to regions of interest.

To probe the chemistry and physics at play in multiphase plasmas, it is important to develop real-time in-situ diagnostics methods in order to characterize the complex processes and quantify the induced reactivity.

1.5 Reducing dimensionality as a diagnostic tool

Imaging three-dimensional (3-D) structures in water is difficult. This is mainly due to two effects: 1) surrounding liquids often obscure the region of interest, in this case, the plasma excited in bubbles, and 2) any 2-D image taken is a projection of the original 3-D structure. This leads to the loss of inherent spatial features that might provide valuable insight.

This is particularly important for studying discharges in bubbles. Given the spherical geometry of a gas bubble, a 2-D image of streamer propagation in the bubble is unable to distinguish between axial propagation, which travels across the diameter of the bubble, and surface propagation, which travels along the front face of the bubble. In order to remove distortions in measurements that arise from projection, it is imperative to devise a method to simplify the system and render the interface region accessible. In this sense, reducing dimensionality can be used as a tool to remove inherent system complexity and thereby elucidate the underlying physics in systems of higher dimensionality.

To render the plasma-liquid interface available for optical diagnostics, we employed a 2-D discharge cell to allow direct imaging of the liquid, gas and interface region simultaneously. This is similar to looking at the cross-section of a system with a single bubble trapped in a volume of liquid. Using clear materials such as plexiglass and quartz, a thin layer of liquid is trapped between two clear plates. Stationary bubbles are then injected into the thin liquid layer using a precision syringe, inside where plasmas are excited.

Using this 2-D discharge cell, we have the flexibility to employ different optical and chemical diagnostics methods to probe and directly observe plasma-induced processes at the interface.

1.6 Dissertation scope

Plasma-based technologies aimed to activate a target liquid require effective delivery of desired reactive species into the liquid region, far away from the plasma-liquid interface. Understanding the production and transport processes of these species is necessary for future development of any applications employing plasmas.

In this dissertation, we present an approach to study the physics and chemistry at the interface in a plasma-liquid system by reducing dimensionality from three to two. In particular, we combine the use of the 2-D discharge cell with various optical and chemical diagnostics methods to characterize fluid flow in the bulk liquid, which appears to be driven by plasma in contact with the interface. Research in plasma-liquid interactions to date has been focused on processes at or near the interface, this work addresses the underlying mechanisms driving large-scale transport in the liquid phase as a direct consequence of plasma discharges in the gas phase. This dissertation thus aims to further the understanding of fundamental processes at the plasma-liquid interface, which is crucial to the implementation of plasma-based applications.

Chapter 2 provides the reader with the importance of transport processes at the plasma-liquid interface and surveys prior research in this area. Chapter 3 describes the design and construction consideration of the 2-D discharge cell. Chapter 4 overviews the preliminary results using the 2-D discharge cells with chemical probes to measure propagation of acidic

and oxidative fronts in the liquid. Chapter 5 gives the findings from the investigation on the effects of feed gas on the formation of acidic and oxidative fronts, and absorption spectrophotometry measurements to quantify the production of oxidative species, primarily ozone. Chapter 6 details the study of interfacial stability by visualizing plasma-induced fluid flow with particle image velocimetry (PIV) and density gradient in the liquid using shadowgraphy. Chapter 7 reports the observation and characterization of capillary waves propagating on the bubble surface. Chapter 8 and 9 investigate the effects of liquid conductivity on the discharge morphology inside the bubble and the induced fluid flow using fast ICCD imaging and PIV. Chapter 10 discusses the use of low temperature plasmas in environmental remediation, in particular the removal of hepatotoxin microcystin-LR and the validity of chemical oxygen demand (COD) tests on plasma-treated water. Chapter 11 summarizes this dissertation and proposes potential future work.

Chapter 2

Background

Plasma-liquid interactions cover a wide range of chemical and physical processes. This chapter serves as a review of the known physics and chemistry at play when plasma comes into contact with liquids. We begin with an introduction to atmospheric pressure plasma discharges and discharges in bubbles. Next we introduce the relevant plasma chemistry that leads to the production of reactive species responsible for plasma's desired reactivity. Lastly, we discuss the physical processes such as fluid motion, which drive transport of reactive species and associated reactivity far away from the interface.

2.1 Atmospheric pressure plasmas

Atmospheric pressure plasmas include various natural and manmade plasmas where pressure is approximately that of the atmosphere. They can often be distinguished by the types

of voltage source and discharge geometry. Common voltage sources include: 1) direct current (DC), 2) alternating current (AC), 3) radio frequency waves (RF), 4) microwaves, and 5) pulsed (microsecond or nanosecond). A few notable discharge geometries are described here: 1) corona discharge, 2) plasma jet, 3) dielectric barrier discharge, and 4) spark discharge.

Corona discharge is often localized near the surface of a conductor at sufficiently high electric potential. High electric field strength on the surface of the conductor leads to ionization and formation of a plasma region in the surrounding region. This can be often observed in high voltage wiring with insufficient insulation, and represents a source of energy loss in high voltage systems.

Plasma jets generally describe plasmas produced in a gas-injected tube with an open end, where gaseous plasma plume can exit. Various gasses can be injected; air, helium, argon and nitrogen are some of the commonly used gases. Numerous electrode placements can be employed, and can be placed inside the discharge tube, wrapped around the discharge tube externally, or placed away from the discharge tube. Plasma jets are well established and thus are often used to large variety of industrial and medical applications [24, 25].

Dielectric barrier discharges (DBD) are discharges between conductive planar electrodes separated with a discharge region and a dielectric layer. Since electric conduction current cannot pass through the dielectric layer, only displacement current generated by a varying

electric field can develop. Thus dielectric barrier discharges are operated with alternating current or pulses with short rise time. DBDs are most notable for the formation of filamentary microdischarges in the discharge region, and are often used in industrial surface processing [26].

Spark discharge is a transient discharge, characterized by a rapid and brief emission of light. When breakdown electric field strength is reached abruptly, at approximately 30 kV/cm in air [27], a spark can form, characterized by an observable conductive channel bridging high potential and ground. Large current can flow through but extinguish as breakdown field strength vanishes. Lightning is a natural phenomenon that represents a spark discharge, characterized by the formation of a transient streamer.

2.2 Streamer formation

A simplest discharge can be produced between a positive anode and a negative cathode, held at few hundred volts potential difference. This was first discovered by John Sealy Townsend and thus named Townsend breakdown. Electrons in the gap, either emitted from cathode due to thermionic emission or cosmic ray ionization, drift towards the anode due to the electric field between the electrodes. Each primary electron undergoes ionization collisions with gas molecules in its path, producing more electrons, shown in Fig. 2.1. This

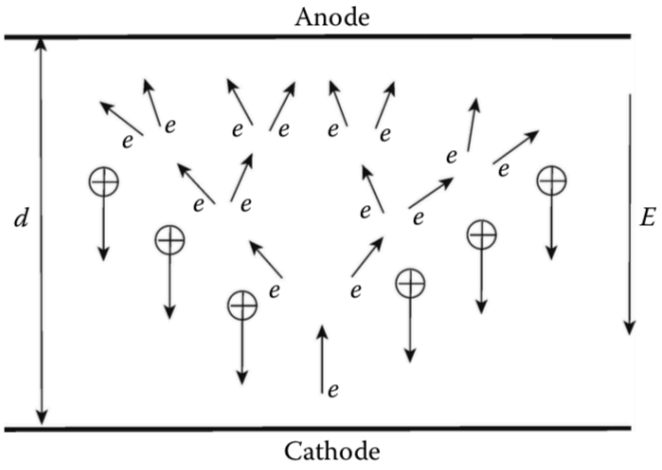

Figure 2.1: Avalanche of electrons produced in Townsend breakdown.

multiplication of electrons generates an avalanche, denoted by

$$\frac{dn_e}{dx} = (\alpha - \beta)n_e \tag{2.1}$$

where n_e is the electron density, α is the Townsend ionization coefficient which defines the electron production (ionization) per unit length, and β is the attachment coefficient. The Townsend coefficient is also the ratio of ionization frequency ν_i to electron drift velocity v_d:

$$\alpha = \frac{\nu_i}{v_d} \tag{2.2}$$

which is gas specific.

For cathode-directed streamers initiated by positive high voltage at the anode, the pri-

mary avalanche is initiated near the anode. The primary avalanche also produces high energy photons through collisions, and leads to photoionization in the vicinity and initiation of secondary avalanches. Accumulated space charges thus enhance the electric field of this charged column. Electrons produced from secondary avalanches get pulled into ionic trail of the primary avalanche due to enhanced electric field at the tip. As electrons continue to move towards the anode while ions move towards the cathode, charges separate in the column. This leads to formation of an internal electric field $\vec{E_a}$. The transition from avalanche to streamer occurs when the magnitude of the internal electric field reaches that of the external field.

$$E_a = \frac{e}{4\pi\epsilon_0 r^2} exp[\frac{\alpha E_0 d}{p}] \approx E_0 \tag{2.3}$$

where e is the electron charge, ϵ_0 is the permittivity of free space, r is the approximate radius of the discharge (or container), E_0 is the external electric field, p is pressure, and d is the discharge gap. This can be further simplified to yield the Meek's breakdown criterion, of which streamer will form if the avalanche amplification parameter αd exceeds 20. In cases where ionization coefficient varies spatially, the criterion can be written as

$$\int_0^x (\alpha - \beta) dx \approx 20 \tag{2.4}$$

As breakdown leads to formation of a self-sustained current, this conductive channel be-

tween anode and cathode is called a streamer.

2.3 Discharges in bubbles

Discharges in bubble are considered of interest in this thesis due to their geometry, which provides an opportunity to study streamer discharges in a closed system with a gas-liquid boundary, and its potential for future environmental and industrial applications. The addition of gas phase and a high surface to volume ratio reduces the breakdown voltage and associated energy, while optimizing contact area with surrounding liquid.

Bruggeman et al [28] first trapped a static bubble in a water-filled capillary to study condition of electrical breakdown as a result of a DC electric field. A bubble filled with dry air, without liquid film on the capillary wall due to external heating, had a threshold breakdown electric field of 18 kV/cm. Once the external heating was removed, a liquid layer formed around the bubble and lowered the threshold voltage required for breakdown due to the presence of conductive liquid. Long rise time of the voltage was also associated with joule heating in the liquid film which led to bubble growth.

Babaeva and Kushner [29] investigated the structure of positive streamers inside gaseous bubbles immersed in liquids computationally using nonPDPSIM. They found that both dielectric constant and conductivity of the liquid can drive variation in propagation of streamers. Due to increases in magnitude and divergence of the electric field, streamers tend

to travel on the surface of the bubble if the liquid is high in either dielectric constant or conductivity.

Tachibana et al [30] studied the effects of feed gas on discharges inside bubbles, and found that plasmas with molecular gases, nitrogen and oxygen, tend to produced predominantly filamentary surface discharges, where plasmas with rare gases, helium, neon and argon, tend to produce volumetric discharges. This is potentially due to higher ionization coefficient at lower electric field for rare gases, which strengthens ionization and field distribution at the front of the streamer. Thus instead of traveling on the surface of the bubble, streamers travel axially and spread out uniformly in the bubble filled with rare gases.

Sommers and Foster [31] employed an ultrasonic acoustic field to levitate and trap an isolated gas bubble, where streamers were excited inside using a pair of submerged electrodes, a flat circular plate and a pointed needle. Liquid-phase streamers initiated from the pointed electrode were observed to both initiate a gas phase streamer inside the bubble and disrupt the bubble-liquid boundary. The surface perturbation effect is a result of streamer impact at the boundary which creates electrical stress, pressure and thermal stress. This stress was observed to be able to rupture the boundary and led to formation of a second bubble. Air plasma was also observed to be more filamentary than that of helium, which is consistent with the results from Tachibana et al [30]. Plasma ignition without visible liquid-phase streamer coming into contact from pointed electrode to bubble surface was also investi-

gated. Reduction of applied voltage to 12 kV was able to ignite plasma in the bubble without visible liquid-phase streamers bridging the gap, due to the presence of sufficient electric field for gas phase breakdown in the bubble, but insufficient for breakdown in liquid phase. Repetitive pulsing was also studied for its effects on plasma ignition. Local energy deposition over many pulses was able to increase gas temperature and vapor pressure in the bubble, which facilitated ionization and subsequent discharge formation.

Gucker et al [32] continued the study of discharges in isolated bubble in water [31] to investigate the effects of bubble size and electrode distance. Bubble size was observed to impact appearance of discharges. Localized corona discharge with weak surface streamers was associated with larger bubbles, and stronger surface discharges accompanied with bubble surface distortion with smaller bubbles. Increasing distance between the electrode tip and the bubble surface led to development of liquid phase streamers as well, of which photon emission can potentially seed photoionization inside the bubble.

Hamdan and Cha [33] studied the effects of bubble location and feed gas in nanosecond discharges in bubbles submerged in distilled water. They observed three distinct modes of streamer ignition: 1) anode-driven ignition, 2) cathode-driven ignition, and 3) co-ignition. This was driven mainly by the proximity of the bubble surface with the electrodes. Argon, helium and nitrogen were used for this study, and they found that argon discharges have the longest lifetime due to the much lower breakdown field and resulting in increased ion-

ization in argon plasmas. However, breakdown strength and lifetimes of metastable states in nitrogen and helium cannot account for the longer lifetime of emission in nitrogen plasmas. Lastly, ignition in double and triple bubbles were observed, indicating discharges can travel between adjacent bubbles. This was attributed to potential transport of solvated electrons along the electric field lines in the liquid, these electrons accumulate on the surface and seed weak ignition in the adjacent bubble.

2.4 Plasma chemistry

Gas phase plasma produces numerous reactive species, including ions, electrons, radicals, and excited neutral particles. When plasma comes into contact with a liquid surface, complex chemistry takes place in the gas phase, liquid phase, and the interface. In this section, we focus on the production and transport of reactive species at the interface and in the bulk liquid. This is a brief review of crucial chemical reactions associated with various reactive species.

2.4.1 Electrons

Low temperature plasmas have higher electron temperature than that of ions and neutral particles due to the lower mass of electrons. These energetic electrons can impact the interface, solvate into the liquid media, or cause excitation, dissociation and ionization of water molecules.

Low energy electrons tend to solvate in aqueous solutions [34]. They have vertical binding energies of 1.6 eV at the water surface and 3.3 eV in a bulk solution with a lifetime of over 100 ps, and are suspected to be involved in dissociative electron-attachment processes [34]. While its lifetime is in the order of microseconds in pure water [35], its lifetime in aqueous solutions is much shorter due to its high reduction potential. Thus solvated electrons are highly reactive with dissolved ions, radicals and neutral particles [36]. However, due to its reactivity, analytical model by Rumbach et al [37] showed that solvated electrons have a typical penetration depth and interfacial concentration of approximately 100 nm and 0.1 mM, and as a result, are unlikely to directly drive reactive chemistry in the bulk liquid but could play important roles at the interface.

High energy electrons, on the other hand, can excite, dissociate, ionize and attach to liquid molecules at the interface through electron impact reactions. Particularly for water, these impact reactions represent important pathways for the production of desired reactive species crucial for industrial and medical applications. A selective few of these reactions are listed here [38]:

$H_2O + e^- \longrightarrow OH^\bullet + H^\bullet + e^-$ (electron impact dissociation)

$H_2O + e^- \longrightarrow O^\bullet + 2\,H^\bullet + e^-$ (electron impact dissociation)

$H_2O + e^- \longrightarrow H_2O^+ + 2\,e^-$ (electron impact ionization)

$H_2O + e^- \longrightarrow OH^- + H^+ + e^-$ (electron impact dual attachment/ionization)

$H_2O + e^- \longrightarrow OH^- + H^\bullet$ (dissociative attachment)

The production of hydroxyl radicals $OH^\bullet$ and singlet oxygen $O^\bullet$ is particularly important due to their high oxidative potentials.

2.4.2 Ions

Ions are much heavier than electrons, and thus undergo mostly solvation and impact collisions at the interface. Minagawa et al [39] reported that simulated O^+ ions with energies of 100 eV can only penetrate to a maximum depth of 2.75 nm, while half of them sputtered off water molecules, thus any ion-induced reactions are local to the interface. However, solvation remain a main pathway for positive ions to transfer charges to the liquid layer. Simulations done by Norberg et al [24] showed that solvated ions can undergo charge exchange with water molecules to produce positive water ions,

$M^+ + H_2O \longrightarrow M + H_2O^+$

Positive water ions then quickly undergo charge exchange with another water molecule to produce hydronium ions and hydroxyl radicals

$H_2O^+ + H_2O \longrightarrow H_3O^+ + OH^\bullet$

where hydronium ions are a main source of acidity in plasma-treated water.

2.4.3 Excited species

While excited species do not participate in chemical reactions at the interface, excited species have sufficient energies upon impact at the interface will undergo impact dissociation reactions [40]. In addition, Lukes et al [38] reported that excited state can undergo electron transfer with oxygen

$$R^* + O_2 \longrightarrow R^+ + O_2^-$$

and Kruszelnicki et al [41] reported that excited nitrogen species in the gas phase can emit photons and lead to photoionization of oxygen.

2.4.4 Reactive oxygen and nitrogen species

Air plasmas can produce a myriad of gas phase reactive species that diffuse into the interface and initiate chemical reactions. In particular, the production and transport of reactive oxygen and nitrogen species (RONS) is important as they drive most of the reactivity in water.

The diffusion of gas phase species across the interface is proportional to their partial pressures and is governed by Henry's laws. The higher of Henry's law solubility constant, the more soluble the species is in aqueous solutions. Henry law's constant for a few RONS are reproduced in Table. 2.1 from Lietz and Kushner [40].

Species with high Henry's law constant, such as hydrogen peroxide, mostly reside in the liquid phase. Constant compensation from the gas phase can also saturate the interfacial

Species	h
ROS	
H_2O_2	1.92×10^6
HO_2	1.32×10^5
H	6.48×10^3
OH	6.20×10^2
O, $O(^1D)$	1
O_3	3.00×10^{-1}
RNS	
HNO_3, ONOOH	4.80×10^6
HO_2NO_2	2.99×10^5
NH	1.47×10^3
HNO_2, HNO	1.15×10^3
N_2O_3	6.00×10^2
N_2O_5	4.85×10^1
NO_3	4.15×10^1
N_2O_4	3.69×10^1
N_2O	5.99×10^{-1}
NO_2	2.80×10^{-1}
NO	4.40×10^{-2}

Table 2.1: Henry's law constants of selected RONS.

layer until the species in liquid phase diffuse away.

Particularly of interest is the production of hydrogen peroxide, hydroxyl radicals and ozone, due to their high chemical reactivities and the ability to drive chemical reactions in the bulk liquid.

Hydroxyl radical ($OH^\bullet$) is a short-lived free radical that has a high oxidative potential E^0 of 2.85 V [42], and can decompose a large variety of organic pollutants that are resistant against conventional means of water purification [43, 44, 45]. However, its lifetime is short. Codorniu-Hernández and Kusalik reported a rough estimation of hydroxyl radical's

lifetime to be 30 ps in aqueous solutions [46], where Attri et al reported a measured experimental lifetime of approximately 3 μs for hydroxyl radical produced by plasma-initiated ultraviolet (UV) photolysis in deionized water [47]. Due to its short lifetime and high reactivity, hydroxyl radicals do not penetrate far into the liquid region. Rumbach et al [37] showed analytically that hydroxyl radicals have a typical penetration depth and interfacial concentration of approximately 100 nm and 0.1 mM because of quick recombination to form hydrogen peroxide. Hydroxyl radicals in the liquid are commonly produced in 3 pathways. Hydroxyl radicals from gas phase can transport across the interface into the liquid phase. Electron impact dissociation at the interface can also produce hydroxyl radicals. In the bulk solution, ultraviolet (UV) produced from plasmas can photodissociate water to provide hydroxyl radicals as well,

$$H_2O + h\nu \longrightarrow OH^\bullet + H^\bullet$$

Sugiarto et al [48] investigated the discoloration of organic dye Rhodamine B using pulsed discharges excited between electrodes arranged in the needle-to-plane geometry, and found that increase decomposition of Rhodamine B can be attributed to photodissociation of hydrogen peroxide added initially to the solution.

Hydrogen peroxide has been historically used as an oxidizer and an antiseptic, commonly applied in water treatment [49] and wound sterilization [50]. It has an oxidative potential E^0 of 1.77 V [42]. Hydrogen peroxide is often attributed to as the main driver of reactiv-

ity in plasma-based reactors for water purification. Traylor et al [1] reported long-term antibacterial effects of plasma-activated phosphate buffered saline (PBS), hydrogen peroxide concentration of 200 μM was measured and did not vary significantly over 7 days. Lukes et al [51] found the initial hydrogen peroxide production rate of 4.9×10^{-7} mol/s in a hybrid gas-liquid electrical discharge reactors with electrical potential set at 45 kV. Lifetime of hydrogen peroxide in water is long, store bought hydrogen peroxide can be shelf stable for years. Combining with its high Henry's law constant, hydrogen peroxide is often the most abundant RONS in liquid phase. Lietz and Kushner [40] found that the density of aqueous hydrogen peroxide reached $3 \times 10^{13} cm^{-3}$ after 5000 pulses in a computationally modeled dielectric barrier discharge (DBD). The simplest reaction mechanism that result in production of hydrogen peroxide is the recombination of hydroxyl radicals, and reacts in timescales of microseconds [40].

$$2\,OH^{\bullet} \longrightarrow H_2O_2$$

Ozone is a commonly used as a disinfection agent in conventional water treatment [52, 53, 54], due to its strong oxidation potential of 2.07 V. In distilled water, ozone has a half-life of approximately 165 mins, less if contaminants are present to react with ozone; but has a half-life of 12 hours in air [52]. As a result, conventionally, ozone is produced in dry air or oxygen, and subsequently piped to target water sources in need of treatment. However, plasmas in contact with water can produce ozone in-situ at the interface. Lietz and Kush-

ner [40] reported the primary source of gaseous ozone is the three-body recombination of singlet oxygen atoms and oxygen.

$$O^{\bullet} + O_2 + M \longrightarrow O_3 + M$$

This accumulation of gaseous ozone leads to solvation of ozone into the liquid phase, and represents the primarily contribution to aqueous ozone as well, with a concentration of 5×10^{16} cm^{-3} found in the liquid phase [40]. In addition, Glaze [52] reported that photolysis of ozone in water can lead to production of hydrogen peroxide, and can attribute to production of sustained reactivity in plasma-activated water.

Due to the large amount of nitrogen in air, plasma can also produce a variety of reactive nitrogen species (RNS), which drives the plasma-driven acidity in water. Reduction of pH in plasma-treated water has been observed in these studies [55, 56, 57]. Lukes et al [42] recounted the production of gas phase nitric oxide NO through a multistep process.

$O_2 + e^- \longrightarrow O^{\bullet} + O^-$ (electron impact dissociation of oxygen)

$O^{\bullet} + N_2{}^{\star} \longrightarrow NO + N^{\bullet}$ (Zeldovich 2-step mechanism, first step)

$N^{\bullet} + O_2 \longrightarrow NO + O^{\bullet}$ (Zeldovich 2-step mechanism, second step)

Excited nitric oxide can also react with oxygen to form nitric dioxide.

$$NO^{\star} + O_2 \longrightarrow NO_2 + O^{\bullet}$$

Nitric oxide and dioxide can react with ozone and singlet oxygen to form nitrates and nitrites.

$$NO + O_3 \longrightarrow O_2 + NO_2$$

$$NO_2 + O_3 \longrightarrow O_2 + NO_3$$

$$NO + O^\bullet \longrightarrow NO_2$$

$$NO_2 + O^\bullet \longrightarrow NO_3$$

Nitrates and nitrates can solvate into the liquid phase, and react with hydroxyl radicals to form nitric and nitrous acid.

$$NO + OH \longrightarrow HNO_2$$

$$NO_2 + OH \longrightarrow HNO_3$$

Nitric and nitrous acid can hydrolyze water, leading to the production of hydronium ions, and thus the reduction in pH.

$$HNO_2 + H_2O \rightleftharpoons H_3O^+ + NO_2^-$$

$$HNO_3 + H_2O \rightleftharpoons H_3O^+ + NO_3^-$$

2.4.5 UV production

Ultraviolet (UV) radiation from plasma discharges results from production and relaxation of excited species as a result of collisions between electrons, ions and gas particles. Positive streamers propagate as a result of photoionization at the streamer head. These high energy photons impacting the interface can also trigger photochemical reactions. These reactions are local due to the short mean free path of UV and VUV (vacuum ultraviolet) photons, from a few to 10μm [58].

Photolysis of water produces hydroxyl radicals [42, 59],

$$H_2O + h\nu \longrightarrow H^\bullet + OH^\bullet.$$

Simulation by Norberg et al [24] showed that photolysis was responsible for the rapid production of hydroxyl radical during the discharge pulse, in the order of tens of nanoseconds, for atmospheric pressure plasmas jet in contact with a water layer. Photons can also lead to photoionization at the interface

$$H_2O + h\nu \longrightarrow H_2O^+ + e^-,$$

accounting for 62% of initial production of positive water ion H_2O^+. This reaction is the dominant source of charge injection into the water, through charge exchange reaction between H_2O^+ and H_2O producing hydronium ions H_3O^+. This reaction produces hydroxyl radicals as well, where photoionization contributes to production of almost 70% of hydroxyl radicals [24].

UV radiation can catalyze other reactions in aqueous solution as well. While ozone and hydrogen peroxide have a longer lifetime in water, photolysis of ozone can lead to the local production of hydroxyl radicals through these reactions [42, 59]:

$$O_3 + h\nu \longrightarrow O_2 + O(^1D)$$

$$O(^1D) + H_2O \longrightarrow 2\,OH^\bullet$$

$$H_2O_2 + h\nu \longrightarrow 2\,OH^\bullet$$

RNS are also susceptible to photochemical reactions and lead to production of desirable

radicals through these reactions [42, 59]:

$$NO_2^- + h\nu \longrightarrow NO^\bullet + O^-$$

$$NO_3^- + h\nu \longrightarrow NO_2^\bullet + O^-$$

Lastly, UV radiation is desirable for its use on disinfection as well. UV is commonly used in drinking water treatment to protect against microbes and chemicals. Chang et al [60] reported the usage of germicidal UV to achieve 99.9% inactivation of bacteria Escherichia coli, Salmonella typhi, Shigella sonnei, Streptococcus faecalis, Staphylococcus aureus, and Bacillus subtilis spores, the enteric viruses poliovirus type 1 and simian rotavirus SA11, and the cysts of the protozoan Acanthamoeba castellanii. Foster[61] also report the potential of using plasma treatment of water to remove disinfection by-products such as carcinogen N-Nitroso-dimethylamine (NDMA) through photolysis.

2.5 Physics at the interface

Plasma discharges can initiate physical interactions at the interface. Momentum transfer from the plasma can lead to thermal and mass transport at the interface and drive several physical phenomena in the liquid.

2.5.1 Thermal effects

Kondo and Ikuta [62] reported the increase of gas temperature of several hundred degrees after repetitive positive streamer corona in point to plane gap with air, ignited using a DC

voltage. Breden and Raja [63] showed the increase of 100-200 K in an 4-kV 10-ns anode pulsed discharge. Increased gas temperature can heat up the interface region locally, this heat gradient will likely diffuse into the bulk liquid at a much longer timescale. The local surface heating can cause evaporation and increase vapor pressure in the gas phase as well.

In addition, current passing through a liquid with a finite conductivity can produce heat, namely through Joule heating. The power dissipated in the liquid P is proportional to the current passed I and the equivalent resistance R of the liquid, where $P = I^2R$. At low conductivity, water behaves as a lossy dielectric through which direct current does not pass. Presence of electric discharges in contact with water can result in displacement current in the water due to the time-varying electric field from the discharge ignition.

Local heating effects can create heat gradient in the liquid layer, and result in surface tension gradient. This is discussed in Section. 2.5.3.

2.5.2 Surface deformation

Plasma contact at the interface can drive surface perturbations due to mass transport of energetic particles and electric field effects.

Using a static machine to charge a drop of liquid in a glass tube, Zeleny was able to show that electric field can lead to hydrodynamic instability on surfaces of ethyl alcohol, a polar solvent [64]. This observations were extended to water droplets by Taylor, who found that a water drop was elongated by an electric field [65], and served as early results of deforma-

tion of air-water surfaces due to electric field effects.

Subsequently, surface deformation was also observed in plasma-liquid systems. Bruggeman et al initiated breakdown in an air bubble trapped in a water-filled capillary and found that bubble deformation can lead to local electric field enhancement and plasma formation [28]. Bruggeman et al also employed a metal pin-water electrode system with DC applied voltage to investigate the electric effects on surface distortion as a result of electrical breakdown. They observed the same Taylor-cone like shape on the water surface, and found that the instability of the water surface was a necessary condition for triggering electrical breakdown at small inter-electrode spacings [66]. These observations suggested that surface deformation and plasma formation can be synergistic in nature.

Sommers et al postulated that strong electric field at the tip of the streamer can cause electrical stress and distort the surface of an air bubble. For a cathode-attached bubble, low amplitude waves were observed to develop on the bubble-liquid interface, and they appeared to consistent with those calculated with Kelvin's equation which describes capillary waves propagation on a surface as a result of surface tension and gravity, modified to include the contribution of a uniform electric field [67],

$$\omega(k) = \frac{\gamma k^3}{\rho} + gk + \frac{\epsilon_0 E^2 k^2}{\rho} \tag{2.5}$$

where $\omega(k)$ is the Kelvin's dispersion relation, γ is surface tension of the fluid, ρ is the den-

sity of the liquid, g is gravity, E is the magnitude of the electric field. In addition to capillary waves propagation on the surface, electric field can also alter the shape of the bubble. In bubbles suspended in water using acoustic standing waves, shapes of the bubble appeared to decompose into their axisymmetric spherical harmonic modes. These distortions can enhance the internal electric field and facilitate breakdown inside the bubble [68].

2.5.3 Fluid effects

Plasma-driven fluid flow remains a largely unexplored research field. Here we primarily summarize the basis of Marangoni flow and experimental reports on plasma-driven flow.

Theoretically, fluid flow in a liquid is governed by Navier-Stokes equations of momentum (Eq. 2.6) and energy (Eq. 2.7), and equation of continuity (Eq. 2.8) for incompressible fluid,

$$\frac{\partial \rho \mathbf{u}}{\partial t} + \mathbf{u} \cdot \nabla \rho \mathbf{u} = -\nabla p + \nabla \cdot \tau + \rho \mathbf{g} \tag{2.6}$$

$$\frac{\partial \rho E}{\partial t} + \nabla \cdot (\rho E \mathbf{u}) = -p \nabla \cdot \mathbf{u} + \tau : \nabla \mathbf{u} - \nabla \cdot \bar{q} + Q_c + Q_r \tag{2.7}$$

$$\nabla \cdot \mathbf{u} = 0 \tag{2.8}$$

where $\mathbf{u}$ is the velocity field, t is time, ρ is density of the fluid, p is pressure, τ is stress tensor, $\mathbf{g}$ is gravity, E is energy, $\bar{q}$ is heat flux and is calculated as $-k\nabla T$, where k is thermal conductivity and T is temperature, and Q_c and Q_r are heat produced from chemical reaction

and radiation respectively.

Marangoni stress can arise due to surface tension gradient in a liquid layer, which is a function of both temperature and concentration. The stress tensor due to Marangoni effects $\tau_{Marangoni}$ can be described as:

$$\tau_{Marangoni} = \nabla_s \sigma(x, y, t, T, C) \tag{2.9}$$

where ∇_s is the gradient operator along the surface, and $\sigma(x, y, t, T, C)$ is the surface tension, which is dependent on location, time, local temperature and local concentration.

Localized heating can lead to development of temperature gradient in the liquid layer. In plasma-liquid systems, elevated gas temperature in the plasma region can lead to localized heating in the interface region, which slowly diffuse into the liquid. Surface tension is a function of temperature,

$$\sigma = \overline{\sigma}_0 + \frac{d\sigma}{dT}\delta T \tag{2.10}$$

where $\overline{\sigma}_0$ is the surface tension at temperature T_0, $\frac{d\sigma}{dT}$ is the surface tension gradient, a constant dependent on the liquid type and δT is the temperature difference between T and T_0. Using Eötvös's rule, $\frac{d\sigma}{dT}$ can be estimated to be $-1.46 \times 10^{-4} \frac{N}{m-K}$ for water [69]. That is, water of lower temperature will have a higher surface tension. As a result, for a water region with a localized temperature gradient, water will flow from hotter to colder regions. The

resulting fluid flow is the temperature gradient-based Marangoni flow, also called thermo-capillary convection.

Addition of surfactant, or oxidation (thus removal) of surfactant by plasma, can result in concentration gradient. Berendsen et al [70] reported the use of cold atmospheric pressure plasma jets flowing argon or air to modify liquid hydrocarbon films on a rotating substrates. Oxidation of the film surfaces increased local surface tension, and gave rise to a concentration-based surface tension gradient, and led to redistribution of solutes in the liquid film which resulted in observed flow.

Studies of plasma-driven fluid flow also reported the possibility of liquid flow as a result of friction between ion flow in gas phase and the liquid surface.

Using a platinum electrode encased in a ceramic tube suspended 1 mm above a small glass container containing water, Shimizu et al [71] observed fast gas flow driven by accelerated ions in the electric field from the electrode tip to the water surface. Employing particle image velocimetry, they recorded the presence of circulating flow in the liquid layer that was induced at the contact point between the plasma and the water surface and spread throughout the bulk liquid, with maximum velocity of 2.5-3 cm/s found at the contact point going upward towards the electrode tip. Due to the presence of fast gas flow near the water surface, they postulated that the driving force of the fluid flow was that of friction between the fast gas flow induced by the discharge and the water surface. Measurements with methyl

red showed that the pH change followed closely with the fluid flow, thus reactive species responsible for pH reduction such as nitric acid were likely transported in the liquid due to this convective flow.

This is consistent with observations made by Thagard et al [69]. Using a rod-plane geometry, plasma discharge was excited between a charged rod and a planar liquid surface. Using particle image velocimetry, the fluid flow field in the liquid layer was measured while the composition and conductivity of the liquid were varied. For the baseline case with only sodium chloride dissolved in water, with a electrical conductivity of 1.042 mS/cm, weak flow first developed which travelled towards the discharge on the surface, but the flow reversed direction after 4 seconds and led to formation of a vortex in the liquid that moved away from the centerline of the reactor. This was attributed to the fluid flow responding to the ionic wind generated by the plasma discharge in the gas phase traveling downward towards the water surface. Computational effort was used to ascertain the required tangential gas velocity to achieve the observed liquid surface velocities (of the order of 10 mm/s), and found that the gas velocity has be to of the order of 0.1 m/s and is consistent with that of ionic wind reported. Additionally, the addition of surfactants was used to alter the surface tension of the liquid. As the added surfactants were degraded by the discharge, surface tension was gradually restored to that of liquid water. This had interesting effects on the induced fluid flow. Localized surface tension gradient resulting from degradation of surfac-

tants led to the development of Marangoni flow. The induced Marangoni flow had vortices with the opposite direction comparing with the case of water. As more surfactants were degraded, the fluid flow eventually restored to that dominant by ionic wind.

Chapter 3

2-D Plasma-in-liquid Discharge cell

This chapter introduces the 2-D discharge cell primarily designed and built to allow simultaneous imaging of the liquid phase, gas phase, and interface of a plasma-liquid system.

Due to the presence of intervening fluid surrounding a bubble, the plasma-liquid interface does not lend itself well to optical diagnostics. Optical emission spectroscopy, often used to study discharges in liquid [72], is difficult to employ due to the lack of access to the gas phase region. Investigation of breakdown in bubbles in capillary tubes yielded some insight into interfacial phenomena [73], but capillary tubes are limited in understanding fluid dynamical effects, such as circulation patterns induced by interface dynamics or the propagation of chemical fronts derived by reactivity excited at the interface observed in systems with higher dimensionality [74, 75, 76].

While it is difficult to map the structure of plasma attachment at the interface, it is possible to experimentally simulate a 2-D slice or cut plane of the system. Such a cross-sectional slice would include the core plasma, interface and surrounding fluid, and serves as a 2-D plasma-bubble analogue. This reduction in dimension is schematically shown in Fig. 3.1. Here a plasma jet interacting with a column of water is illustrated. A 2-D slice of the plasma

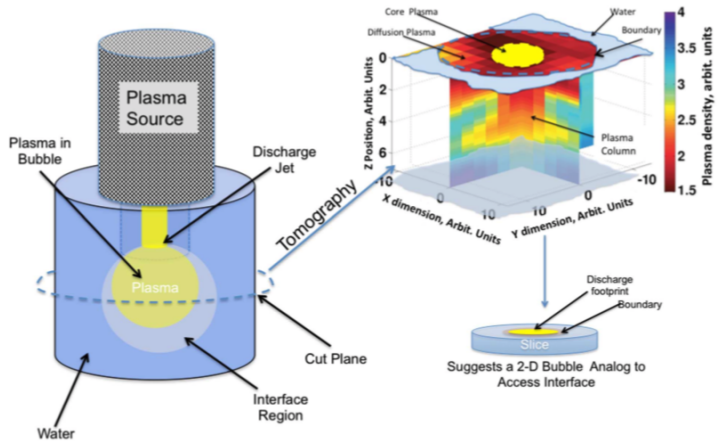

Figure 3.1: Schematic of the decomposition of the plasma interaction with water into a tomographical slice.

residing in a gas bubble would reveal the interfacial region. Experimentally, this can be implemented in a manner similar to approaches taken in fluid mechanics to study 2-D flows and associated chemical reactivity in solution, such as the Hele-Shaw cell. The cell consists of two closely spaced plates between which fluid is injected. The fluid flow inside the cell is laminar and in the plane of the plates. Flow is essentially irrotational. Flow of this nature is known as potential 2-D flow. Indeed, the flow in a Hele-Shaw cell is somewhat paradoxical in that it is essentially inviscid even though the fluid surface is subjected to viscosity at

the boundaries. The velocity profile along the thickness of the fluid is indeed parabolic. A schematic representation of a Hele-Shaw cell is shown in Fig. 3.2 [77].

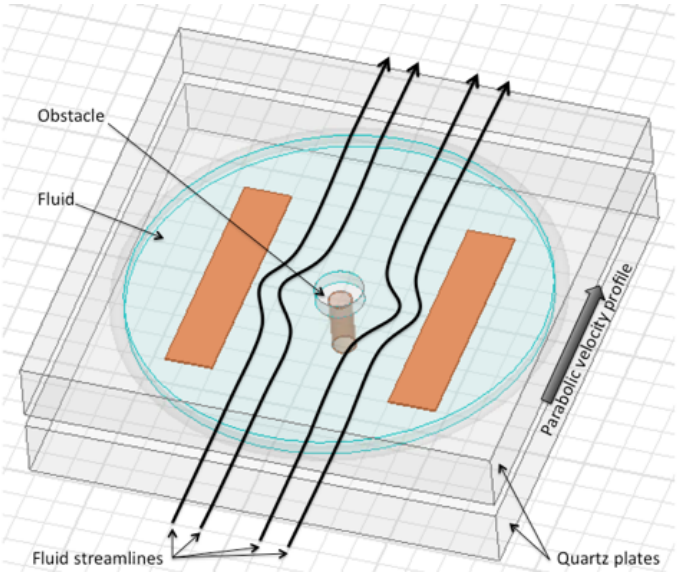

Figure 3.2: Schematic of a simple Hele-Shaw cell.

Because the trapped fluid layer in the Hele-Shaw cell is relatively thin, processes taking place therein are optically accessible. This attribute makes the approach an attractive analogue to study the plasma-liquid interface. Diagnostics, such as optical emission spectroscopy, can be used to study the plasma composition in the bubble. Propagation of acidic fronts can be readily studied using chemical probes such as methyl orange. Lastly, since motion in the cell is 2-D and inviscid, any fluid dynamical effects associated with plasma formation, such as induced circulation, can be mapped using Schlieren or velocimetry methods.

A few generations of the 2-D discharge cell were designed and implemented to accommodate various optical diagnostics methods and investigate alternative electrode geometries.

3.1 First generation design

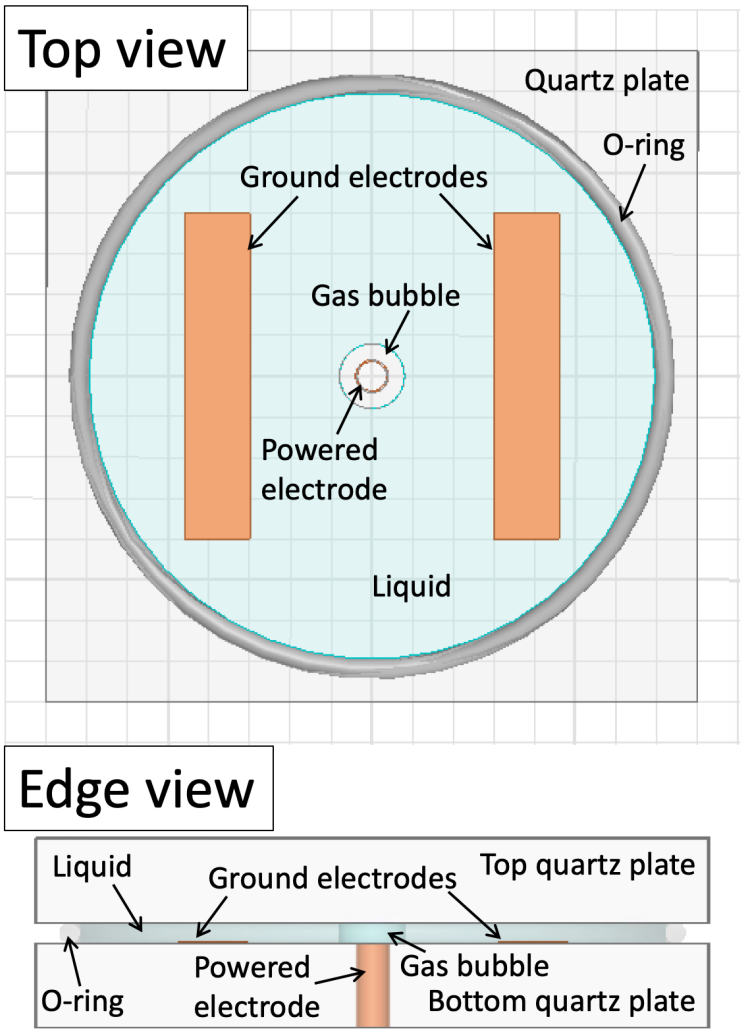

Figure 3.3: Schematic depiction of the first generation 2-D discharge cell.

The first generation 2-D discharge cell is shown schematically in Fig. 3.3. The central, powered electrode consists of a 2-mm diameter stainless steel tube flush mounted to a 7.6 cm by 7.6 cm quartz plate with thickness of 6 mm. Two flat, planar electrode composed of 0.1 mm thick copper film served as the symmetrically counter ground electrodes. The central electrode was sealed to the quartz plate using UV grade transparent optical epoxy. The electrical connection to the ground electrode is made using stainless steel rods bonded to the copper plate electrodes. These rods pass through channels in the quartz plate and are sealed using epoxy. The water reservoir and seal is maintained using a Buna-N O-ring. Once water is placed in the cell, the cell is sealed with a top quartz plate of similar dimensions. The central bubble is injected via precision syringe connected to the powered electrode. Bubble diameters ranging from the diameter of the powered electrode to 1.0 cm were investigated with the apparatus. The overall arrangement has the general form of a point to plane discharge.

3.2 Second generation design

Two variations of the second generation 2-D discharge cell were built. Fig. 3.4 shows the variation with two flat ground electrodes and an O-ring to contain the liquid layer. Fig. 3.5 shows the alternate version with a raised ring electrode to contain the liquid layer. The dimensions of the quartz plates were 8 cm $\times$ 8 cm $\times$ 1 cm. The sealing O-ring used had an

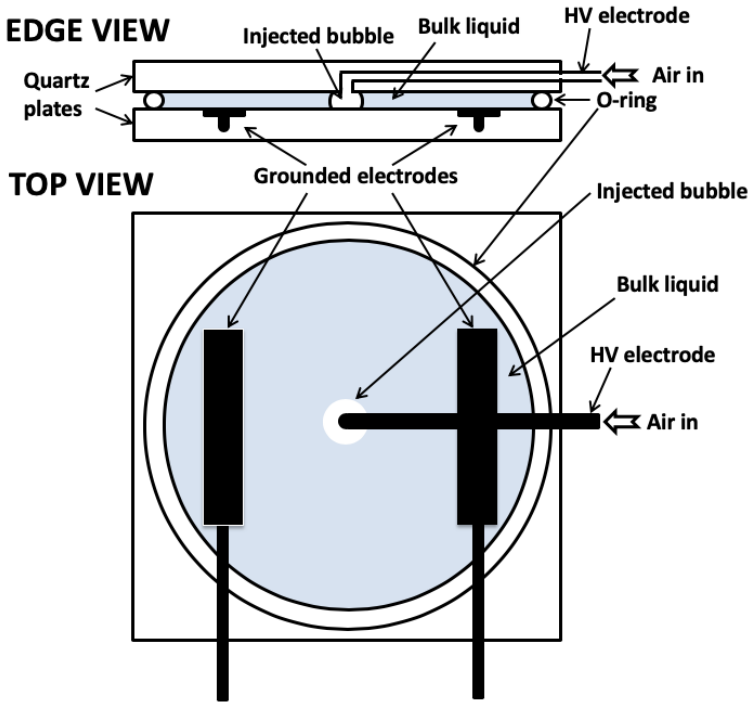

Figure 3.4: Schematic depiction of the second generation 2-D discharge cell, with flat electrode variation.

inner diameter of 7.27 cm and a thickness of 1.78 mm. The raised ring electrode is approximately 1.5 mm thick from the quartz surface. A trapped bubble is injected into the liquid through a stainless steel tube embedded in the top quartz plate through a bored hole. This hollow tube also serves as the high voltage electrode. The ground ring electrode embedded in the bottom quartz plate has an inner diameter of 38.5 mm, and also serves to contain the liquid in the cell. Alternatively, solid stainless steel tube was inserted in the bottom quartz plate, and was connected to copper tape strips on the surface which act as flat rectangular-shaped round electrodes.

Contrary to the first generation 2-D discharge cell, the electrodes in this cell was extended

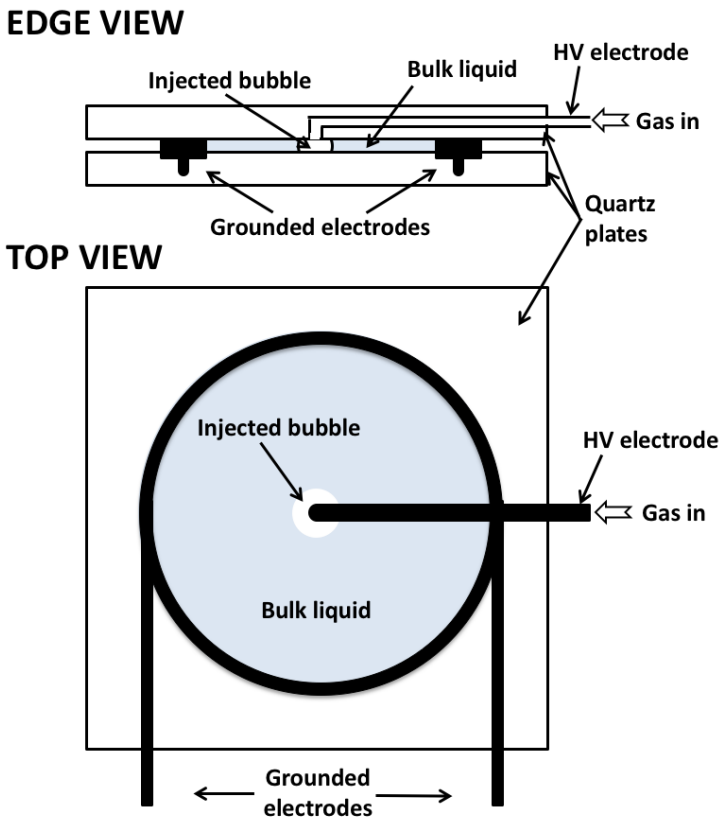

Figure 3.5: Schematic depiction of the second generation 2-D discharge cell, with ring electrode variation.

through bored holes in the quartz plates. Thus any electrical connections can be made away from the imaging plane. This allows for the use of back light or solid white background for imaging colorimetric responses of chemical probes.

3.3 Third generation design

The third generation of 2-D discharge cell is shown in Fig. 3.6. A 0.5 mm deep, 30 x 30 mm reservoir was etched into a 1-cm thick plexiglass plate. This depression contained the liq-

uid and injected bubble used in this study. The top plate was made of quartz in order to maximize transmission of plasma emission through the plate. A 2-mm thick cathode made with stainless steel was embedded in one end of the plate. A 10-μL syringe with a 26 gauge blunted needle (Hamilton 1700 Series Gastight Syringes #80085) was threaded in a track with a diameter of 0.47 mm, and acted as both the anode and the gas injection port. Bubbles injected contained atmospheric pressure ambient air, and had volume of 10 μL, which gave an approximately axial diameter between 3.5 to 4.5 mm.

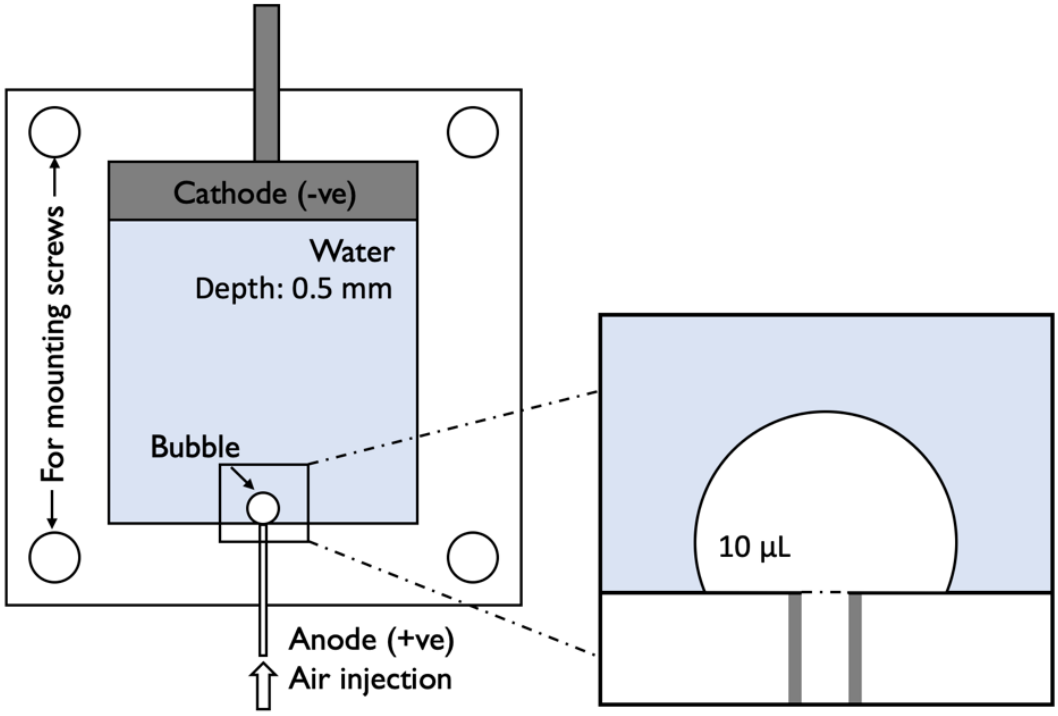

Figure 3.6: Schematic depiction of the third generation 2-D discharge cell.

The previous generations of 2-D discharge cell are considered to have a radially symmet-

ric point-to-plane discharge, where the powered electrode, gas bubble and the ground electrode are all concentric. Assuming the injected bubble is perfectly circular and centered with the powered electrode, streamer propagation is expected to be stochastic, and can be anywhere in the bubble given the uniformly radial electric field.

In this particular generation of 2-D discharge cell, the electrodes are placed in a linear pin-to-plane geometry instead. The bubble is injected near the electrode held at a higher potential. Thus the resulting electric field inside the bubble will generally point away from the attached electrode. The altered electric field allows us to investigate directed streamer discharges in bubbles.

Chapter 4

Preliminary results in 2-D discharge cell

This chapter describes the early experimental results using the 2-D discharge cell to study the plasma-liquid interface. The discharge produced in the flattened bubble was characterized. In addition, chemical probes were used to track the propagation into bulk solution of reacting chemical fronts, which originated at the plasma-liquid interface region. Plasma-induced emission of the bubble discharge was characterized using optical emission spectroscopy to identify active species in the gas phase. Finally, plasma-mediated fluid flow effects, which were also found to originate at the interface, were also observed. These local effects were found to give rise to large-scale circulating flow patterns in the bulk liquid.

4.1 Experimental set up

The apparatus used was described in Section. 3.1. The discharge was generated using a 10-kV pulsed power source capable of generating 13-ns wide pulses with 3-4 ns rise time at a pulse repetition rate of up to 10 kHz. The voltage applied to the powered electrode was measured using a Tekronix 6015A high voltage probe. Current was monitored suing a Pearson 6585 current sense coil. A 300 MHz bandwidth oscilloscope (TDS 3034C) was used to acquire voltage current waveforms.

An application of voltage to the trapped bubble resulted in a plasma discharge that either had the form of a localized microdischarge at either or both the central powered electrode or the water-gas interface, or a streamer discharges that propagated from the powered electrode to the water-gas interface. The microdischarge plasma can be best described as a dielectric barrier discharge with the water serving as one of the dielectric barriers. The discharge type was voltage dependent with the streamer discharge tending to form at peak voltages above 6800 V. In both cases, the discharges did not extend beyond the gas/liquid boundary, suggesting that any effects observed in the bulk were due primarily to plasma-liquid interface interactions.

In this work, the plasma was excited at 2.5 kHz. In addition to investigating nanosecond pulsed discharges, continuous wave-excited discharges were also studied. Here, a 20-kV, 27-kHz AC source was used to excite the bubble. Interest in discharges excited in this range is

derived from the fact that the plasma falls intermediate between non-thermal and thermal, which could have potential advantage of driving higher temperature reactions without the complete heating of the gas [78].

Emission spectra presented herein was acquired using an Ocean Optics HD 4000 spectrometer, which has a wavelength range from 200 to 1100 nm, with 300 lines per nm grating, a 5 μmeter wide slit and an optical resolution of approximately 0.02-8.4 nm FWHM. In order to image the physical details of the bubble and discharge attachment, an AmScope stereomicroscope with a magnification from 2x to 225x and working distance of 356 mm was utilized. The microscope was also used to observe spatial and temporal changes in water doped with colorimetric chemical probes, which were used to study the propagation of plasma-driven chemical fronts. The microscope utilized a 9 megapixel CMOS camera with an acquisition speed of 6 frames/s.

The physical morphology of the discharge (bounded by quartz plates) are assumed to be not as important as the chemistry induced when the plasma contacts the liquid at the interface. Surface discharges that could potentially occur along the quartz plates are themselves merely additionally sources of reactive oxygen or nitrogen species (ROS/RNS), and therefore should not impact the interpretation of the fluid response to the discharge. Gas phase species in general results from either microdischarges or streamers. In addition, the fluid flow is laminar and owing to viscosity effects flow speed is essentially zero, at the plates sur-

face. Any observed flow is, therefore, a consequence of processes removed from the plates.

Of particular interest is the electric field in solution. This field could potentially drive ion flow. The calculated electric field profiled in the mid-plane of the source is depicted in Fig. 4.1. Fig. 4.1 shows the result of a Maxwell electromagnetic field solver [79] 3-D simulation of the test cell. The cell is essentially to scale and is filled with tap water. As a test case, 10 kV was applied to the central electrode in the simulation. 10 kV is approximately the highest voltage attainable with the pulsed power supply used in this study. As can be seen in the figure, field lines emerge from the surface of the powered electrode and drop off rapidly radially from the surface of the bubble into the liquid. The field at the interface is nearly 60 kV/cm. The field at this location is strong enough to locally drive ionization at the interface. Localized interface discharges were observed in this work. This field is strong enough to drive fluid dynamical effects as well, since the effective field pressure to surface tension pressure is much greater than 1. This so called electric Weber number, $W_E = \frac{\varepsilon_0 |E|^2 r_0}{\sigma}$, is large, of the order of 100 in this case, suggesting the potential for strong field perturbative effects. In the liquid, the field drops over an order of magnitude. The field patterns in solution are symmetric but not uniform in the vicinity of the bubble. However, near the grounded electrodes, the field is uniform, at least normal to the electrode edge. The field profiles can yield some insight into observed flow patterns in the cell. The field can drive ion flow in solution local to the bubble edge. For example, the mobility of

the nitrate ion in water at room temperature as inferred from electrophoresis is approximately 3.09×10^{-4} $cm^2V^{-1}s^{-1}$.[80] In the bulk region, the induced, instantaneous drift would be of order a few cm/s. Because the discharge is repetitively pulse, the actual drift speed would be somewhat less. The importance of this mobility contribution to transport can be assessed via absorption measurements to determine the density gradient. With the density gradient, the relative contribution of diffusion and mobility to overall transport can be appreciated. This is left to future work.

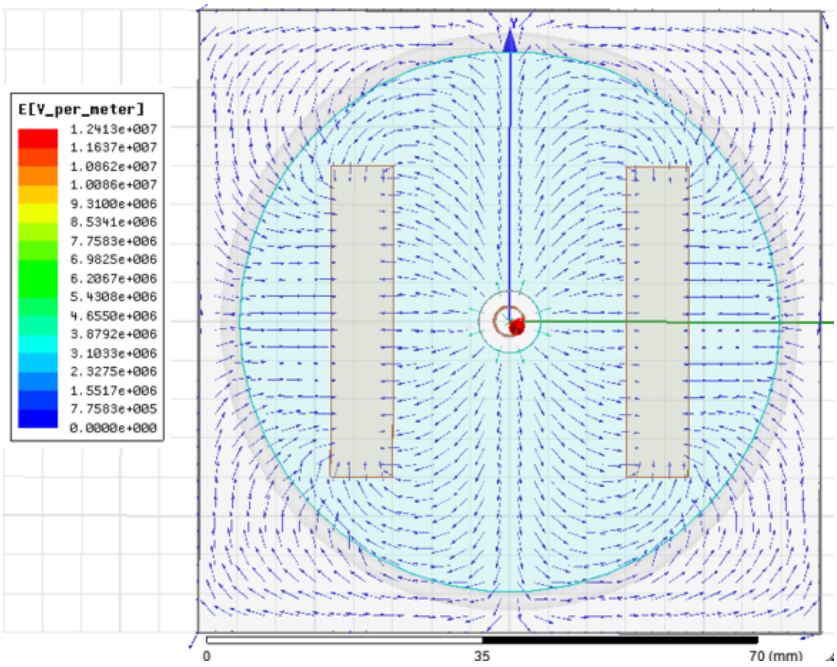

Figure 4.1: Maxwell simulation of electric field profile of 2-D bubble.

A number of chemical probes were utilized in this investigation to infer reactivity and the transport of reactivity originating at the interface, summarized in Table. 4.1. Methyl

orange, of molar concentration 2.18×10^{-3}M, was used to infer pH changes in solution. Methyl orange turns dark red when pH drops below 3.1. As it is known that acidification occurs in liquid water exposed to air plasma, methyl orange provides a direct indication of where the acidification takes place as well as the nature of the transport of those agents, such as NO, that lead to acidification [81]. ROS production and transport were interrogated using a starch and potassium iodide solution. Oxidized iodine forms a complex with the starch and in the process, gives rise to a noticeable color change, from essentially clear to blue-black. In this regard, the diagnostic is a qualitative measure of the presence of ROS and the diffusion of ROS from the interface into the bulk. This diagnostic has been used successfully in imaging ROS flux to liquid surfaces in plasma jet studies [74]. Precipitation of starch particles formed in the process yields insight on induced convection as well. The spatial progression of chemical probe color changes in time indicates the velocity of the chemically reacting front. The volume of liquid that the front has passed through is assumed reacted and only can be replenished via diffusion of new reagent. In this regard, these reagents presented here are used to study slow diffusional processes. Faster processes can be tracked using reversible chemical probes with short decay times.

Chemical probe	Concentration	Color change
Methyl orange	2.18×10^{-3} M	Red when pH < 3.1, yellow when pH > 4.4
Potassium iodide	0.117 M	Colorless to dark blue when oxidized (mixed with starch solution)
Starch solution	0.25% by weight	(see above)

Table 4.1: Chemical probes used and associated observable color change.

4.2 Voltage and current waveforms

The plasma discharge in the 2-D cell manifested itself in two general modes. These are designated: 1) the microdischarge mode, where microdischarges were observed on the surface of the powered electrode and at the gas-water interface without any visual sign of plasma filling the gap between powered electrode and water interface and 2) the streamer mode where a number of streamers bridged the gap between the powered electrode and the interface. The microdischarge mode was observed typically at lower peak voltages (around 3000 V), whereas the streamer mode was apparent at voltages somewhat higher than this for the typical bubble sizes investigated. At bubble sizes larger than 1.5 cm, breakdown was not possible over the voltage range supplied the pulsed power unit. Peak voltage and current depended on solution conductivity. For example, lower peak voltages were observed for essentially all experiments that featured the chemical probe methyl orange cases. A typical waveform structure for the microdischarge mode is shown in Fig. 4.2. The bubble associated with this waveform was oval in shape with its major diameter was approximately 15

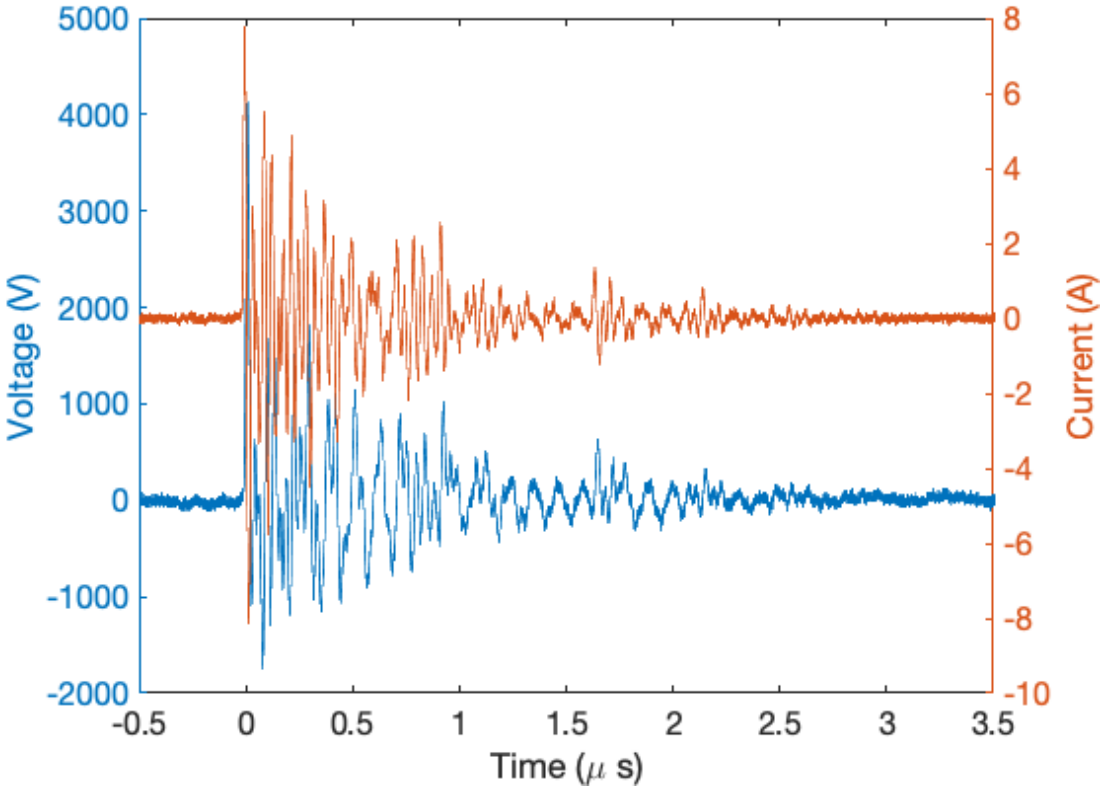

Figure 4.2: Typical voltage current pulses observed in microdischarge mode.

mm, and its minor diameter was approximately 11 mm. Apparent in both the voltage and current waveforms is considerable ringing. The ringing suggests that the circuit is underdamped in part due to impedance mismatch between the load and the source as well as the contribution of parasitic inductance and capacitance inherent in the setup. The current pulses are believed to be a combination of ringing effects coupled with the signatures of actual microdischarge formation and extinction. The characteristic frequency of the current signal ringing is roughly 7 MHz, which yields some insight into the resistance R, system in-

ductance L, and capacitance C. The characteristic frequency of an underdamped circuit is given by:

$$\omega = \frac{(4L/C - R^2)^{1/2}}{2L} \tag{4.1}$$

where the resistance R is predominantly controlled by discharge. The bubble was also excited with continuous wave AC voltage (26 kHz). There is some interest in plasma-induced effects of such discharges as they possess characteristics similar to a thermal discharge though technically, and the gas temperature was about a tenth that of the electron temperature. The low-frequency source waveform is shown in Fig 4.3 for deionized water. Displacement current is substantially smaller owing to a significant longer rise time (tens of microseconds) and the reduced conductivity contribution to charging (primarily a polarization response). The plasma current is distinguishable from the displacement current as well, seen here as a spike during the negative and positive portions of the cycle.

The AC-driven discharges tended to be streamerlike. The discharge waveform excited at 26 kHz allowed for relatively straightforward inference of the power deposited into the plasma using the Lissajous method [82]. Using a sense capacitor, it was found that the deposited power was approximately 2 W.

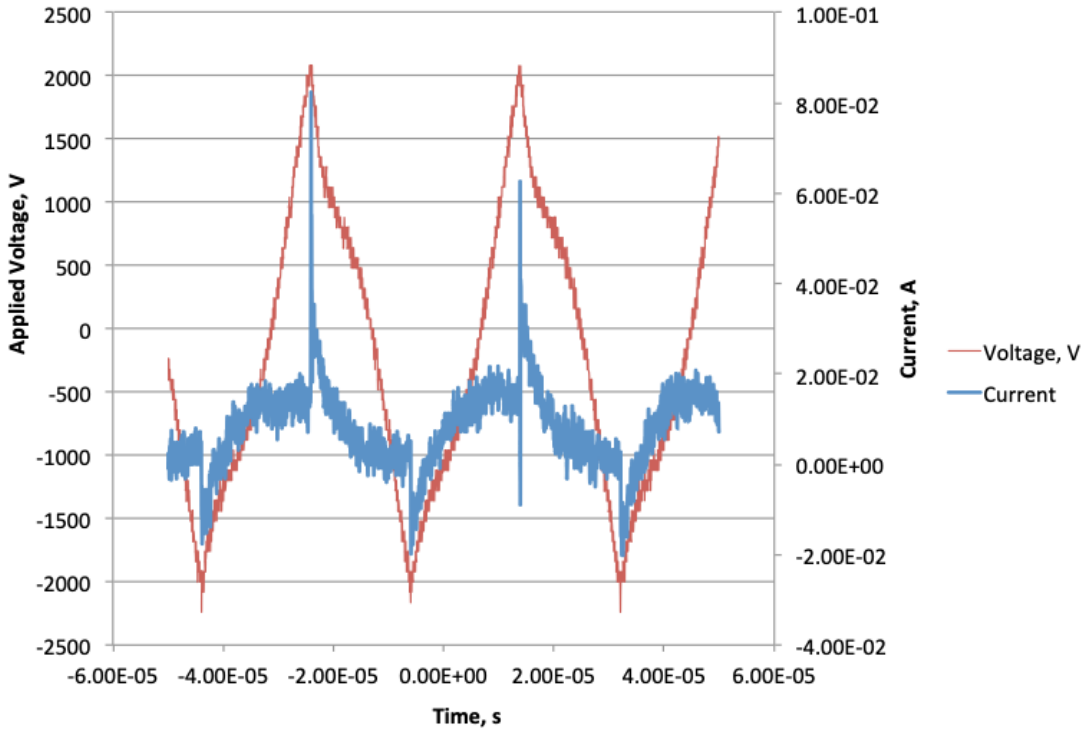

Figure 4.3: 2-D bubble current response at 26-kHz continuous wave excitation.

4.3 Chemical probes

A number of chemical probes were used to probe the reactivity driven by the interaction of the plasma with the water interface as well as infer transport in solution. In general, physical processes taking place at the interface have been discussed [83]. These include processes ranging from charging to sputtering to evaporation in addition to chemical processes, such as water decomposition, UV-driven photolysis, and acidification via oxidation of nitrogen molecules. Longer lived species, such as hydrogen peroxide, is also generated in this interfacial region. A supersaturated methyl orange solution as well as a potassium iodide-starch

solution was used to probe plasma-driven chemical and fluid dynamics derived at the interface.

4.3.1 Methyl orange

Methyl orange turns red if the solution pH drops below a pH of 3.1. A supersaturated solution of methyl orange (2.18×10^{-3}M) was used to visualize the acidification front as it propagates from the bubble-liquid interface into the bulk solution driven by plasma production within the bubble. Because the solution was supersaturated, particulates were observed at the chemical front's leading edge. Particulate formation allowed for the direct visualization of induced convection. Upon the application of nanosecond pulses at 2.6 kHz (a peak voltage of around 4100 V), a chemical front emerging from the bubble interface was observable. The front's formation is attributed to gas phase radicals produced by the localized discharge on the powered electrode, which ultimately deposit at the interface. Streamers were not observed for this condition. The front propagated slowly from the interface into the bulk solution, as shown in Fig. 4.4. In Fig. 4.4, the frames are separated in 15-second increments. Acidified regions appear dark in the grayscale images. The discoloration is noticeable in frame 2 and slowly expands outward into the liquid water with time. The expansion in this case is observed only on one side of the bubble owing to the localized nature of the discharge, that is, the microdischarge was located on the side of the electrode facing the front. The muted activity on the opposite side of the electrode is attributed to

the shadowing effect of the powered electrode and the general lack of a plasma-driven radical production on that side of the electrode. Chemical front expansion continues through frame 9. What is clearly shown here is that the origin of liquid phase activity in the bulk solution originates at the interface and propagates slowly outward. These data suggest that the observed chemical front derived from species are produced (or introduced) at the interface and propagate outward under a diffusion gradient with perhaps some degree of field-driven drift, reacting with the methyl orange along the way.

One can further speculate on the physical processes occurring in this case. Here, the microdischarges within the bubble, composed primarily of air, generate NOx species NO in particular can react with oxygen to form nitrogen dioxide. It should be pointed out that neither NO or nitrogen dioxide is very soluble in water. Indeed, they are considered hydrophobic [84]. Nitrogen dioxide, however, is very reactive with water. This rapid interaction rate leads to the production of nitrous and nitric acid (HNO_2 and HNO_3). This acidification pathway has been described starting with the following reactions:

$$2\,NO_2 + H_2O \longrightarrow NO_2^- + NO_3^- + 2\,H^+$$

$$NO + NO_2 + H_2O \longrightarrow 2\,NO_2^- + 2\,H^+$$

As the pH is lowered, nitrites can be converted into nitrates as well via the reaction:

$$4\,NO_2^* + O_2 + 2\,H_2O \longrightarrow 4\,NO_3^- + 4\,H^+$$

Because of the low diffusivity of NO and NO_2 coupled with the high reaction rate of the

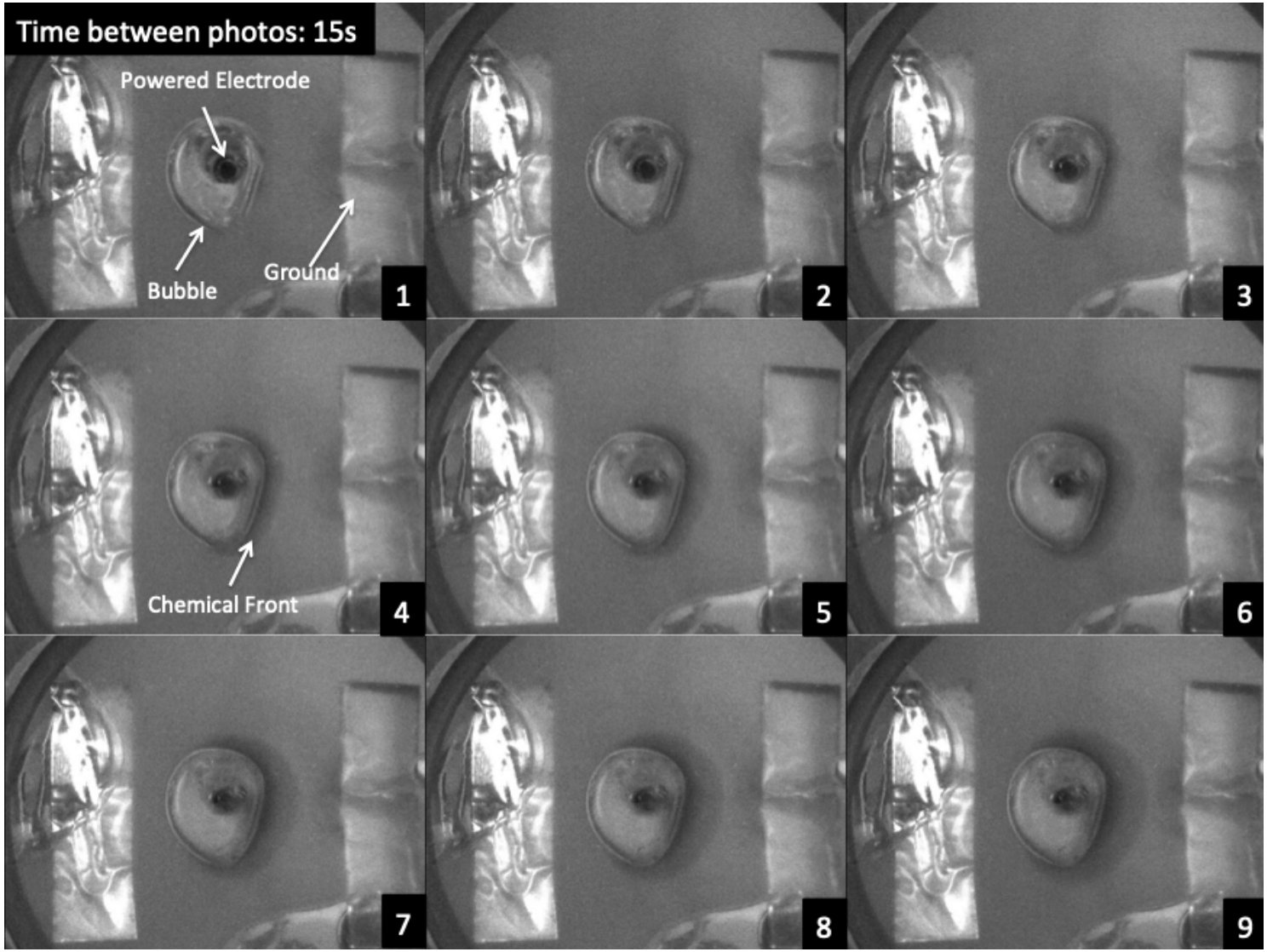

Figure 4.4: Propagation of chemical front induced by microdischarge inside bubble. (Peak voltage 4134 V at 2.6 kHz repetition rate)

NO_2, we hypothesize that the acidification must occur at the interface. Thus in this manner nitrous and nitric acids are formed via air plasma interaction with the liquid primarily at the interface. The chemical fronts observed are, therefore, a consequence of the acidic solution diffusing outward. Here, proton attachment to the methyl orange gives rise to the color change. In many respects, the color change is a measure of the diffusion of acidic components produced at the interface into the bulk. Because hydrogen peroxide can also be formed at the interface via electron impact produced OH and subsequent radical recombination, the nitrite anions can react with the hydrogen peroxide leading to the formation of other reactive species, such as peroxynitrite [85]:

$$NO_2^- + H_2O_2 + H^+ \longrightarrow O{=}NOOH + H_2O$$

At reduced pH, peroxynitrite decomposes to produce OH and NO_2^- radicals.

The data shown in the frames suggest that the chemical front is expanding radially during microdischarge mode. Fig. 4.5 shows the variation in the position of the front as a function of time along three lines oriented relative to the normal between the powered electrode and the grounded electrode with angles of 0°, 45° and -45°.

The slope of these lines yields the speed of the chemical front which yields some insight into the diffusivity of the products produced at the interface. The slopes are relatively similar yielding a flow speed of approximately 0.03 mm/s. For these experiments, the peak voltage was of order a few thousand volts. The electric field is expected to be approximately

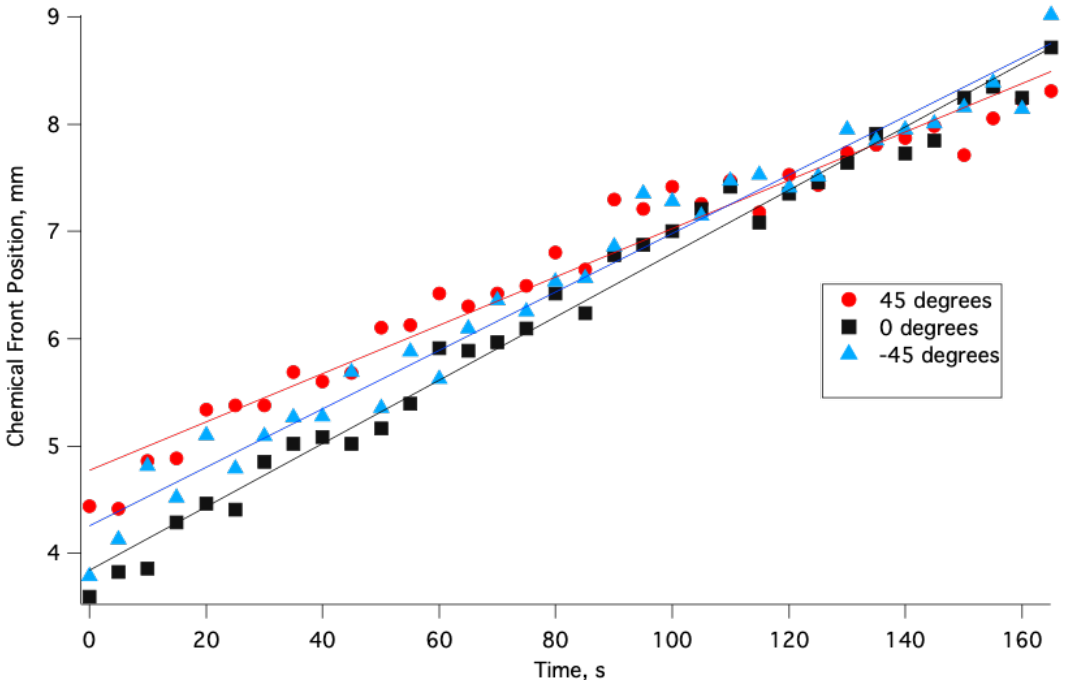

Figure 4.5: Chemical front propagation displacement as a function of time along 3 ascension angles.

20-50 times lower in the bulk than in the modeled case featuring deionized water shown in Fig. 4.1. This would give rise to a mobility associated velocity of order the magnitude measured here at least for the nitrate ion, suggesting that through mechanisms of transport are well understood, the local field may play a role in transport at least in region near the electrode. In addition, it should be pointed out that the magnitude of the measured front speed is consistent with the penetration speeds predicted for $OH^{\bullet}$, for example, via computational physicochemical models [86]. The speed of the chemical fronts appears to be relatively constant over the time range of interrogation. Because the input power is constant, the density gradient at least in the near field driving the diffusion should be relatively

constant leading to a constant speed of the chemical front. It is important to point out that the chemical front leading edge represents the boundary between the reacted and unreacted methyl orange. These data, therefore, yield some insight into the speed at which acidification occurs. These data suggest that a point source discharge could acidify a 100 mL beaker of liquid (2.5 cm radius) completely in of order 10 min assuming similar powers. Interesting, this time scale is of order that associated with pH saturation in plasma treated liquid studies, that is, the time constant associated with the pH change is of order 10 min [87]. Though difficult to quantify with nanosecond pulsed discharges, some insight into transport may be gleaned from varying input power. Power absorbed, however, in such small discharges driven by nanosecond pulses unfortunately is difficult to quantify. In this experiment, the input frequency was fixed, because, in general, discharge character changes with frequency thus making it difficult to separate plasma effects (temperature, reaction rates, discharge size and intensity) from simply radical source function effects.

For comparison purposes, it is pointed out that the chemical diffusion front speeds vary depending on shape of the front. It was found that flat stable fronts in autocatalytic cells travel at a constant speed of approximately 30 μm/s, the same order of magnitude of the chemical fronts observed in this experiment, suggesting similar dynamics [88].

The plasma interaction at the interface was also observed to drive fluid dynamical effects. Such effects were observed primarily when the apparatus was operated in the streamer

mode. As the applied voltage is increased to the powered electrode, the discharge transitions from the microdischarge mode to streamer mode. In the streamer mode, the attachment at the interface is sometimes asymmetric, meaning that the attachment has a preferred direction, as shown in Fig. 4.6. This asymmetry is likely related to the electric field distribution in the bubble, which in turn is driven by bubble shape and the centering of the bubble relative to the powered electrode. As can be seen in frame 1, the chemical front associated with the microdischarge is apparent. But, at higher voltages, once the microdischarge transitions into streamers, a rather dramatic color change in the methyl orange is observable as can be seen in frame 2. This is presumably due in part to increased NO production associated with the higher plasma density streamer discharges. The streamers at later times (starting in frame 4) appear to drive a circulation pattern originating at the interface. The circulation pattern extends nearly to the grounded electrodes. These large-scale structures appear to be associated with forced convection. The convection trails, however, in this case are chemically active, as inferred by the noticeably darkened circulation tracks. Apparently, when streamers are present, this circulation is observed. The diffusion of the chemical front into the bulk is also faster (note that the time between frames is 1 s in contrast to 15 s, as shown in Fig. 4.4 in contrast to the purely microdischarge case.

In addition, over time, the precipitates of presumably oxidized methyl orange are observable. Some of these particulates venture into the circulation patterns and are entrained in

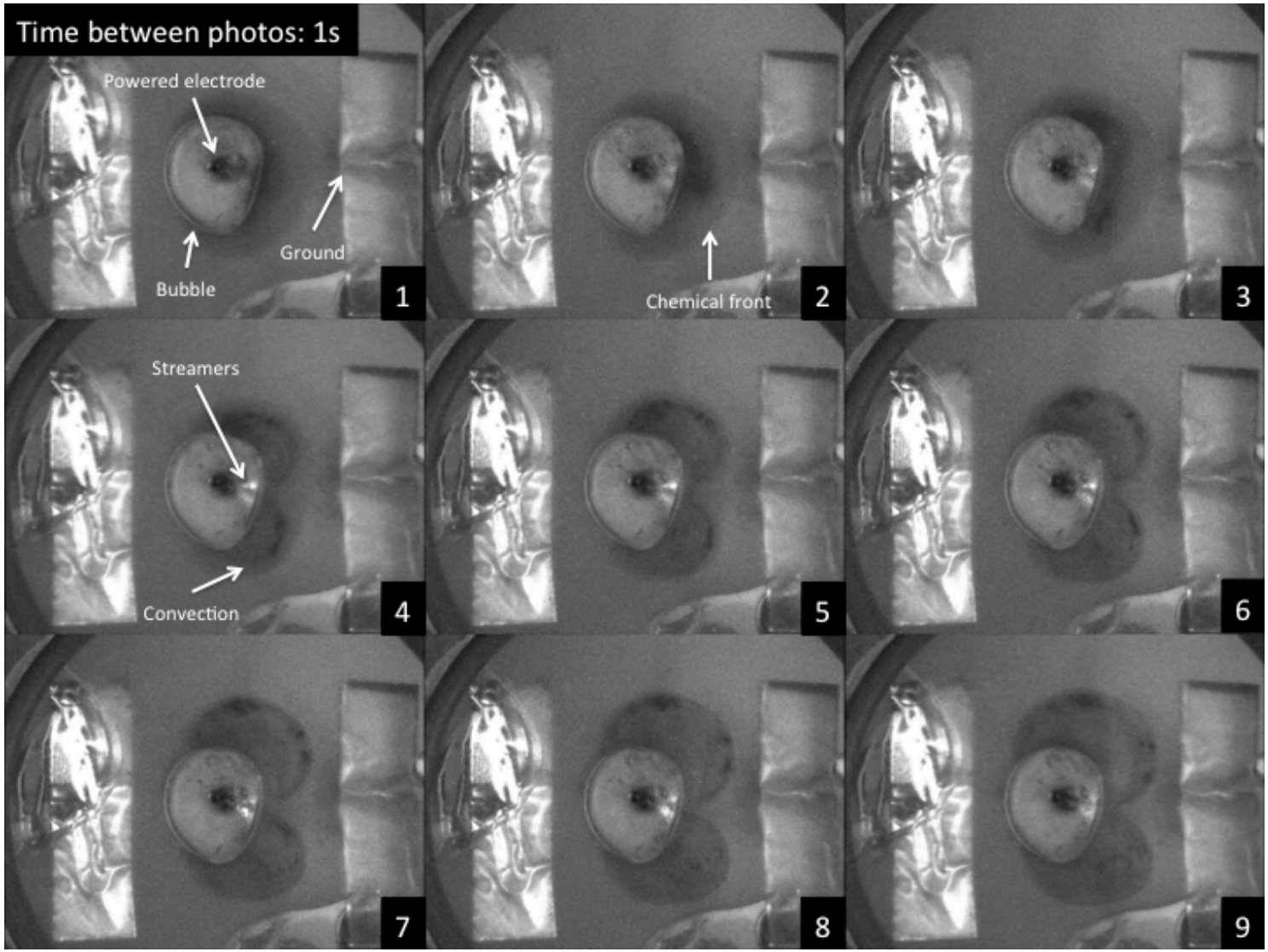

Figure 4.6: Streamer-induced convection, noticed the two-lobed structure circulation pattern. Pattern apparently entrains particulates.

the circulating flow. This observation confirms that the swirl-like patterns are indeed flow patterns. The flow patterns form two lobes associated with each streamer attachment point, that is, the circulation lobes appear to originate at the streamer termination point at the interface. In this regard, these data suggest that streamer-water interaction is not simply radical production and diffusion at the interface; rather, the interfacial interactions appear to be more complex. Apparently, body forces originating at the interface drives the large-scale circulation. This driven circulation enhances the transport of reactants into the bulk. In this case, nitric and nitrous acid produced at the interface are driven into the bulk via body forces originating at the interface.

In real systems, such induced transport if present would shorten treatment times. The plasma-water interaction in this regard is not static. The particles that diffuse near the bubble surface are driven circumferentially around the bubble. This suggests that the body force acts circumferentially as well at least local to the interface. The origin of this force is not well understood at the moment. It is possible that ion impact momentum exchange at the streamer had could be driving the flow.

In addition, the intermittent acting of the streamer head at the interface may give rise to a body force. In this case, the electric field at the streamer head can drive capillary waves that can propagate along the circumference of the bubble [89]. The behavior of the swirl pattern is reminiscent of a jet of fluid propagating through a denser medium. What is clear,

however, is that the body force driving the acceleration acts tangent to the bubble's boundary. Surface tension effects cannot be discounted here. The localized attachment of the streamers will no doubt give rise to a gradient in surface tension at the interface. The associated tangential sheer stress is known to give rise to bulk fluid motion. Surface tension gradients would give rise to body forces at the interface. This so-called the Marangoni effect is associated with induced flow due to surface tension gradients [90]. It is likely that the observed circulation is due in part to this effect.

It is interesting to note that circulation patterns (convection) have been observed in a number of discharge experiments [91, 92]. In these experiments, circulation due to plasma jet interaction at the liquid surface drives bulk circulation. Marangoni effects at the surface may drive this circulation as well. Indeed, the circulation patterns observed here are reminiscent of those predicted by Taylor [93]. Taylor [93] theoretically predicted that similarly observed circulation patterns arise in the presence of an electric field due to a balance between electric stress and a variable pressure difference between the inside and outside of the bubble. This difference can exist only if the fluid is in motion, the observed circulation. The circulation patterns observed in this paper, therefore, provides some insight into the circulation patterns observed in larger scale experiments.

It is possible to estimate at least qualitatively the magnitude of the induced flow by tracking the behavior of precipitated particulates in solution. The trajectory and the instanta-

neous speed of the particulates give insight into the nature of the actual velocity flow field. Fig. 4.7 shows the outline of a trajectory of one such particle. This representative particle's

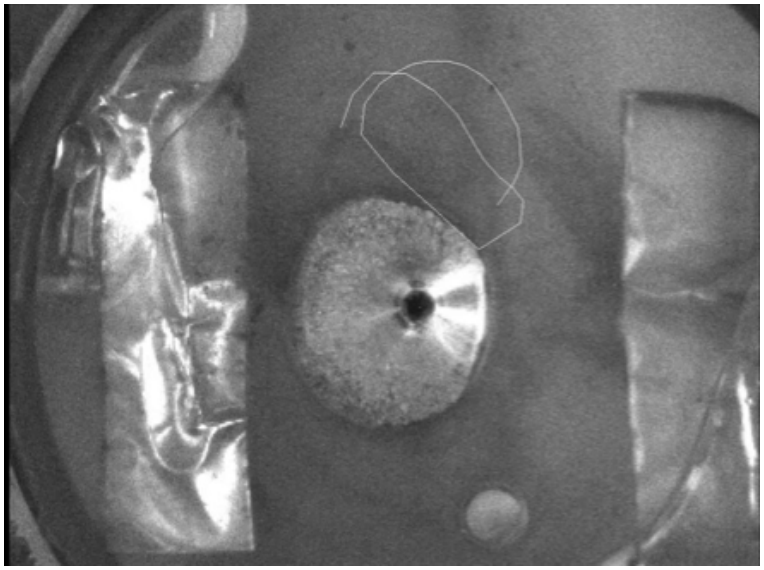

Figure 4.7: Representative trajectory (white line) of a precipitate particle entrained in streamer induced flow field. Note that t = 0 corresponding to tracking start point.

trajectory carried it near the interface as well as through the bulk region. Fig. 4.8 shows this particle's instantaneous speed and position relative to the location of the powered electrode as a function of time. As can be seen here, the particle's speed away from the central electrode is somewhat constant, either 2 or 4 mm/s depending on location away from the interface. However, near the interface, the particle speeds up significantly, suggesting that the flow field is nonuniform in this region. Indeed, near the interface, the particle's speed increases by an order of magnitude. This interesting behavior can be quantified in detail using particle imaging velocimetry to fully detail the flow field and thus elucidate the true

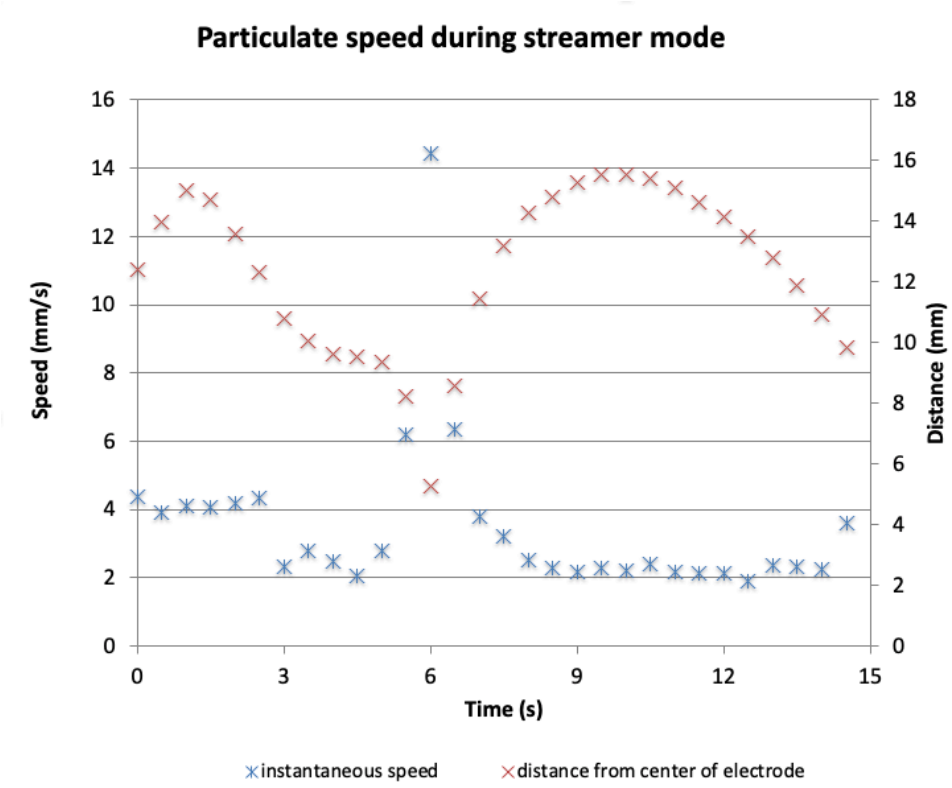

Figure 4.8: Instantaneous precipitate flow speed along with radial distance relative to the electrode as a function of time.

nature of the force at the interface. This is left to future work.

Also observed in these experiments was the ballistic ejection of interface-produced acidic solution into the bulk liquid. That is, a discrete packet or portion of the interface is essentially blown off. This was observed, as shown in Fig. 4.9, when pulsing the electrode voltage. Here, as can be seen in the photographs, a parcel of reactive fluid is ballistically ejected into the bulk. The fluid packet maintains its structure. These visual data, shown in Fig. 4.9, illustrate the action of the body force at the interface driven by the pulsed streamer and the

reactivity at the interface. The images suggest that a faction of treated fluid is torn from the interface forming essentially an island of reactive fluid. What makes this set of images unique is that we observe the effect of a short duration pulse. The separated parcel of fluid remains relatively unchanged over long time scales (over 1 second). The lack of a trail of darkened solution is a consequence of the fact that the streamer is no longer present after the ejection to produce species necessary to support acidic species. The acidic fluid is simply ballistically ejected into the bulk. Here, the reactive nitrogen species (RNS) have reacted with the methyl orange at the interface, locally exhausting active reagent (in the packet), and thus, no trail is observed. Again, the data suggest that body force evacuates the treated fluid. Because the streamer is not maintained, this fluid is not entrained, as the convection field is not yet established. This observation suggests that the interface is dynamic with reactivity being generated locally but spread to distant locations via other forces. In this respect, transport is not as simple as simple diffusion. Transport apparently depends on discharge type, whether streamer or microdischarge.

4.3.2 Potassium iodide and starch

While it is of interest to understand the nature of chemical transport and processes such as acidification, it is equally of interest to determine the nature of the radicals produced at the interface. In particular, the transport of reactive oxygen species (ROS) is of interest as it drives decomposition reactions for water purification applications or microbial steriliza-

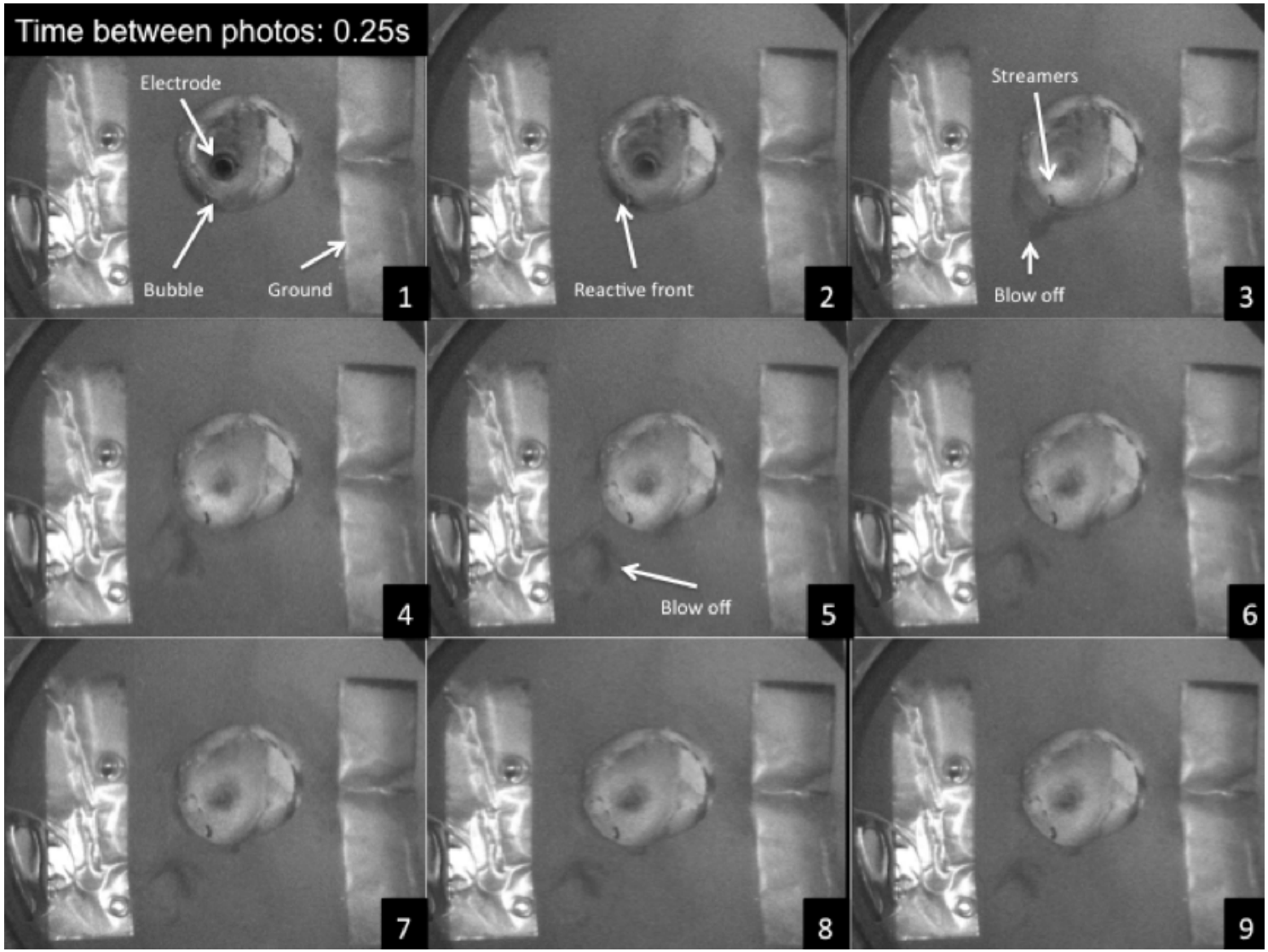

Figure 4.9: Ballistic ejection of reactive fluid from the interface (single shot).

tion for medical applications. A potassium iodide (KI) and heat-dissolved starch solution in tap water was prepared to detect the presence of ROS. Heat has been proved to help increase amylase percentage in iodine, which improves reaction rates. Iodine in the presence of hydrogen peroxide for example forms tri-iodide ions. These ions forms a complex with amylase in starch leading to a color change, in this from clear to blue-black. For example for hydrogen peroxide produced at the interface, the interaction proceeds as:

$$2\,I^- + H_2O_2 + 2\,H^+ \longrightarrow I_2 + 2\,H_2O$$

$$I_2 + I^- \longrightarrow I_3^-$$

$$I_3^- + \text{starch} \longrightarrow \text{starch} - I_3^- + I^-$$

While a great deal of ROS activity takes place at the interface owing to the short lifetimes of OH and superoxide, longer lived species, such as hydrogen peroxide, can diffuse deeper into the medium and react along the way. In this case, the leading edge of the chemical front would be associated with long-lived ROS flow into the bulk. Fig. 4.10 shows the behavior of the solution upon application of voltage (a peak voltage of 6.8 kV). Multiple streamers clearly are observable in frame 3 along with a darkened region at the bubble-solution interface. The discoloration tends to be more pronounced in those regions on the same side of the discharge attachment at the interface. In this case, two lobes are apparent early on. Interestingly, circumferential flow driven around the interface by the streamers is also apparent. This flow spreads the oxidized complex around the perimeter of the bubble.

The intrusion of the reactivity into the presumably unaffected solution is not in the form of uniform radial expansion; rather, expansion is associated with swirl patterns.

This behavior is associated with the body force driven flow at the interface. Also observable at later times is the monotonic expansion of the chemical front into the volume. The processes observed here takes place on a time scale of seconds. The new insight gleaned here is the circumferential flow that spreads the reactivity and leads to circulation of the chemical front. Again, both chemical probes suggest that the interface is not just the source of chemical reactions, but depending on the nature of the plasma excitation, body forces are apparently present at the interface, which presumably drives mixing and thus the rate at which the solution is treated. Fluid dynamical effects, therefore, cannot be discounted in regard to assessing the transport of reactivity into the bulk solution.

4.3.3 Emission spectra

Emission spectra were acquired directly in the bubble region using an optical fiber with lens attachment. The spectral distribution tended to change over time. For example, the plasma emission in the bubble was monitored as a function of time for the KI solution, as shown in Fig. 4.11.

The relative intensity of the nitrogen emission lines tended to decrease over time. The relative intensity of the hydrogen and oxygen lines tended to increase over time. In general, nitrogen solubility in water is poor, roughly half that of oxygen. The decrease in nitrogen

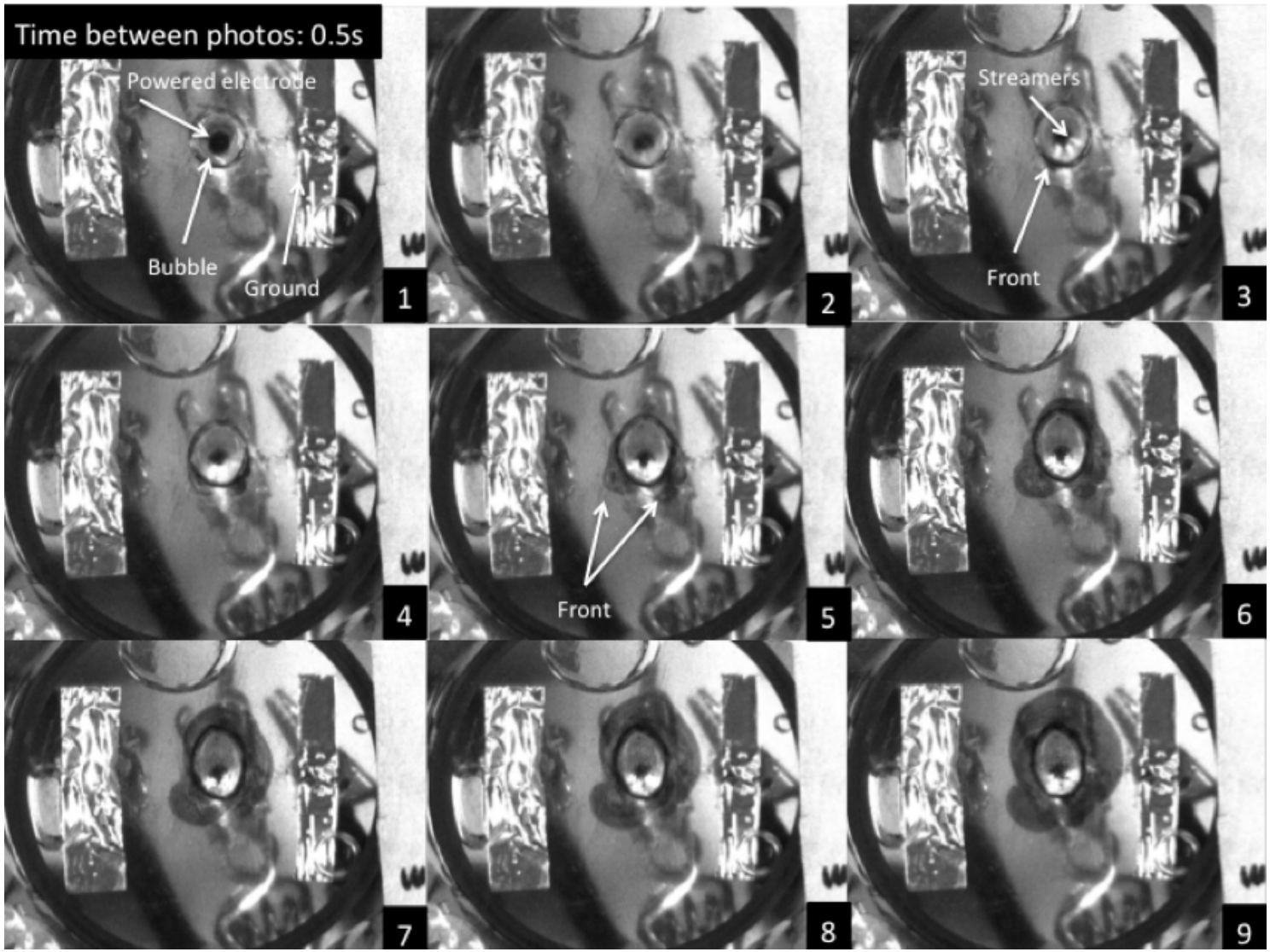

Figure 4.10: Reaction of KI-starch solution with ROS.

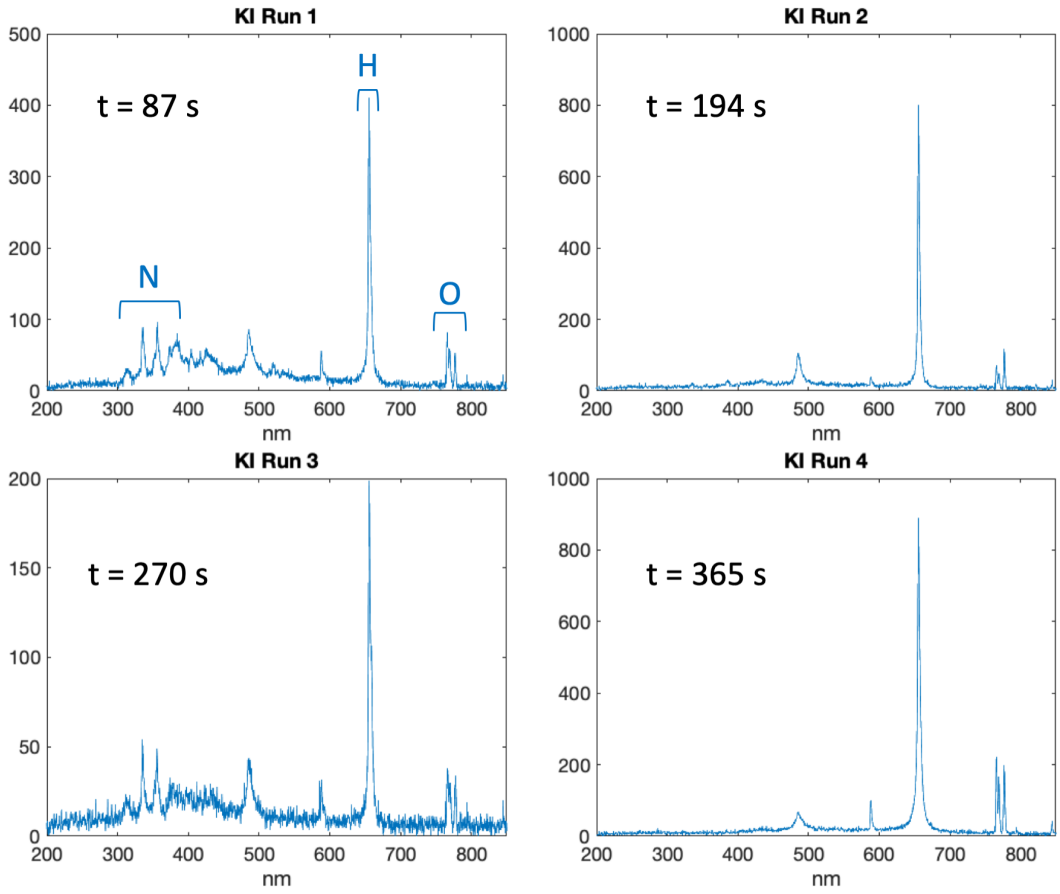

Figure 4.11: Emission spectra from 2-D streamer bubble in KI solution.

emission is attributed to the formation of nitrogen-based gas phase species that essentially remove free nitrogen. Some of these products have fairly large Henry's law constants and are thus lost to solution (e.g. NO_3, HNO_3, and N_2O_3) [94]. The fact that this apparent consumption is observable is attributed to the manner in which the gas was introduced to make the bubble. The bubble gas is supplied by the syringe (finite volume gas reservoir), so the amount of nitrogen and indeed all gases with access to the discharge is finite. Inevitably,

the nitrogen partial pressure is selectively reduced owing to gas phase plasma-driven reactions and subsequent dissolution into the surrounding liquid.

The increase in the hydrogen (656 nm) and oxygen (777 nm) emission is most likely due to increased water vapor partial pressure via diffusion from the surrounding liquid due to perhaps localized heating. The water is broken up into constituent atoms via plasma action. This apparently occurs in this case after a little over 190 seconds of operation. These effects can be observed visually as well by observing the bubble size, which tends to shrink over time. Presumably, this occurs as the air is lost to the liquid. At 270 second, the pressure in the bubble was increased by depressing the syringe connected to bubble. This presumably increased the partial pressure and, thus, the density of nitrogen in the bubble. The resulting spectra clearly show the presence of nitrogen emission.

In the case of discharges in bubbles, gas composition and relative solubility can be expected to play a key role in resulting chemistry. For a given bubble, the amount of specific reactivity that can be achieved by subsequent breakdown pulses will obviously reduce over time. For single bubble studies, it is, therefore, important to monitor actual partial pressures as these can be expected to change over time. If one could measure the evolution of the partial pressure of the gases with time, then it is should be possible to infer resulting chemistry in the interface. Alternatively, if the goal is to maintain a constant partial pressure of nitrogen for example, an inline flow controller could be utilized.

Chapter 5

Effects of feed gas and the production of ozone

In this experiment, we used chemical probes to visualize pH changes and oxidative species production at the interface due to discharges inside air and argon bubbles. The production and transport of oxidative species such as ozone and hydroxyl radicals were measured using a dye in combination with absorption spectrophotometry.

5.1 Methods

The 2-D discharge cell (with both flat and ring electrodes) used in this experiment is described in Section. 3.2. The electrode was connected to a nanosecond pulsed power supply (FID GmbH, FPG 10-10KM), which supplied the cell with voltage pulses up to 10 kV at a repetition rate of several kHz. In this work, the repetition rate used is 1.89 kHz, and the voltage and current waveforms of a typical pulse are shown in Fig. 5.1. To vary the gas type

used in the cell, an opening was made on the body of the syringe connected to the stainless steel tube, allowing the syringe to be filled with either air or argon gas. Bubble diameters used in this experiment ranges from 4.35 to 7.82 mm.

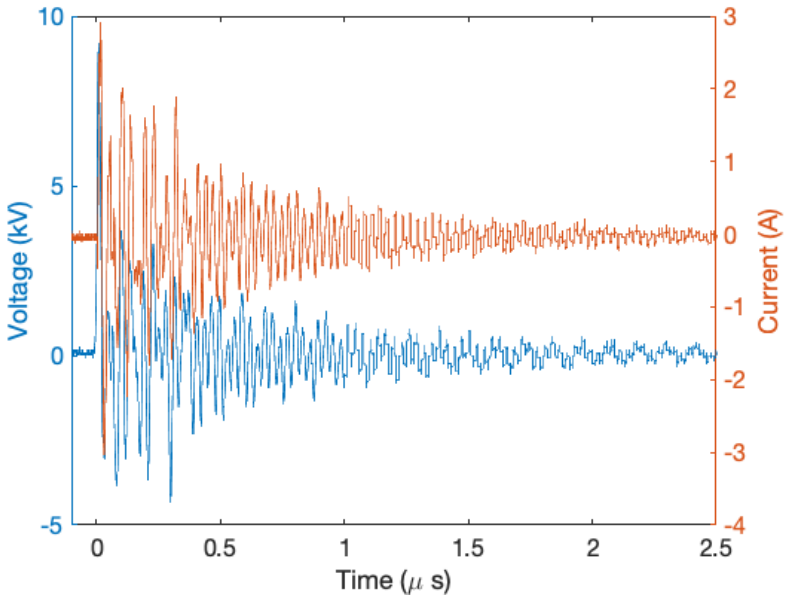

Figure 5.1: Voltage and current waveforms of a typical pulse.

Chemical probes were used to visualize various chemical fronts. Methyl orange solutions were used to show pH changes in the liquid. Methyl orange solutions appear as different colors as the pH changes: yellow when pH>4.4, red when pH<3.1, and orange in between.

Solutions with dissolved starch and potassium iodide (KI) were used to indicate the presence of oxidative species, such as hydrogen peroxide. Hydrogen peroxide oxidizes iodide ions in solutions to form iodine and potassium hydroxide,

$$H_2O_2 + 2\,KI \longrightarrow I_2 + 2\,KOH$$

The iodine further reacts with iodide ions to form triiodide ions,

$$KI + I_2 \longrightarrow KI_3$$

Starch molecules react with triiodide ions to form a blue-black colored complex. This color change from colorless to blue-black occurs when oxidative species are produced.

Indigo trisulfonate in solutions appears dark blue, but the solution turns colorless when oxidized. While indigo trisulfonate does not react with hydrogen peroxide [95], it reacts with aqueous ozone at a reaction rate of 1×10^7 $M^{-1}s^{-1}$ [96, 95], and is frequently used as a chemical probe for aqueous ozone. [97, 98, 99] Hydroxyl radicals can be formed as ozone decomposes in water, and are highly oxidative. [100] Hydroxyl radicals react with aliphatic and aromatic compounds with reaction rates reaching the order of $10^8 - 10^9$ $M^{-1}s^{-1}$, thus are suspected to also react with indigo trisulfonate at a high rate. [101, 102] In this study, we will attribute the discoloration of indigo dye to the reaction with both aqueous ozone and hydroxyl radicals.

The indigo dye has a strong absorbance at 600 nm with a molar extinction coefficient of $23,000$ $M^{-1}cm^{-1}$ [95]. Absorption spectrophotometry of indigo trisulfonate was performed to quantify the production and transport of oxidative species. The experimental set-up is shown in Fig. 5.2; a light source (AmScope 150 W fiber optic halogen illuminator) and mirror (Edmund Optics 75×75 mm protected silver, $\lambda/4$ mirror, stock # 88-541) were used to back light the cell. A 600 nm filter with a full width-half maximum of 10 nm was

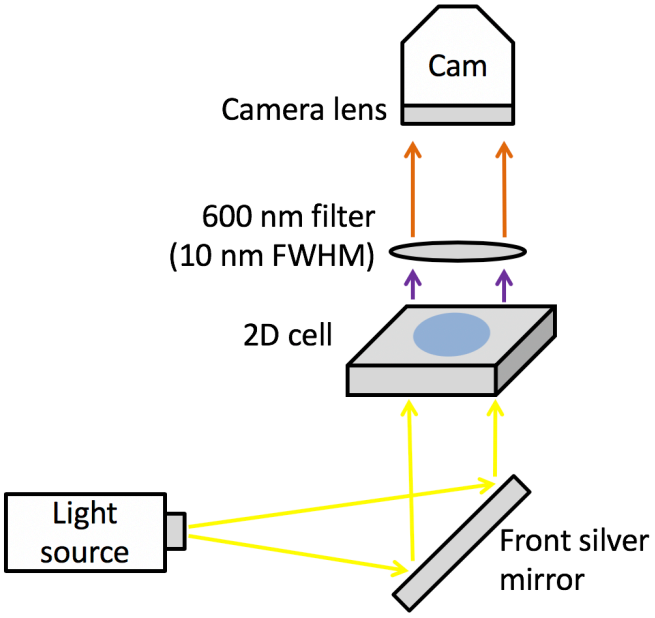

Figure 5.2: Experimental set up of spectrophotometry.

used to isolate the light transmission at the target absorption wavelength. As indigo trisulfonate was consumed, less light was absorbed, and the measured light intensity increased. The amount of oxidative species produced can be inferred from the measured light intensity at 600 nm. Transmitted light for absorption spectrophotometry was recorded using a fast camera (Photron FASTCAM UX-100) with a resolution of 1280 × 1024 and capable of recording 8,734 frames at 50 frames per second (fps). Chemical front measurement in methyl orange and potassium iodide-starch solutions was recorded using a Nikon DSLR camera. A Nikon 60 mm f/2.8D DSLR camera lens was used in combination with both cameras.

5.2 Results and discussion

5.2.1 Comparison of colorimetric probe responses due to air and argon discharge

Air is a composite gas composed of approximately 78% nitrogen, 21% oxygen, 1% argon and other gases. As such, air plasma contains an extensive variety of excited and charged species. In particular, reactive oxygen and nitrogen species can diffuse through the interface into bulk liquid but can also initiate chemical reactions at the interface and produce reactive aqueous species. The extensive variety of reactive species contributes to the complex plasma chemistry at play at the interface. In order to elucidate the various chemical processes at play, we compared the responses of colorimetric probes due to both air and argon plasmas. Argon is a rare gas, and when excited, produces excited states of argon metastables, argon ions, and electrons. Argon allows for a reduction in the magnitude of plasma-induced chemistry pathways due to the limited number of present active species. Therefore, the use of argon simplifies the reactions induced at the interface and can provide insight to the chemistry of plasma-derived reactivity in liquids.

5.2.1.1 Acidic front propagation measured with methyl orange

Methyl orange solution is sensitive to pH changes. As the solution becomes more acidic and more hydronium ions are available, methyl orange becomes protonated and its molecules

appears red in solution. When methyl orange solution was used as a bulk liquid in the 2-D cell, it was shown that an acidic front, indicated by color change in solution, was observed when streamers were excited inside the bubble. [103] This color change was captured using a DSLR camera and is shown in Fig. 5.3.

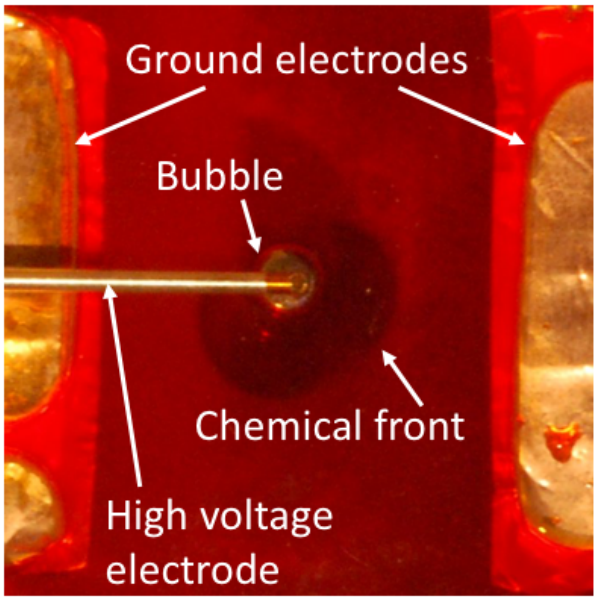

Figure 5.3: Acidic front in methyl orange solution.

Fig. 5.4 shows acidic front propagation in the air bubble experiments. Significant dark red colored acidic front propagated from the bubble surface outward. Asymmetry of the acidic front in bulk liquid, concentrated on the lower region, was likely due to the bubble not being concentric with the high voltage electrode. This led to streamer discharges localized in the lower half of the bubble, initiating an acidic front in that region as well. Air plasma typically produces a large amount of NOx species. The diffusion of nitric dioxide

species at the interface can interact with hydrogen peroxide and water to form both nitrous and nitric acids. These acids can then react with methyl orange, leading to the observed color change. The acidic front propagation was measured using image processing software

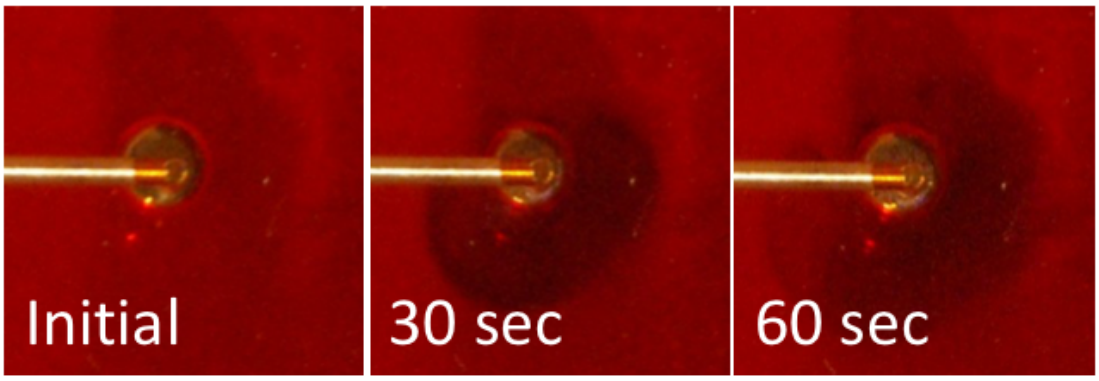

Figure 5.4: Acidic front initiated by air plasma.

ImageJ. The acidic front location measured from the bottom bubble boundary is shown in Fig. 5.5. The measured front speed, at 0.46 mm/s, was high in the first 10-second period but slowed down subsequently.

The NO mechanism for acidification should have been absent in the argon bubble plasma. However, as shown in Fig. 5.6, an acidic front was observed in bulk liquid when the bubble was filled with argon gas instead of air. Bubble enlargement after plasma excitation was observed for cases with argon filled bubbles. For ample hydronium ions to be produced at the interface, another acidification mechanism is suggested. Positive water ions ($H_2O^+_{(aq)}$) can be produced through photoionization and charge exchange with positive argon ions. The positive water ions can undergo further charge exchange reactions with water

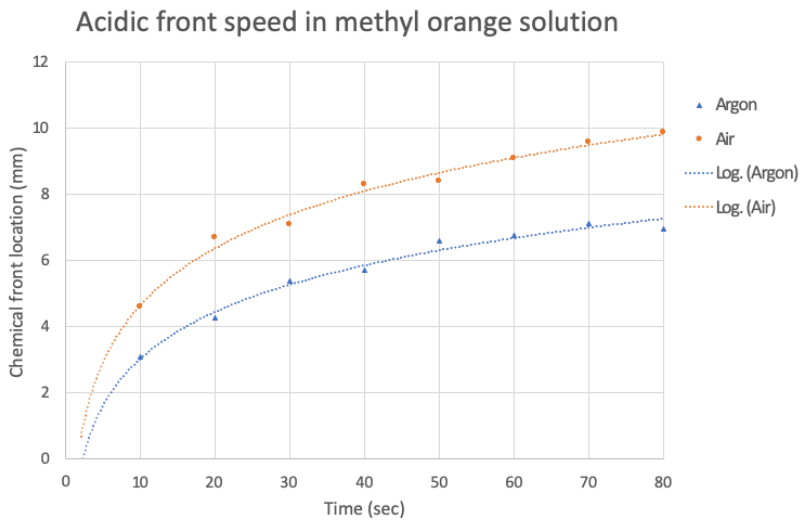

Figure 5.5: Measured acidic front location in methyl orange solutions initiated by both argon and air plasmas.

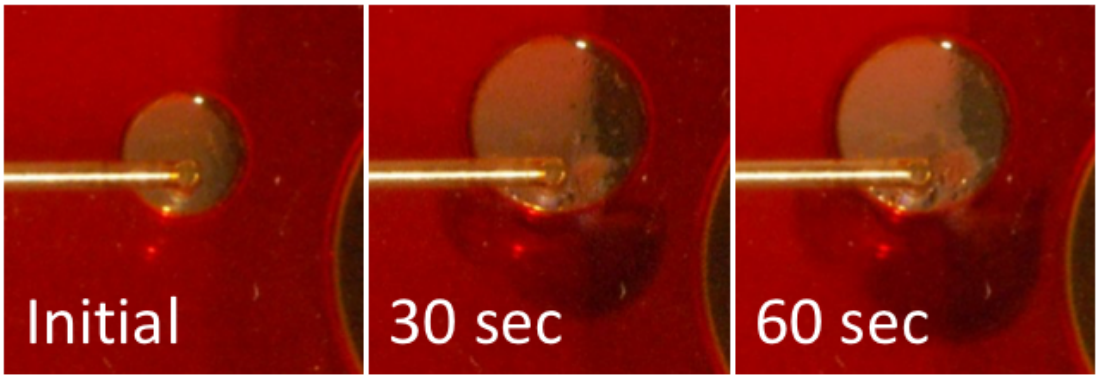

Figure 5.6: Acidic front initiated by argon plasma.

to form hydronium ions and hydroxyl radicals:

$$H_2O_2 + h\nu \longrightarrow H_2O^+ + e^-$$

$$Ar^+ + H_2O \longrightarrow Ar + H_2O^+$$

$$H_2O^+ + H_2O \longrightarrow H_3O^+ + OH^\bullet$$

The acidic front propagation due to argon plasma is also shown in Fig. 5.5. Its instantaneous speed in the first 10-second period was found to be 0.31 mm/s.

The differences in front speeds (0.46 mm/s for air bubble and 0.31 mm/s for argon bubble) may have been due to the variation in bubble sizes and the proximity of the bubble boundary to the high-voltage electrode, both of which arise from discrepancy in the manual process of bubble injection. Slight shift in the bubble location will significantly alter the discharge gap, resulting in variation in the propagation of streamers. This asymmetry of streamers' location impacts the induced chemistry, and ultimately contributes to variations in the observed flow speeds.

5.2.1.2 Production of oxidative species measured with potassium iodide and starch solution

Plasma discharges can produce various oxidative species when coming in contact with water. [59] This includes short-lived species, such as hydroxyl radicals and singlet oxygen, and long-lived species, such as hydrogen peroxide and nitrates. These species can oxidize iodide ions in solutions to form iodine. If an ample amount of potassium iodide is dissolved in the solution, iodine will react with iodide ions to form triiodide ions. Starch solution, while unreactive to iodide ions, will react with triiodide ions to form a blue-black complex. This reaction was observed in previous experiments when streamers were excited in the 2-D cell. [103] The oxidative front was captured using a DSLR camera, as shown in Fig. 5.7.

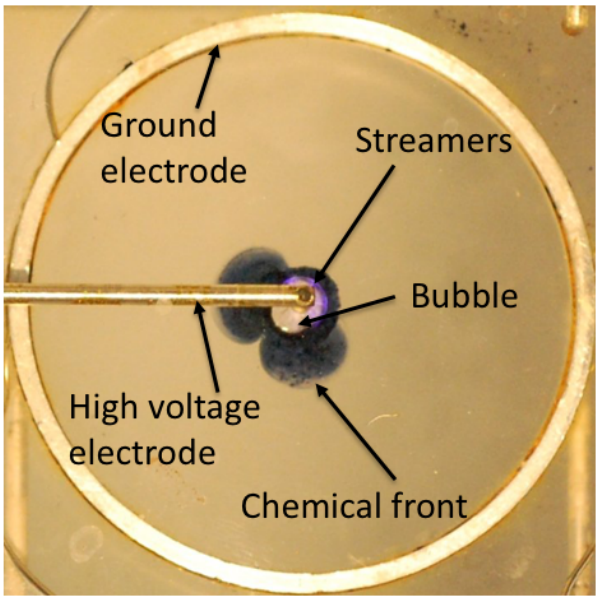

Figure 5.7: Oxidative front in potassium iodide-starch solution.

Oxidative front propagation in the air bubble experiment is shown in Fig. 5.8. Streamers were present in the lower left region of the bubble, and blue-black complexes surrounded the bubble in the liquid region. While the fluid flow of the blue-black complex is not within the scope of this study, the oxidative front propagated further into the liquid region over time. The presence of oxygen and nitrogen in air led to the formation of oxidative species, such as ozone, nitrates, and hydrogen peroxide in the liquid region. These species then reacted with potassium iodide and the starch solution to form the color change observed.

In the absence of nitrogen and oxygen in argon gas, reactive nitrogen species cannot form in the gas phase discharge region, whereas reactive oxygen species can only form as a result of presence of water vapor in the bubble. As shown in Fig. 5.9, an oxidative front was ob-

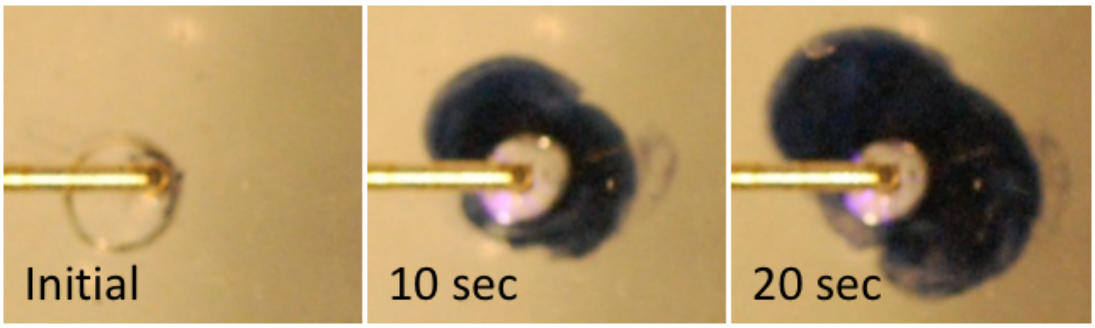

Figure 5.8: Oxidative front initiated by air plasma.

served in bulk liquid when discharges were produced in the argon bubble. This can be attributed to the production of hydroxyl radicals in the gas phase discharge, but the production of oxidative species at the interface when streamers came into contact with the liquid layer can play a role as well. Electron impact ionization at the interface leads to the formation of hydroxyl radicals, which is a short-lived oxidative species, and can combine to form the long-lived oxidative species hydrogen peroxide. As mentioned in the previous section, hydronium ions can also be formed at the interface. The acidic environment, in combination with the formation of an oxidative species, allowed a triiodide ion to form and be trapped by starch molecules. An observable color change in solution also indicated that in-situ reactive oxidative species production at the interface contributed significantly to generation transport of reactive species into the liquid region.

The propagation front was measured using image processing software ImageJ [104]. The front locations from the boundary of the bubble are shown in Fig. 5.10. The instantaneous

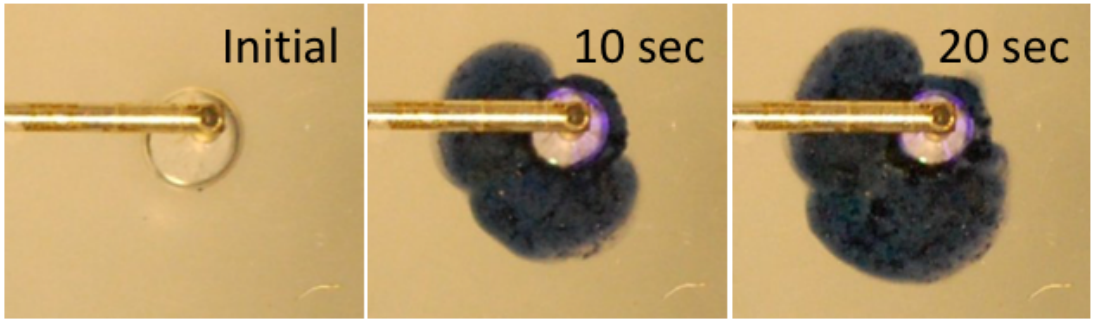

Figure 5.9: Oxidative front initiated by argon plasma.

speeds of the oxidative fronts for the first 10 seconds were 0.55 mm/s and 0.51 mm/s for air and argon plasmas respectively, which is consistent with the penetration speed of aqueous ROS reported at 2.2×10^{-5}m/s, by [86]. While differences in bubble sizes and streamer formation can affect flow speed, it is likely that air plasma leads to higher production of oxidative species in water. This scenario can lead to a higher chemical concentration gradient, producing a surface tension gradient in the area surrounding the bubble and increasing the induced flow speed.

5.2.2 Production and transport of oxidative species measured with indigo trisulfonate

In the published method used to quantify aqueous ozone, potassium indigo trisulfonate ($C_{16}H_7K_3N_2O_{11}S_3$) reacts with aqueous ozone stoichiometrically, as shown in Fig. 5.11 [95]. As such, the change in the absorption measured can be correlated to the amount of indigo trisulfonate consumed. Calibration was performed by imaging the light transmis-

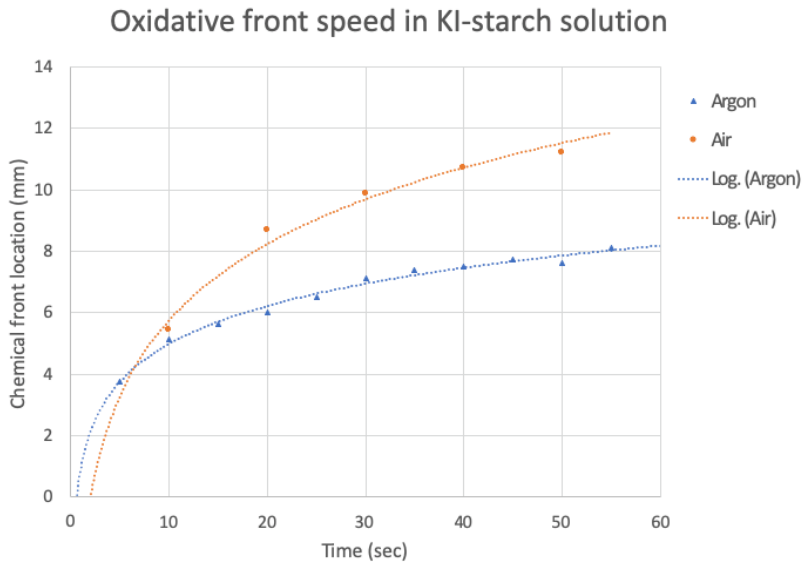

Figure 5.10: Measured oxidative front location in KI-starch solutions initiated by both argon and air plasma.

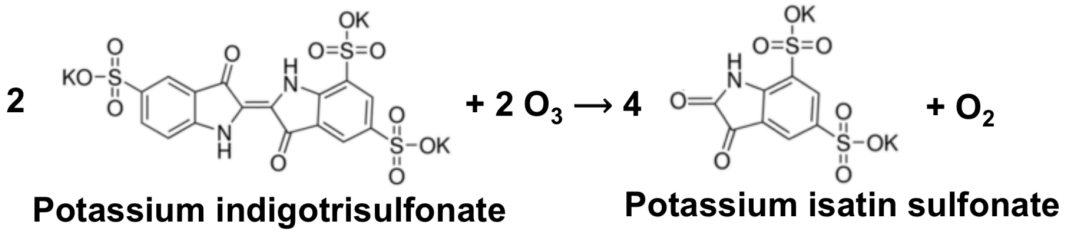

Figure 5.11: Reaction between indigo trisulfonate and aqueous ozone.

sion through known concentrations of indigo trisulfonate. Measured light intensity was then converted to the concentration of indigo trisulfonate in the liquid layer, thus allowing for the calculation of the amount of dye consumed and the concentration of oxidative species produced. Images recorded with fast camera were exported as TIFF images and analyzed using MATLAB. An unprocessed sample image is shown in Fig. 5.12(a), and the post-processed image is shown in Fig. 5.12(b). A high-voltage electrode was inserted through the

top quartz plate, which obstructed part of the liquid layer and most of the bubble region. The electrode is shown on the left of both images. The bubble region, outlined with dashed lines, allowed some light to come through, which appears orange in Fig. 5.12(a) and red in Fig. 5.12(b). While a chemical front cannot be observed by the naked eye in Fig. 5.12(a), the slight difference in light intensity was amplified using the MATLAB script as seen in Fig. 5.12(b).

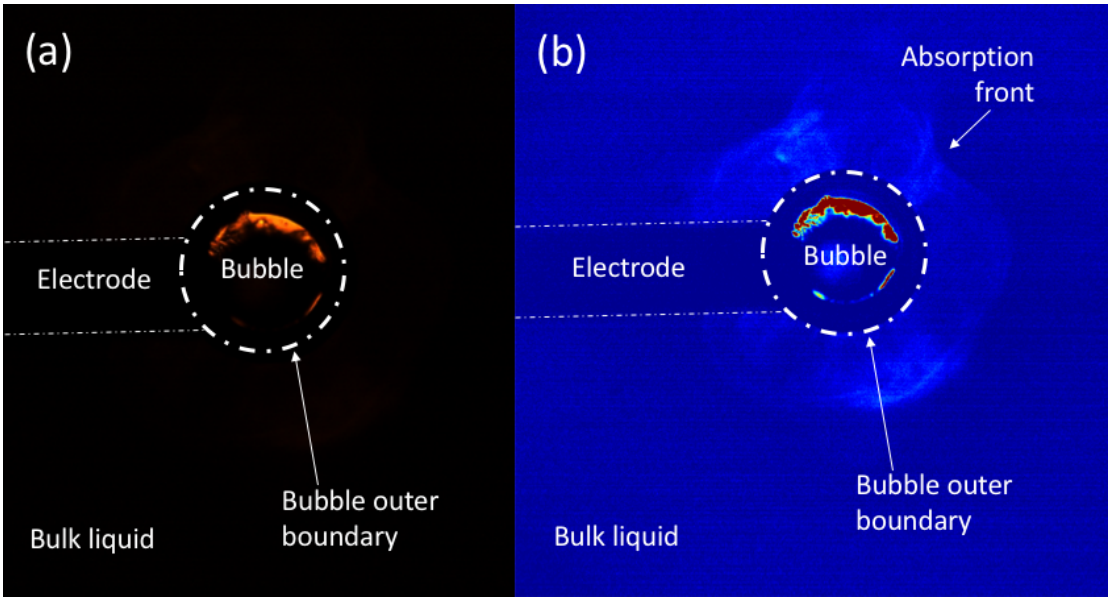

Figure 5.12: Post-processing of spectrophotometry images.

As seen in Fig. 5.13, the region of low indigo trisulfonate extended far into the bulk liquid region after four seconds. Due to the high reaction rate between indigo trisulfonate, ozone and hydroxyl radicals, it is unlikely that these oxidative species diffused far away from the liquid phase. Thus, it is possible that indigo dye was consumed at the interface, and the

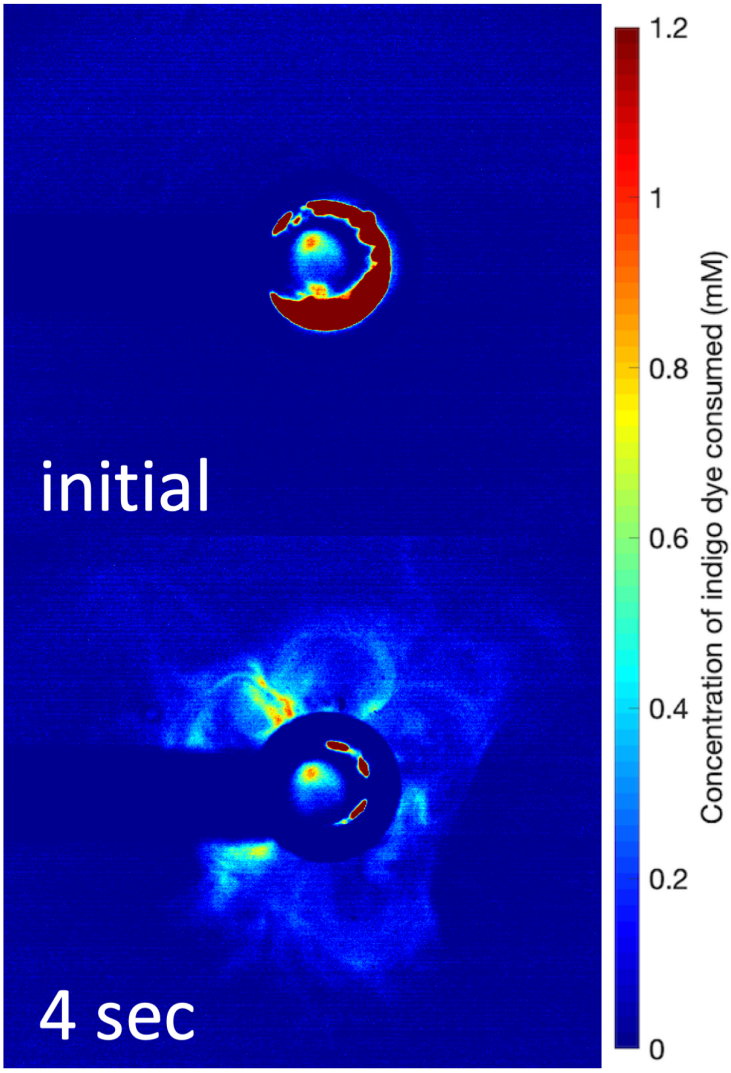

Figure 5.13: Time lapse image of transport of reactive species in bulk liquid.

discolored reaction products were transport into the bulk liquid due to plasma-induced fluid flow. Using the calibration curve obtained, the amount of oxidative species produced and transported through the liquid layer was found to be in the order of several hundreds of micro-mole per liter (μM) after four seconds in the bulk liquid. In regions close to the interface, the concentration reached approximately 1 milli-mole per liter (mM), which corresponds to approximately 48 parts per million (ppm). Regions of low concentration of indigo trisulfonate can be seen in the bulk liquid region, far away from the bubble. This is consistent with the previous result, where plasma-induced fluid flow drove convection flow in the bulk liquid and significantly improved mixing between the interface and bulk liquid significantly. [103, 105] With a high initial concentration of indigo trisulfonate, it is assumed that any oxidative species produced were consumed. Future studies, including the direct measurement of ozone production using absorption spectroscopy and hydroxyl radical production using emission spectroscopy, will better elucidate the contribution between the production of aqueous reactive species at the interface and the transport of gaseous reactive species through the interface.

Chapter 6

Instabilities at the plasma-liquid interface

In this experiment, we utilized particle image velocimetry (PIV) and shadowgraphy to assess changes in the interface as well as determine the plasma-induced flow field directly. The velocity flow field yielded reactive species streamlines as well as provides insight into interfacial stability. What followed were experimental measurement of plasma-induced liquid flows, variations in the density gradient near the interface, and possible instabilities at the plasma-liquid interface in response to two types of plasma generated in the 2-D bubble: 1) localized microdischarges and 2) direct streamer discharge. Microdischarges are dielectric barrier discharges where water acts as a dielectric barrier; these discharges are localized on the surface of the powered electrode, but do not fill the gap between. Streamers bridge the gap between the powered electrode and the interface and are visible as bright filaments. These measurements presented here gave additional insight into the role that plasma de-

rived forces may play in the generation of the large-scale circulation pattern observed in previous work, which may significantly influence the transport of active species and radicals from the interface into the bulk solution [103].

6.1 Experimental set-up

6.1.1 2-D cell

The 2-D discharge cell used in this experiment is schematically described in Section. 3.2 and depicted in Fig. 3.4. The gas used in this work was air, is injected through the powered electrode tube using an industrial grade plastic 1-mL syringe. This hollow tube is connected to a high voltage nanosecond pulsed power supply (FID GmbH, FPG 10-10KM) to excite plasma inside 2-D bubble.

PIV measurements typically require the illumination of the plane of the flow field of interest and the acquisition of the scattered light normal to that illumination plane. In order to carry out this measurement, a modified 2-D bubble cell was used. This cell, fabricated from clear, optical grade plexiglass, featuring a 1 mm deep recessed volume, etched into the plexiglass plate. A powered gas injection electrode along with ground electrodes were located in this recessed region. The recessed region was necessary to avoid o-ring obstruction of the illuminating laser sheet. In this case, the recessed area is below the plane of the sealing o-ring. Fig. 6.1 illustrates schematically the PIV 2-D bubble cell and experimental set up.

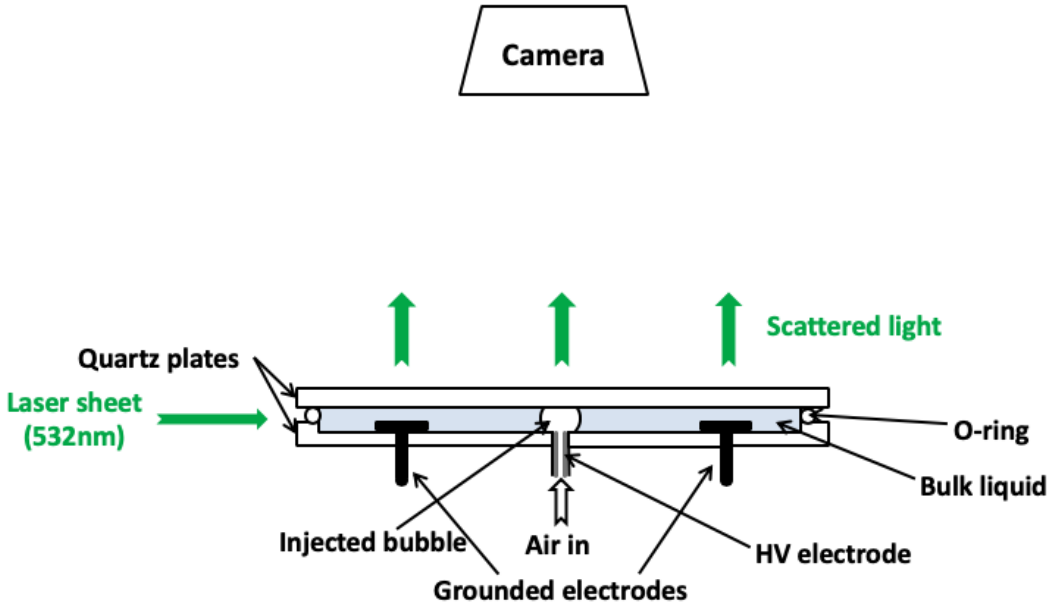

Figure 6.1: PIV experimental set-up.

6.1.2 Shadowgraphy

Shadowgraphs were formed by using two concave mirrors of diameter of 75 mm and focal length of 750 mm. The light source used was a 150 W fiber optic halogen light illuminator. The image was focused using a convex lens of diameter of 15 cm. An iris was used to terminate deflected rays, giving rise to greater contrast. The projected image was collected on a screen and photographed with a digital camera. The experimental set up is shown in Fig. 6.2.

High speed imaging of the shadowgraph images and colorimetric reactions in the 2D test

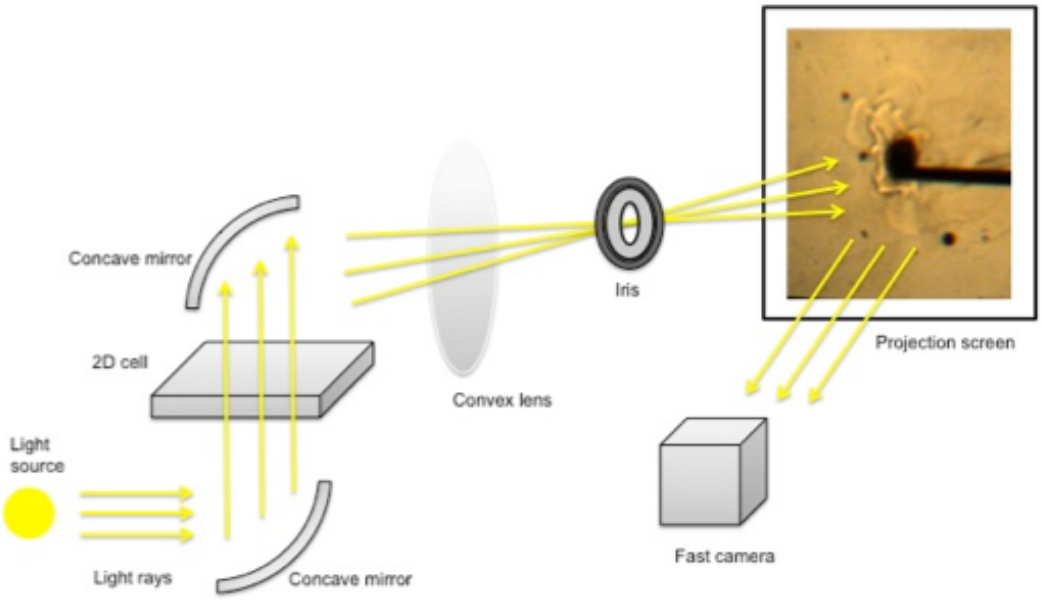

Figure 6.2: Shadowgraph schematics.

cell were acquired using Photron FastCam UX100. Frame rates used in this work extended from 50 fps to 1000 fps. Resolution of the image is of 1280 pixels by 1024 pixels, where the field of view is approximately 15.5 cm by 12.4 cm.

6.1.3 Particle image velocimetry (PIV)

A schematic representation of the PIV setup is also shown in Fig. 6.1. A Nd:YAG sheet laser, with frequency doubled to produce light at 532nm, is used to illuminate fluid external to the bubble, and was operated at a power of 1W at a repetition rate of 100 Hz. Neutral buoyant microbeads of 10 micrometer diameter were added to the liquid water captured in

the 2-D cell to assess the flow field. Measurements were taken while streamers were present in the 2D bubble. The scattered laser light from the moving particles was measured using a fast camera Vision Research Phantom M340 with a resolution of 2560 pixels by 1600 pixels and a frame rate of 100fps. Software Davis 8.2.2 [106] was used to convert images to a flow field map.

6.2 Experimental results and analysis

6.2.1 Velocity flow field

Fig. 6.3 depicts a typical flow field profile observed when a streamer contacts the interface. As indicated in the figure, the air bubble is located at the center of the image. The dark area above the bubble is located in the bubble's shadow, where poor illumination of tracer renders no available flow field data. The fluid is set into motion driven by the streamer-interface interaction, this was observed in previous studies where precipitates were observed to circulate in the bulk liquid, with fluid flow initiated at the interface [103]. Significant velocity shear is apparent at the interface. A sharp velocity gradient is observed between the dashed bubble boundary and high speed region. This suggests that the fluid velocity very close to the bubble boundary greatly exceeds flow speeds in the bulk liquid, reaching to speeds up to 1.5 mm/s, as shown in Fig. 6.3. Such speeds are comparable to previous experimental results.

A very sharp velocity gradient can be observed between the high-speed region, shown in red, and the boundary of the air bubble. Using ImageJ image processing software, it was found that a velocity shear gradient occurs within a layer of thickness approximately 1.5 mm measured from the boundary of the bubble. The flow field does not vary greatly in other regions surrounding the bubble, shown as light blue regions in Fig. 6.3, possibly due to the lack of streamers contact in those regions. The streamer is apparently the source of the large-scale circulation observed.

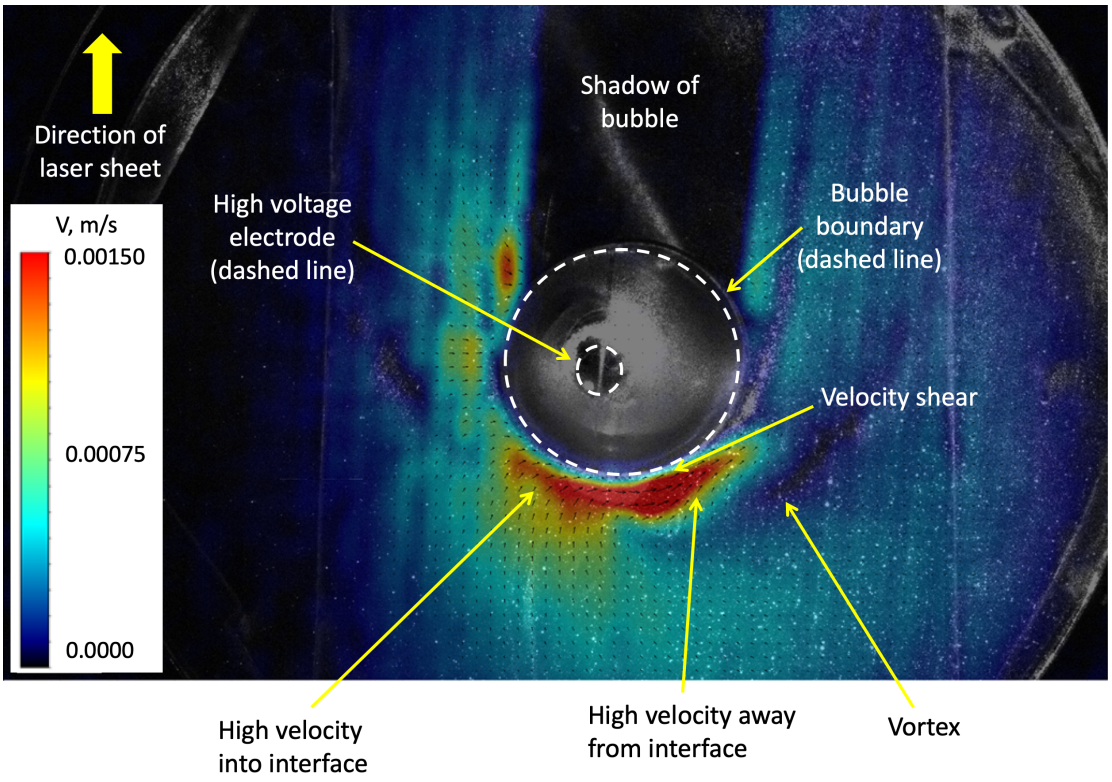

Figure 6.3: PIV fluid flow field showing sharp velocity shear at the interface.

To the right of the red high-speed region, a dark blue low speed region can be observed,

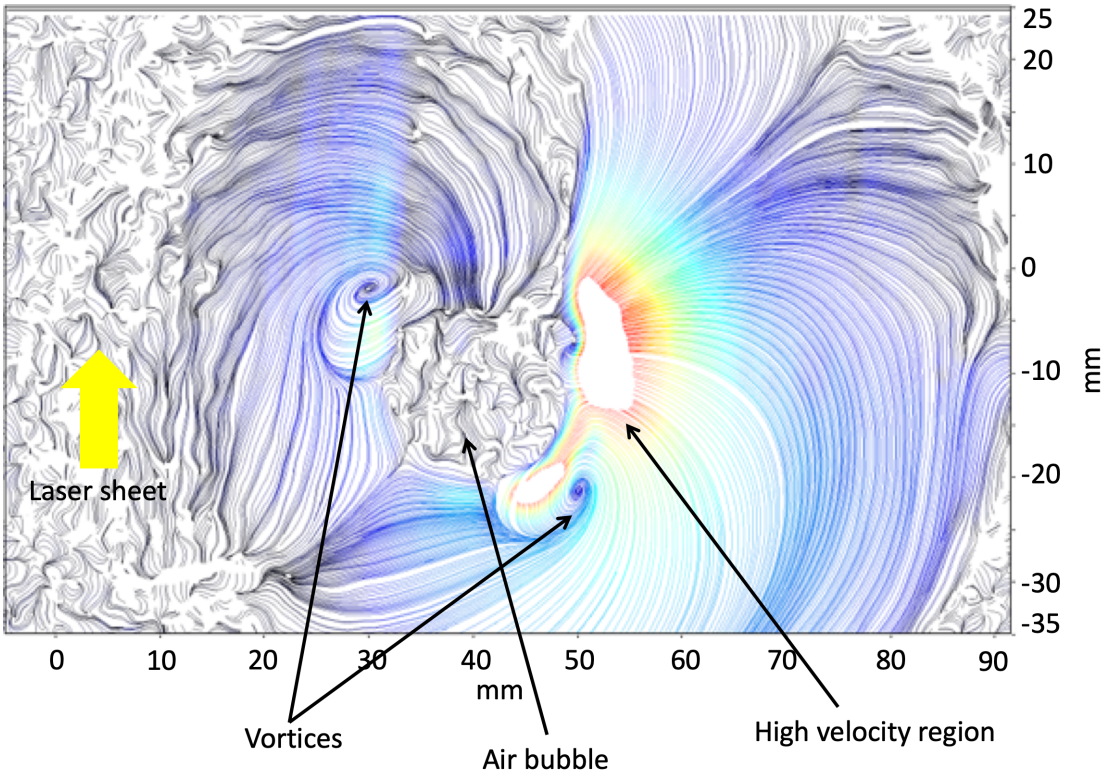

Figure 6.4: PIV fluid flow field showing the presence of vortices.

as noted on Fig. 6.3. The varying directions of the low velocity flow field surrounding the region show that the region is a vortex. These circulation patterns can enhance radial transfer into the bulk liquid. The formation of vortices is also evident in Fig. 6.4. While these vortices can be seen as sources and sinks of streamlines, the flow is not 3D. Broken streamlines are found in the bubble shadow and on the left side of the bulk fluid where tracers experienced little to no motion. No correlation associated with tracers moving out of thin laser plane due to 3D flow was observed during post-processing, thus the flow observed is essentially 2D. Streamers come into contact with the interface on the right side of the bub-

ble, initiating high flow speed in the fluid, shown as the white region in the figure. Vortices are formed in the bulk liquid near the interface as a result of streamer-driven flow. The presence of the circumferential flow at the bubble interface and vortex patterns is reminiscent of Marangoni flows. Marangoni flows are driven by gradients in the surface tension. The localized nature of the streamer attachment at the interface can drive such flows through localized heating, high electric field strength and sharp concentration gradient, all of which could lead to a significant gradient in the surface tension.

Interestingly, in a similar experiment, Marangoni flows of geometry similar to that observed here was initiated on a bubble trapped between two slides by localized heating at the bubble liquid interface using a laser pulse [107]. The similarities between the observed flow in this experiment and this present work provide anecdotal evidence that the circulation patterns and vortices observed is driven by Marangoni effects. It is interesting to note that this circulation has been observed in DC glows with liquid anode and in plasma jets incident on liquid water. In common with all of these systems is the very localized plasma attachment, each of which can drive Marangoni convection. It is entirely possible that the bulk flows in each of these systems are due to Marangoni effects. Future work will involve solving the Marangoni convection equation with localized heat or concentration gradients consistent with streamers to further investigate the connection between the observed flows and the Marangoni effect.

In addition to the large-scale circulation patterns, observed were discrete structured radial flows towards the interface, shown as white crown-like structure surrounding the bubble, in Fig. 6.5. These flows may be consequences of self-consistent action of multiple vortices formed at the interface initiated by streamer action, pulling bulk liquid towards the interface, such behavior is also consistent with Marangoni flow.

Additionally, as shown in Fig. 6.6, are interfacial oscillations driven by streamer action. Oscillations are known as capillary waves and have been observed in past experiments [67]. The propagation of such waves can alter local density at the interface as well as modify the local electric field there.

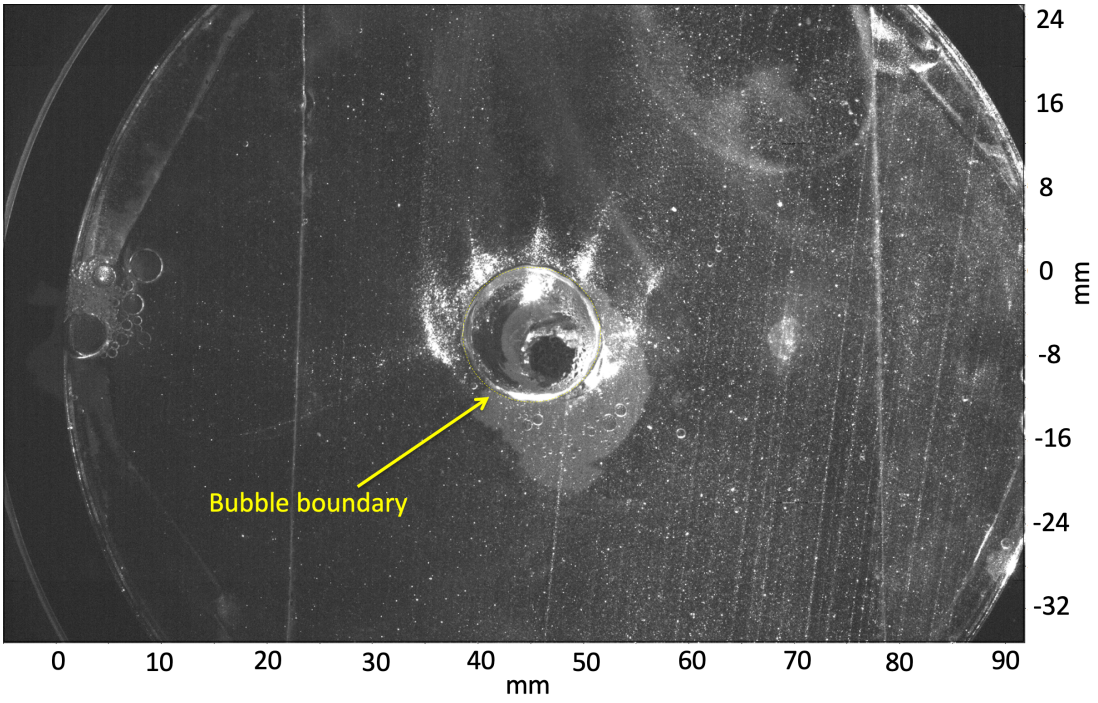

Figure 6.5: PIV scattered light measurement.

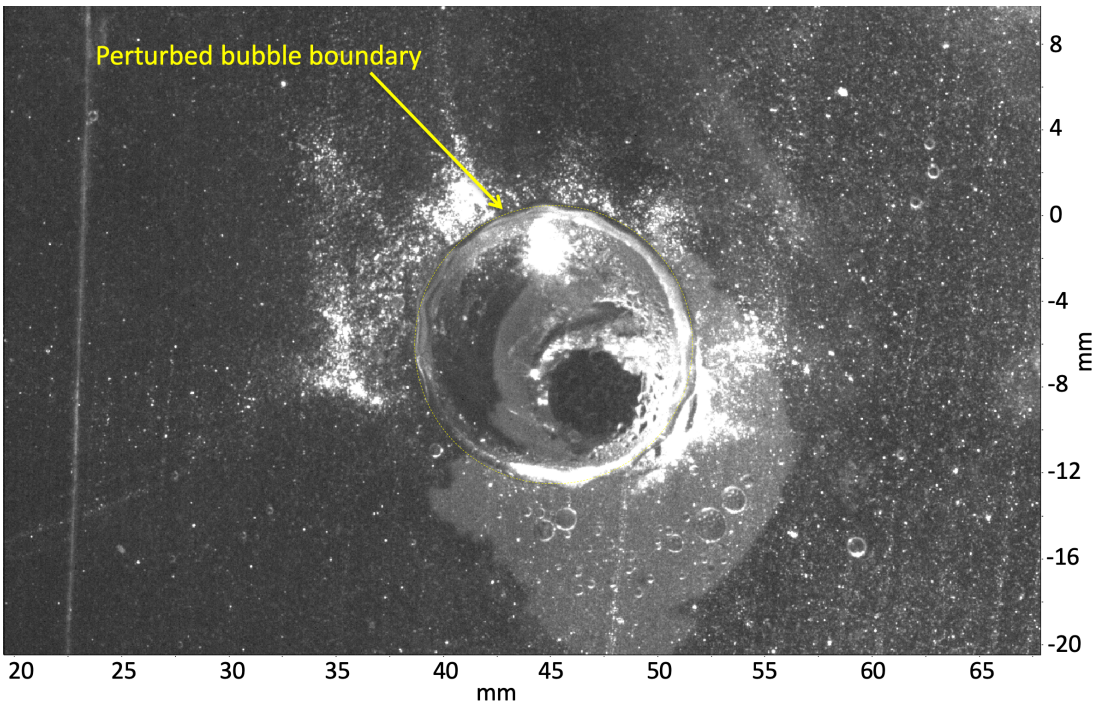

Figure 6.6: Close up of PIV scattered light measurement.

6.2.2 High speed imaging of colorimetric reactions in liquid

Previously, a potassium iodide and starch solution was used to study reactive oxygen species production including reactants such as hydrogen peroxide in the 2D test cell [103, 108]. Hydroxyl radicals formed in the plasma can combine to form hydrogen peroxide at the interface, which subsequently oxidizes iodide ions in the water into iodine. Iodine is trapped in starch molecules and forms a complex that appears blue in the bulk liquid. In this work, we investigate the relationship between plasma-induced perturbation of the interface and the transport of ROS. Interfacial perturbations affect not only convective transport by initi-

ating fluid flow but also enhanced diffusive mass transport via presence of capillary waves [67]. Bubble interface deformations were observed and imaged at 500 fps.

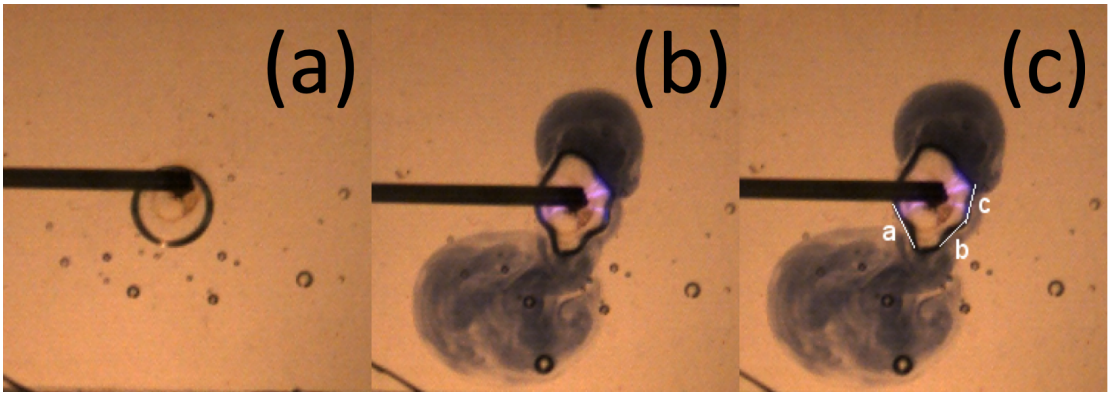

Figure 6.7: (a) Without plasma (b) Bubble deformation due to presence of plasma (c) With wavelengths labeled

Fig. 6.7 depicts bubble variation due to streamer action; compared with a circular bubble boundary at the absence of plasma, shown in Fig. 6.7a, the bubble boundary deformation is clearly visible in Fig. 6.7b. The induced capillary waves along the interface are driven by both streamer action and surface tension. Using ImageJ, the wavelengths of the observed capillary waves were labeled as a, b and c, shown in Fig. 6.7c; and were measured to be 3.101 mm, 2.405 mm and 2.603 mm respectively, with an average value of 2.703 mm for use in later dimensional analysis. The wavelength variation is likely due to the asymmetry of the radial location of streamers. While the streamers intensity and location of contact varies in time, the bubble boundary deformation is active and changes in time. Thus the wavelengths of observed deformation modes vary but remain within the same order of magnitude; shorter wavelengths are measured in regions where larger number of streamers was

observed.

Asymmetrical pattern in bulk liquid region of potassium iodide and starch solution, shown as blue colored region in Fig. 6.7, was observed to originate from contact points of the streamers. This observation suggests that indeed streamer interface interaction is a key source of ROS and RNS, which leads to asymmetric injection of reactive species and corresponding swirl like flow in bulk liquid.

Streamers in contact with the boundary appear to push the boundary outward, causing subsequent deformations and interfacial capillary waves. The origin of this deformation is not well understood; though localized heating, surface tension effects and polarization may play important roles. It is well known that liquid droplets distort under electrohydraulic forces in a non-uniform electric field [66]. Studies have shown that electric field at streamer head can reach up to several hundred kV/cm upon contact at interface [109, 110]. The electric field pressure exerted on the interface by the streamer at the contact point can approach local water pressure and thus excite the interface. Electric Weber number, as the ratio of deforming electric field pressure to surface tension, is calculated to find out whether fluid motion is a result of electric perturbation [111, 112]. Using electric field of 120 kV/cm found in this study by Bonaventura et al [110] and the average capillary wave wavelengths of 2.703 mm, the electric weber is calculated to be 47.3, which shows that electric field pressure is a driving force in perturbing the interface. It is also possible that charge deposited

on the interface may be responding to the streamer electric field giving rise to outward repulsion. This latter mechanism is possible as it is known that solvated electron lifetime is about 1 μs [35]. In this span, during a pulse, many nanosecond wide streamer pulses could interact with localized charge thus providing a potential mechanism for the observed effects. Electrostriction, in which the interface is actually pulled in the direction of the electric field gradient, could also give rise to interface perturbations [113].

6.2.3 Analysis of shadowgraphs

Shadowgraphy can be used to infer density gradients and the presence of turbulence in solution associated with local plasma action on the interface. Turbulence can drive mixing and thus may play an important role in radical transport from the bubble into the solution. A shadowgraph observed in this work is shown in Fig. 6.8, taken at 50 frames per second. In this case, the streamer is excited at 4 kHz with peak voltage at approximately 2 kV. Bulk liquid used is tap water.

As labeled, the bubble is located at the center of the image. It appears dark since light refracts away at the quartz-air interface in much more than at the quartz-water interface. Surrounding the bubble, areas of various darkness and brightness are observed. As index of refraction scales positively with density, density gradient in water produces a gradient in the index of refraction, which leads to deflection of light rays. Brighter region results from less deflection and represents regions of lower density, where darker region represents region of

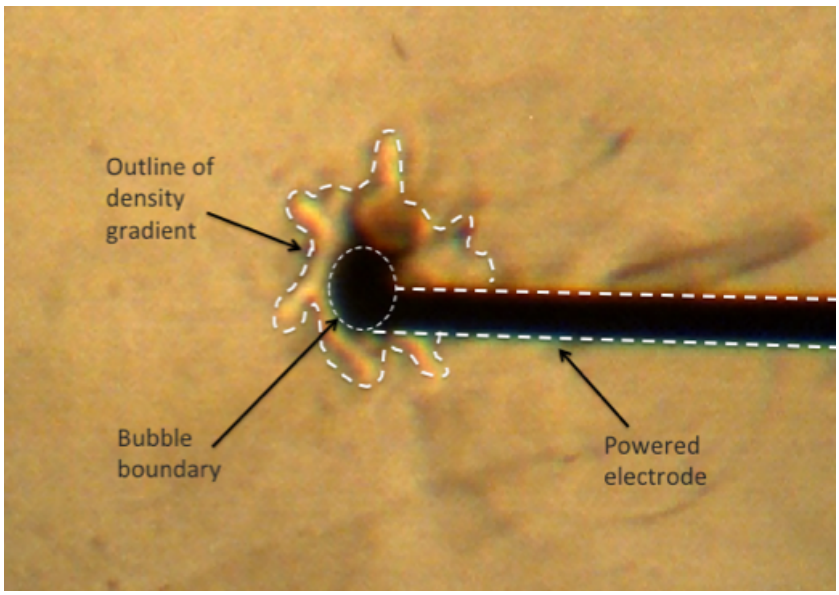

Figure 6.8: Shadowgraph image

higher density.

As light rays tend to deflect away from area of higher density, brighter region represents that of lower density; where darker region represents that of higher density.

It was observed that the density gradients around the bubble are highly structured as observed in the figure. It is speculated that streamers impart an outward force on the interface, leading to local compression as observed as the darkened band marked in dash line surrounding the lower density region.

The shadowgraph image observed was active, where the density gradient shifts in time with a pumping-like motion. This pumping might explain the behavior of particle flows in the PIV images. It should be pointed out that these fluid dynamical effects are likely not re-

sponding to a single nanosecond voltage pulse but rather a train of them acting in series and ultimately resonantly to drive this observed macroscopic response. Shadowgraph images were used to assess interfacial stability as discussed in the next section.

6.2.4 Stability analysis

It is known that in the presence of velocity shear, small perturbations at the boundary between two fluids can grow, giving rise to the Kelvin-Helmholtz (KH) instability. Such instability is well studied in magnetohydrodynamics (MHD) [114]. The velocity shear observed in Fig. 6.3 is a result of both surface tension force maintaining the bubble shape and the fluid flow initiated by the streamer head, such sharp shear is of the magnitude necessary for the conditions of the instability if there is perturbation of the plasma-liquid boundary.

As noted in the analysis by Miura and Pritchett [114], instability growth rate increases linearly with wave number, whereas at short wave number, the modes satisfying $k\Delta < 2$ are unstable, where k is the wave number and Δ is the length scale of shear. Additionally, most unstable modes has $k\Delta \quad 1$. The wave number k is calculated as $2\pi/\lambda$, and λ is defined by one wavelength of the perturbation observed at the velocity shear interface. The velocity shear interface is infinitesimally short distance away from the bubble interface, thus λ is assumed to be of similar value to that of vibration wavelengths observed in Fig. 6.3. The shear length scale Δ is 1.5 mm as inferred in Fig. 6.3. Average capillary wavelength is taken to be 2.703mm (Fig. 6.7). With these approximate values, $k\Delta$ is calculated to be 3.5, thus the

velocity shear regions are stable.

Stable boundary can still generate vortices as the shearing layers folds towards the boundary. Such vortices are desirable in plasma applications in various fluid systems as they lead to increased mixing and convection flow in fluids, thus allows the active species created in plasma to further transport into the bulk liquid in addition to diffusion alone. These vortices are clearly observable in Fig. 6.9.

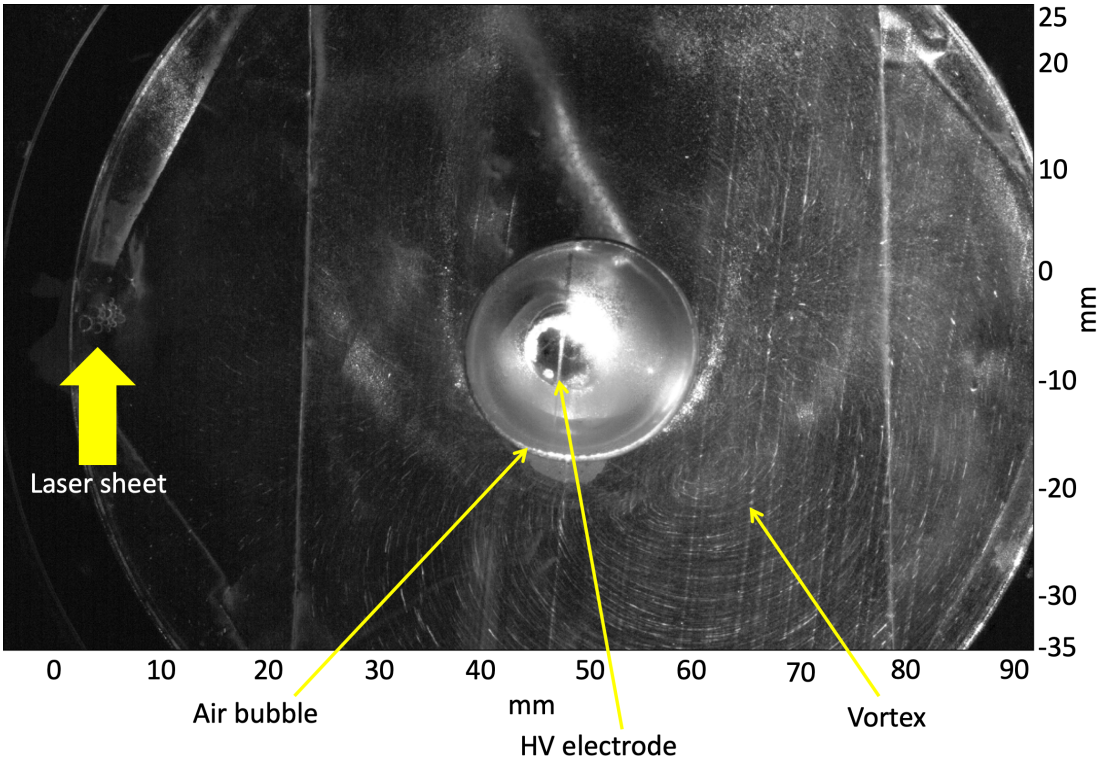

Figure 6.9: PIV flow field.

Chapter 7

Capillary waves on the interface

Chapter. 4 and 5 describe complex chemical processes at the plasma-liquid interface that lead to formation of reactive oxygen and nitrogen species, as well as reducing agents such as solvated electrons. This induced chemistry activates the water, thereby enabling the specific technological function such as decomposition or enhanced healing. Interestingly, the mechanical interaction between plasmas and the interface is not understood. Plasma formation is associated with production of excited species, energetic charged particles, photons and high fields. This energy can interact with the interface mechanically and lead to driven oscillations, which in turn can lead to forced diffusion in liquids [115, 105]. From a more fundamental fluid mechanics standpoint, streamer excitation of capillary waves at the interface is a novel method to probe viscosity and elastic properties of the gas-liquid interfaces as well [116].

In this experiment, we study the production of capillary waves that propagate along the liquid interface boundary which is excited by a pulsed atmospheric pressure discharge. Past work has shown that streamers in contact with the interface of bubbles can give rise to two different macroscopic oscillation modes: 1) volume conserving shape mode in which the exterior of the bubble morphs into various shape with spherical harmonics solutions, and 2) volume mode in which the bubble volume oscillates [68, 115]. These effects can alter internal pressure and electric field distribution in the bubble. Additionally, localized streamer perturbations can displace the elastic interface giving rise to propagating capillary waves - simple elastic oscillations propagating along the interface [115]. Two key questions remain unanswered: how does induced boundary perturbation arise? And how does this perturbation affect subsequent streamer formation and discharge propagation? This effort aims to address these questions by elucidating the forces imparted to the interface by streamers and the nature of the feedback from the mechanical change on the interface.

We report here the observation of surface capillary waves formation in response to nanosecond pulsed streamer discharges in 2-D bubble and the subsequent plasma self-organization. Streamer discharges inside the 2-D bubble perturb the interface, launching capillary waves on the surface. The amplitude of the oscillation is a measure of the stored potential energy at the interface and is thus a measure of the pressure forces present at the streamer head. The capillary wave modes are functions of plasma pulse frequency and the bubble diameter.

Correlation between theoretical capillary waves at air-water interface and experimental data shows that the capillary waves are likely driven by plasma and restored by surface tension only. Capillary waves can also be initiated along the surface of adjacent bubbles, possibly due to streamers initiated inside, or transmitted capillary wave-derived acoustic oscillations in bulk liquid. Additionally, subsequent streamers excited appear to self-organize due to surface perturbation. This indicates an important positive feedback mechanism observed between discharge-induced surface perturbation and spatial self-organization of subsequent streamer strikes. This work thus illustrates the interplay between plasma dynamical effects and fluid dynamical effects. Understanding this interplay effect gives insight into how streamers can alter the contact area between plasma and liquid surface, particularly during the self-organization process. This can be relevant for various plasma applications. Efficient water purification relies on maximizing the plasma-water treatment surface area [117]; and adaptive plasma devices for treatment of cancer can be thus tailored with better understanding on plasma self-organization in bubbles [118].

7.1 Methods

The 2-D discharge cell used in this study is shown in Fig. 3.5 and described in Section. 3.2. A nanosecond pulse generator (Eagle Habor Technologies) was used to excite plasma inside the 2-D bubble. The central electrode was excited at a voltage of 20 kV with pulsing

frequency ranging from 100 to up to 2 kHz, and pulse width ranging from 20 to 260 ns. Voltage and current waveforms of a typical 20 kV, 120 ns pulse across the 2-D discharge cell are shown in Fig. 7.1. Feed gas used is ambient air, injected using a 1-mL industrial syringe.

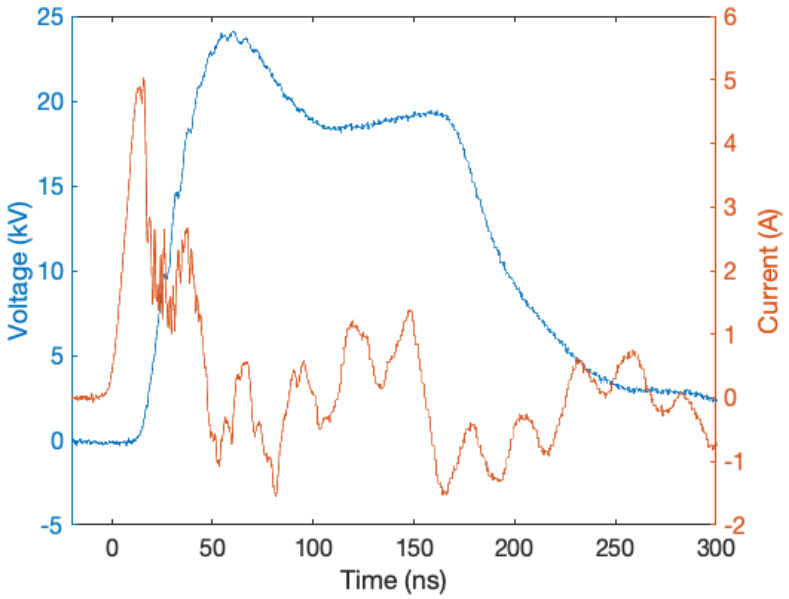

Figure 7.1: Voltage and current waveforms of a typical 20 kV, 120 ns pulse.

Chemical dye potassium indigotrisulfonate was used to highlight the bubble cavity region by giving a distinct contrast between the gas and liquid region. The dye has high absorbance of 600 nm light [95]. By placing a 600 nm (10 nm FWHM) filter between the discharge cell and imaging camera, the background liquid appears dark. The set up gives high contrast between the gas region and the liquid at the interface, and enhances the imaging of any interfacial oscillations. A fast camera, Photron FastCam UX100, is used to image at high frame rates; frame rates used in this work extended from 80 to 8000 fps. A Nikon

60 mm f/2.8D DSLR camera lens was used in combination with the camera.

Particularly, it is interesting to note that, the surface of the bubble remains curved and appears on image, even when the trapped liquid layer is thin. Described schematically in Fig. 7.2, the curvature of the surface refracts light away and appears dark, while light passing through the bubble and liquid region remains unperturbed. This effect is illustrated in Fig. 7.3. When backlight intensity is increased in the absence of the optical filter, not all the incident light is absorbed by the dissolved dye, which gives the liquid region a purple hue. With the light passing through bubble region unperturbed but blocked by the curved surface, the boundary is seen as the dark layer separating the bubble and liquid region.

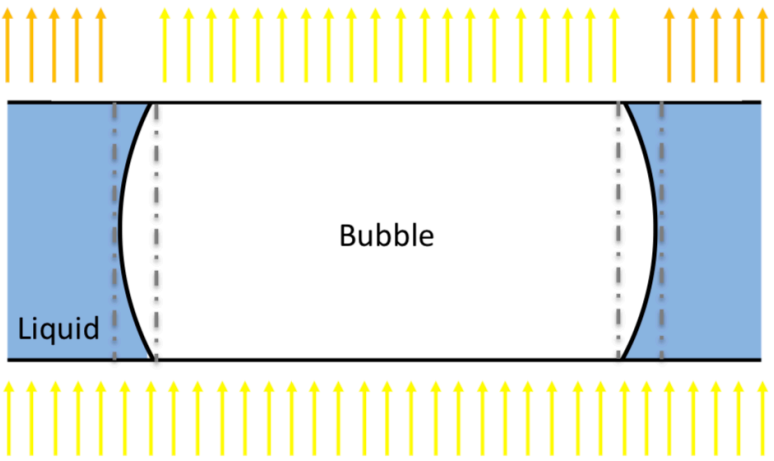

Figure 7.2: Cross section of 2-D cell, side view of bubble and surrounding liquid region. Light passes through bubble and liquid region unperturbed but is blocked by the curved surface.

Additionally, part of the high voltage electrode, embedded in the top quartz plate, obscured the bubble region. This can be seen in Fig. 3.5, where the electrode covers the right

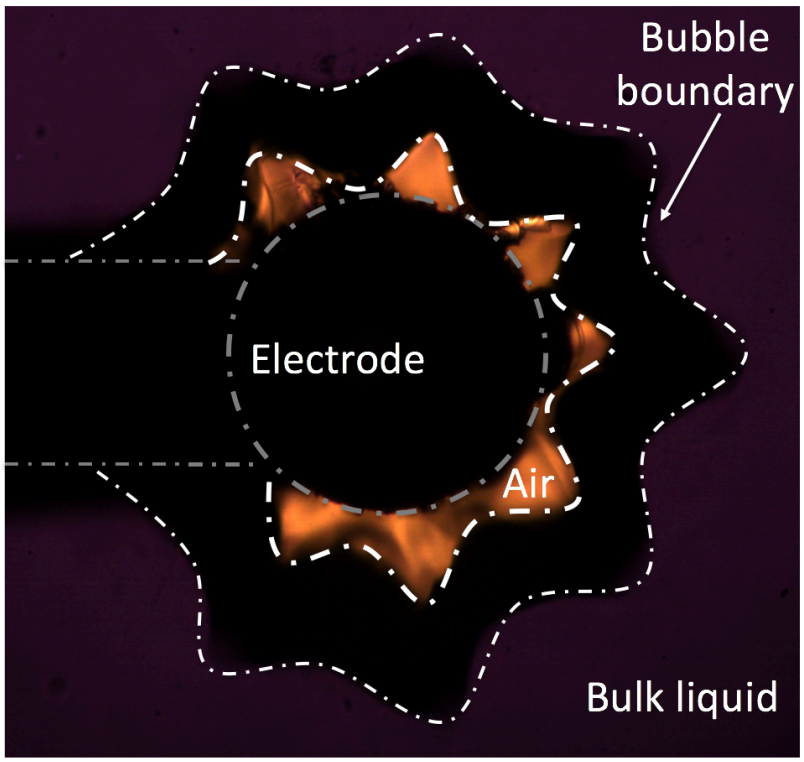

Figure 7.3: Plasma-induced bubble boundary perturbation.

side of the bubble, and in Fig.7.3, where the electrode is outlined in gray dashed line.

7.2 Spatiotemporal evolution of deformation of bubble boundary

Observed spatial and temporal variations of the bubble boundary under the influence of a repetitively pulsed discharge is depicted in Fig. 7.4. Here, the discharge in bubble were excited with 20 kV, 20 ns wide pulses at a repetition rate of 1 kHz. The discharge cell was backlit with a white light source and imaged through a 600 nm filter. This gives high contrast between the liquid and bubble region, where the bubble region appears bright orange

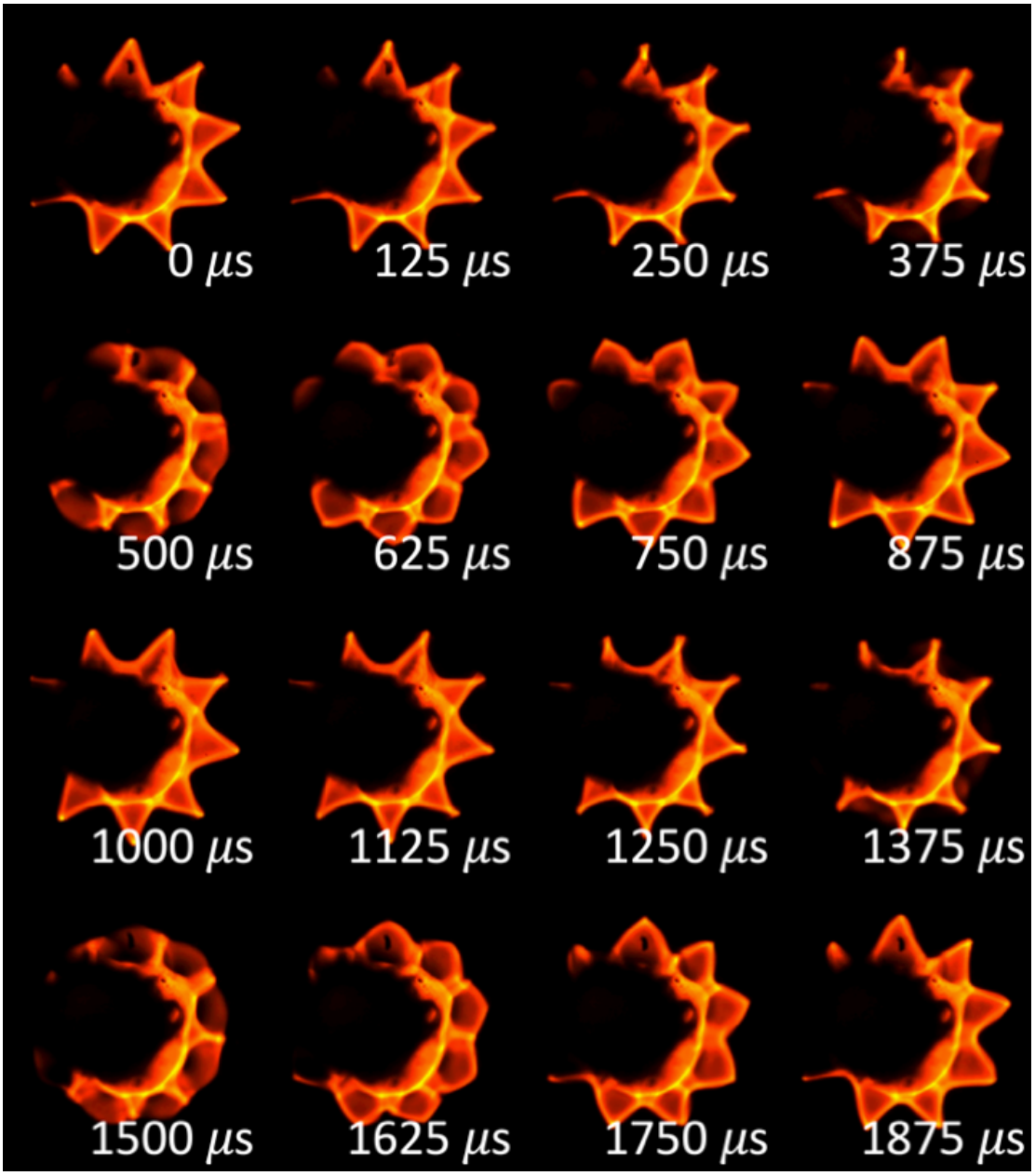

Figure 7.4: Spatiotemporal evolution of air cavity.

and liquid region appears dark. Images were captured at 8000 fps, which gives 125 μs resolution between frames.

The oscillation pattern can be seen as a 9-pointed star in both Fig. 7.3 and 7.4. Given that the surface perturbation resembles the shape of star polygons, we have adapted the language often used in mathematics to describe these shapes. In this case, a 9-pointed star polygon will be identified as an n = 9 mode.

For the 1 kHz excitation frequency, images of the discharge were acquired in temporal intervals of 125 μs, yielding 8 images between each pulse. This allows for resolution of temporal evolution of surface perturbation in details. As shown in Fig. 7.4, peaks turn into troughs and then peaks again in approximately 2000 μs, that is, peaks at 0 μs turn into troughs at 1000 μs, and grow into peaks again at 2000 μs. This gives a surface perturbation oscillation rate of 500 Hz, one half of the excitation frequency. This is consistent with Faraday's observation in his investigation of standing waves on surface of liquid placed in a vibrating container. He observed that the frequency of the observed wave was half of the external vibration frequency, suggesting that the surface oscillations are also standing waves [119, 120].

The source driving the perturbation and development of capillary waves is postulated to be combination of effects such as electric field pressure and localized modification of interfacial surface tension due to chemical or temperature gradients [66]. The high electric

field at the streamer head can generate high electric pressure. Our calculation shows that this results in an electric Weber number, ratio of electric field pressure to interfacial surface tension, of order 1. The electric pressure can therefore perturb the interface. If electric Weber number is much larger than 1, electrical forces would burst the bubble; if electric Weber number is much smaller than 1, there would be insufficient electrical forces to perturb the surface. In addition to electric pressure due to high electric field, electrons and ions in streamers impacting the boundary can also transfer momentum to water molecules at the interface and perturb the surface.

In general, for low viscosity ideal fluid, the angular frequency of capillary wave at the interface can be calculated as:

$$\omega_0 = \sqrt{\frac{\sigma k^3}{\tilde{\rho}}} \tag{7.1}$$

where $\tilde{\rho}$ is the sum of the densities of water and air, σ is the interfacial surface tension and k is the associated wave number. For an observed oscillation frequency of 500 Hz, the wavelength resulting from Eq. 7.1 is roughly 1.2 mm. In order to compare this value with that observed on the perturbed bubble surface, we estimate the observed wavelength as the quotient of the arc of a circle drawn between peaks and troughs by the n mode, in this case n = 9. Thus we estimated that the wavelength of the observed capillary waves is approximately 1.1 mm, which matches well with our calculated value, indicating that the capillary wave is dominated by surface tension.

Radii of peaks and troughs in Fig. 7.3 have an average difference of 0.48 mm. This gives a capillary wave amplitude of 0.24 mm, approximately 10% of the bubble radius. This amplitude is a measure of pressure forces present at the plasma streamer head. By resolving the effects of viscosity, surface tension, and densities of fluids, the pressure acted on the interface by plasma streamers can in principle be estimated.

Laplace's equation gives the pressure difference across the water-air interface due to surface tension,

$$\Delta P = \sigma(\frac{1}{R_1} + \frac{1}{R_2}) \tag{7.2}$$

where ΔP is the pressure difference across the interface, σ is the surface tension, and R_1 and R_2 are the principle radii of the curvature. In our case, we assume that the capillary wave is essentially contained in a 2-D plane. Thus we can assume that one of the principle radii is sufficiently large where Laplace's equation simplifies to

$$\Delta P = \frac{\sigma}{R} \tag{7.3}$$

The radius of curvature of the capillary wave can be estimated for sinusoidal waves with infinitesimal amplitudes, according to Kenyon [121]. With the capillary wave amplitude of 0.24 mm and wavelength of 1.2 mm, the height of capillary wave (y) can be expressed as a

function of location on the circumference (x) in the form of

$$y = a\, sin(kx) \tag{7.4}$$

where $a = 0.24$ mm is the height of the wave amplitude, and k is related to the wavelength where $\frac{2\pi}{k} = 1.2$ mm. The radius of curvature is thus

$$R = \frac{1}{k^2 a} \tag{7.5}$$

In our case, R is calculated to be 0.152 mm. Thus we can estimate the pressure acted on the surface by plasma streamers as the pressure difference ΔP, which is calculated to be 479 Pa. The pressure exerted by an electric field can be estimated as $\frac{\varepsilon_0 E^2}{2}$, where ε_0 is the permittivity of free space, and E is the magnitude of electric field at the streamer head, which can reach up to several hundred kV/cm upon contact. [109, 110]. The pressure exerted by an electric field with a magnitude of 100 kV is thus calculated to be 443 Pa. The calculated pressures are of the same order of magnitude, which suggests that the capillary wave is likely driven by electric pressure exerted on the interface by the streamers.

Also, spatial variations in the light intensity can be seen in the images. This is possibly due to internal reflection of light at sharp points and other non-uniformities of the surface perturbation. However, these two observations are not further investigated in this particu-

lar study.

The excitation of capillary waves on the interface increases the contact area between plasma and the surrounding water, thus also increases the loss area of plasma-derived reactive species into the liquid. For the observed capillary wave with wavelength of 1.2 mm and amplitude of 0.24 mm, the calculated arc length for one period is 1.6 mm, which gives an estimated radio of perturbed boundary length to the circumference of the bubble of 1.3. Plasma-derived reactive species can be produced in-situ at the plasma-liquid interface or diffuse across the interface into the bulk liquid. Thus the optimization of plasma-liquid contact area can lead to increase transfer of plasma's reactivity into the bulk liquid, and is important for many plasma liquid technologies.

7.3 Formation and development of capillary wave

Nyquist sampling frequency is the minimum sampling rate required to reduce error, and is often chosen to be twice the characteristic frequency associated with the experiment, e.g. the pulse frequency. In our case, to measure the transition between excitation pulses, we chose to measure at four times the excitation frequency in order to see how capillary wave develops and propagates. However, at high imaging frequency, the exposure time reduces significantly. Faint emissions from streamers are not detectable by the fast camera at high frame rates. In order to image both streamer discharges and subsequent capillary waves, we

chose a lower pulsing frequency of 200 Hz in combination with a camera frame rate of 800 fps. In this case, the excitation pulse is 20 kV, with a pulse width of 60 ns.

First streamer excitation is shown in Fig. 7.5. Prior to the streamer contact at the sur-

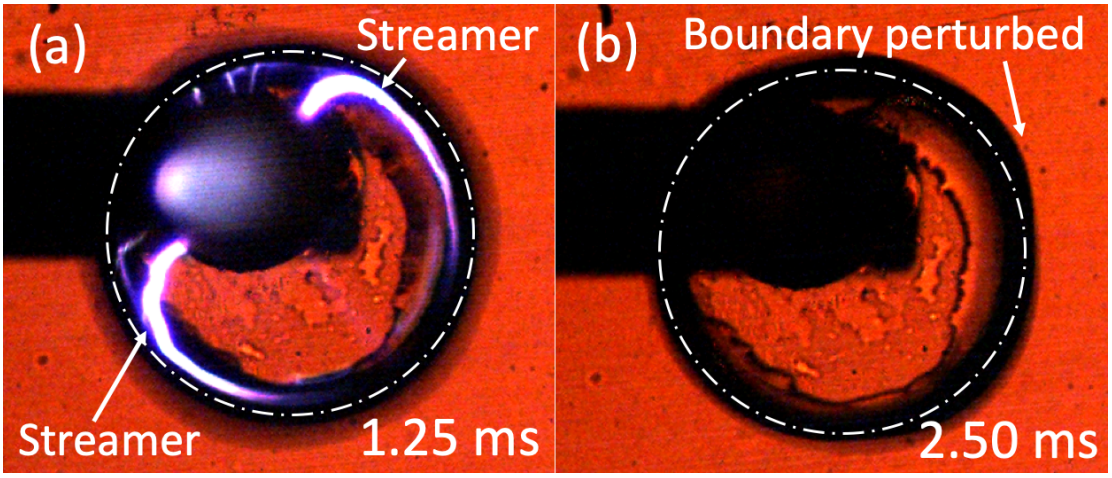

Figure 7.5: Perturbation of bubble boundary from first pulse.

face, the boundary of the bubble is circular without any observable bumps. In Fig. 7.5a, the streamers reach for the bubble boundary and propagate along the boundary. The impact of the streamer at the boundary leaves the boundary slightly perturbed, as seen in Fig. 7.5b. This distortion continues to grow with subsequent pulses, and eventually develops into a capillary wave after 11 pulses. This progression is shown in Fig. 7.6.

The development of capillary wave is likely due to streamers resonantly adding energy to the surface, at the rate of the pulse frequency. However, the perturbation does not grow indefinitely, which suggests that a damping process is present to stabilize the perturbation. Elastic media such as water typically manifests linear force-like responses, where the restor-

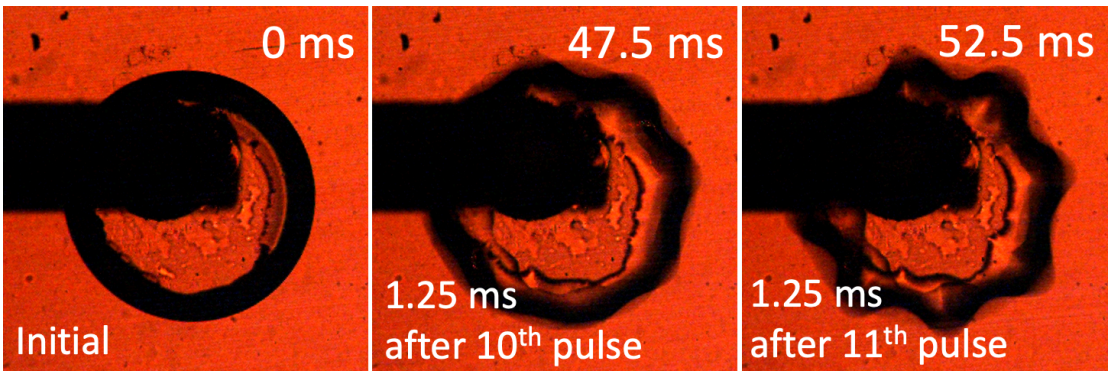

Figure 7.6: Development of capillary waves in time.

ing force is parallel and proportional to the perturbation. In this case, surface tension and finite viscosity likely stabilize the growth of the perturbation. [122] The viscocapillary characteristic time scale is

$$t_{vs} = \frac{\tilde{\mu}^3}{\sigma^2 \tilde{\rho}} \tag{7.6}$$

where $\tilde{\mu}$ is the sum of dynamic viscosities of air and water, σ is interfacial surface tension, and $\tilde{\rho}$ is sum of densities of air and water [122]. In this case, the calculated viscocapillary characteristic time scale is 0.14 ns. With a short characteristic time scale, restoring forces act very quickly. Given that the capillary wave requires approximately 10 pulses to develop, it suggests that the development of the capillary waves is heavily damped and driven forcibly by the pulsed plasma.

First excitation of capillary waves were observed to relax into steady-state dominant mode driven primarily by plasma pulsing frequency. This dependence on pulse frequency will be discussed in the next section. However, this relaxation indicates the possible pres-

ence of a range of harmonic and subharmonic resonances. In the case shown in Fig. 7.6, resonant mode (n = 8) first developed. Capillary waves then relaxed into a subharmonic resonant mode (n = 5) after around 600 pulses, and eventually reached steady-state dominant mode (n = 3) after an additional 1,000 pulses,shown in Fig. 7.7. The evolution from resonant modes into dominant modes is mostly likely related to the damping of resonant modes, and can be calculated by analyzing the frequency dispersion but is beyond the scope of this report [122]. We also speculate that with the frequent occurrences of both singly and multi-branched streamers, multiple attachment points can force higher order modes. Over time, the dominant mode which is not heavily damped remains.

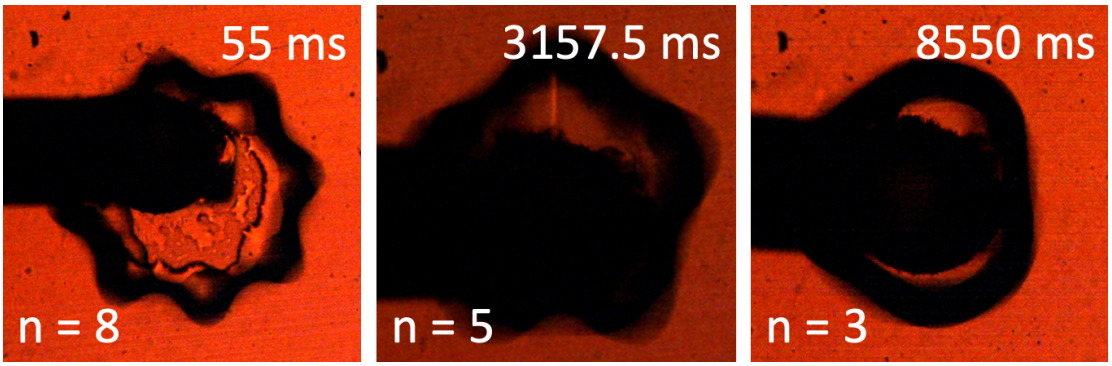

Figure 7.7: Relaxation into dominant mode.

7.4 Effects of plasma pulsing frequency on associated capillary wave modes

Similar to ripples excited on water surfaces, where the driving perturbation frequency affects the various characteristics of the observed capillary waves on water surfaces, the plasma

pulsing frequency also impacts the observed capillary wave modes on the bubble boundary. While resonant modes can be excited immediately after discharges are initiated, capillary waves relax into steady-state dominant modes that are associated to the pulse frequencies. Varying the pulse frequency, ranging from 100 Hz to 1 kHz, we investigated the relationship between plasma pulsing frequency and the associated capillary wave modes.

As discussed previously, we have adapted the language often used in mathematics to describe the observed star polygons arising from capillary waves propagating on the bubble boundary. An n-pointed star polygon will be identified as the associated n mode.

With a pulse frequency ranges from 100 Hz to 1 kHz, modes from n = 2 to 12 were observed, some of which are shown in Fig. 7.8. At frequencies lower than 100 Hz, no observable surface perturbation was recorded. Frequencies above 1 kHz was not investigated due to imaging limitations. Both steady-state dominant modes and transient resonant modes are shown here. Multiple capillary wave modes are possible at a given pulsing frequency due to excitation of transient resonant modes, as discussed in the previous section.

We observe that a steady-state dominant mode will eventually evolve only after a significant number of pulses. The relationship between the plasma pulsing frequencies and their associated wave modes are shown in Table. 7.1. As discussed in previous section, the wave number of capillary waves at the interface of an air bubble suspended in water can be calculated and depends only on oscillation frequency of the waves and surface tension at the

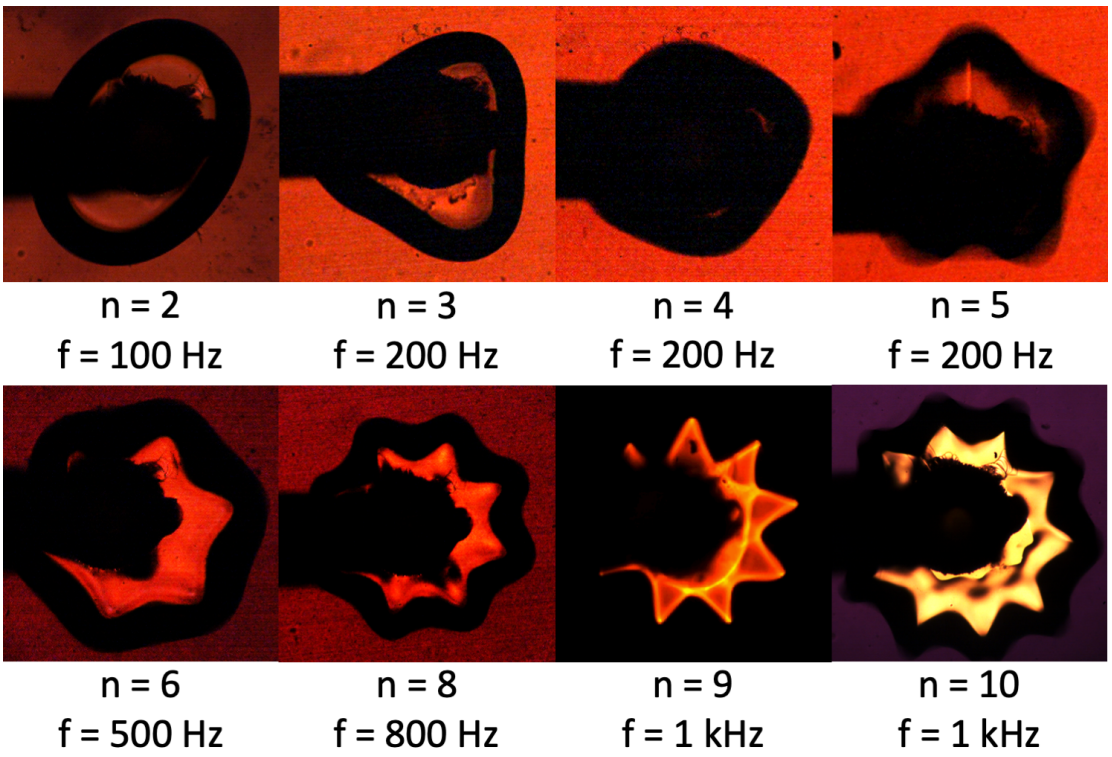

Figure 7.8: Capillary wave modes.

Plasma pulse frequency	Steady-state wave modes
100 Hz	2
200 Hz	3, 4
500 Hz	6
800 Hz	8
1 kHz	8, 9, 10, 12

Table 7.1: Plasma pulse frequency and observed steady-state wave mode

interface, in Eq. 7.1. Thus with a known bubble size, the resulting wave mode can be predicted. Assuming that the steady-state wave mode is only driven by the pulsed plasma and applying the dispersion relation of capillary waves due to surface tension onto the interface,

the capillary wave modes, n, can be calculated as:

$$n = \sqrt[3]{\frac{f_{exc}^2 \tilde{\rho} \pi^2 D^3}{8\sigma}} \tag{7.7}$$

where f_{exc} is plasma excitation frequency, $\tilde{\rho}$ is the sum of densities of air and water, D is diameter of bubble, and σ is interfacial surface tension. This relationship is shown in Fig. 7.9. For a specific bubble diameter, increasing the plasma pulse frequency perturbs the boundary at a higher rate, thus reducing the wavelength of the induced capillary waves and increasing the wave modes n. At a specific plasma pulse frequency, wavelengths of the induced capillary waves remain constant; larger diameter leads to larger circumference where oscillation propagates, thus result in increase in the wave mode number n.

Calculated values of capillary wave modes and data obtained are compared in Table. 7.2. Out of 9 cases documented here, 8 matched. Good match between calculation and data suggests that steady-state dominant modes are indeed driven by plasma pulse frequency and restored by surface tension.

7.5 Observation of sympathetic resonant oscillations

Capillary wave oscillations can resonantly transmit to adjacently trapped bubbles. As capillary waves developed along the interface of the primary bubble excited by streamers, surface oscillations can also develop in secondary bubbles nearby, as seen in Fig. 7.10. This effect

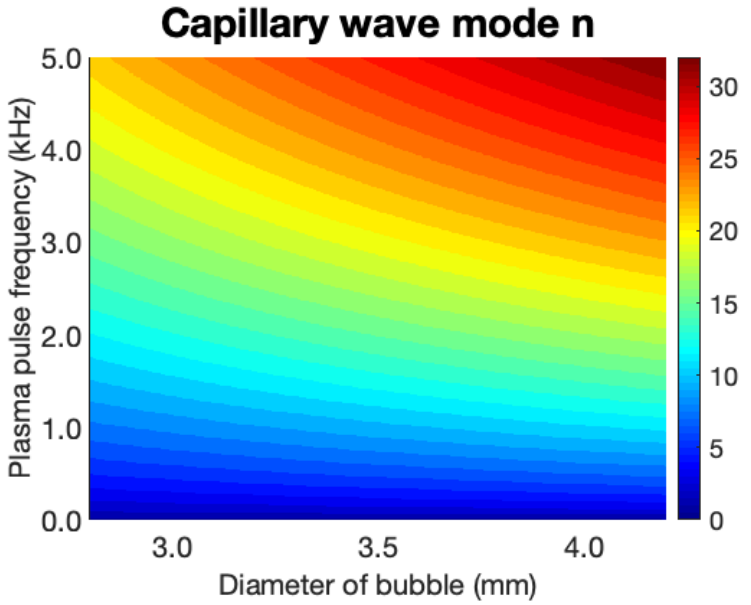

Figure 7.9: Calculated wave mode as a function of plasma pulse frequency and diameter of bubble.

Case	Pulse frequency	Diameter of bubble (mm)	Measured n	Calculated n
1	100 Hz	3.44 ± 0.17	2	2
2	200 Hz	3.00 ± 0.15	3	3
3	200 Hz	3.27 ± 0.16	3	3
4	500 Hz	3.48 ± 0.17	6	6
5	800 Hz	3.50 ± 0.17	8	8
6	1 kHz	3.51 ± 0.18	9	9
7	1 kHz	3.61 ± 0.18	10	9
8	1 kHz	3.76 ± 0.19	10	10
9	1 kHz	3.90 ± 0.19	10	10

Table 7.2: Comparison of capillary wave modes n measured and calculated.

could possibly be attributed to two different driving mechanisms.

Leakage of electric field in the excited bubble can potentially induce breakdown in the adjacent bubble, thereby giving rise to oscillations there at the secondary bubble. As shown in Fig. 7.11, discharges can be observed in both primary and secondary bubbles. Analogous

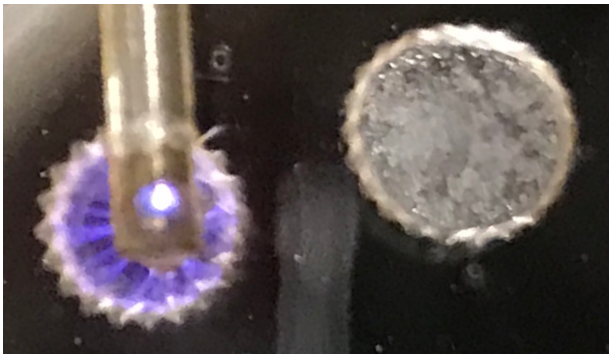

Figure 7.10: Surface perturbation in secondary bubbles.

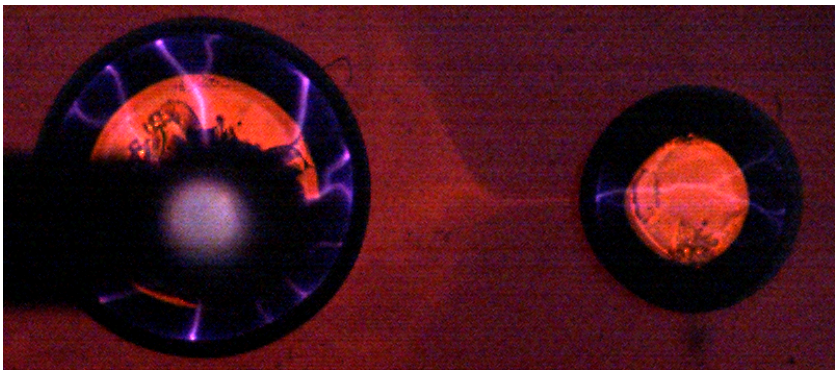

Figure 7.11: Streamer excitation in primary and secondary bubble.

to development of capillary waves on surface of single bubble, discharges inside secondary bubble likely perturb the surface and launch capillary waves. Secondly, capillary waves along the interface give rise to acoustic oscillations in the liquid itself. If these oscillations are resonant with a mode number in the secondary bubble, then the bubble can develop sympathetic capillary wave oscillations. As such, adjacent bubbles can be coupled to the acoustic field of the driven bubble. The presence of compression waves in the bulk liquid is consistent with previous results: shadowgraph taken showed active density gradient in

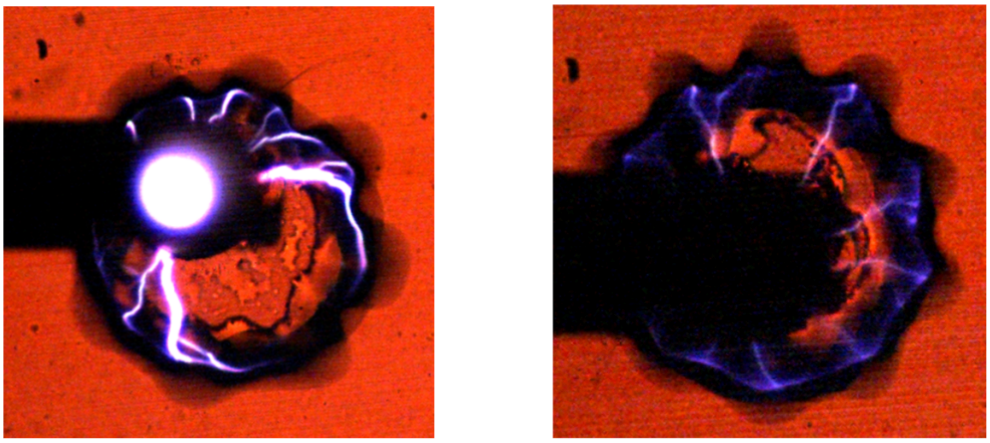

(a) Discharge traveling on perturbed surface in bubble not centered on electrode.

(b) Self-organization of discharge in bubble centered on electrode.

Figure 7.12: Self-organization of subsequent streamers in perturbed bubbles.

the bulk liquid surrounding the bubble boundary, indicating local compression initiated by discharges inside bubble [105].

Observation of capillary waves developed in secondary bubbles indicates that capillary waves development on primary bubble is not a localized event, but can drive large-scale physics in the bulk liquid, such as forced diffusion of reactive species produced in the bubble. Capillary waves alter geometries of bubbles and can enhance electric field in regions of the bubble, allowing discharges to form. Thus long-ranged effects of capillary waves can potentially favor formation of discharges in secondary bubbles far away from electrodes.

7.6 Self-organization of streamers

Interestingly, capillary wave formation on the bubble liquid interface not only alters the surface itself, but also influences the spatial distribution of streamers inside the bubble. When the bubble is not centered on the high voltage electrode, part of the boundary is closer to the electrode resulting in asymmetrical distribution of electric field inside the bubble. Thus streamers tend to start at regions with higher electric field, reaching for surfaces closest to the electrode. These streamers initiate surface ionization waves on the interface, seen in Fig. 7.12a, which appears to travel along the perturbed interface towards region of lower electric field. For bubble that is centered on the high voltage electrode, streamers tend to extend radially outward towards the boundary evenly. These streamers also launch surface ionization waves on the surface, which can be seen in Fig. 7.12b.

While development of capillary waves can alter the electric field inside the bubble, it appears that the streamers come into contact with the boundary when the perturbed interface transitions between crest and trough. This is illustrated in Fig. 7.13. Here, plasma was pulsed at 800 Hz and images were taken at 3200 fps. As previously mentioned, capillary waves propagate at half the plasma pulse frequency, thus there are two pulsed plasma discharges during the time where peaks regain their initial position. Defining the frame at which the top peak is at its maximum amplitude as having a zero phase shift at 0 μs, we can see that at 2500 μs the peak has regained its initial position, with a phase shift of 2π. Stream-

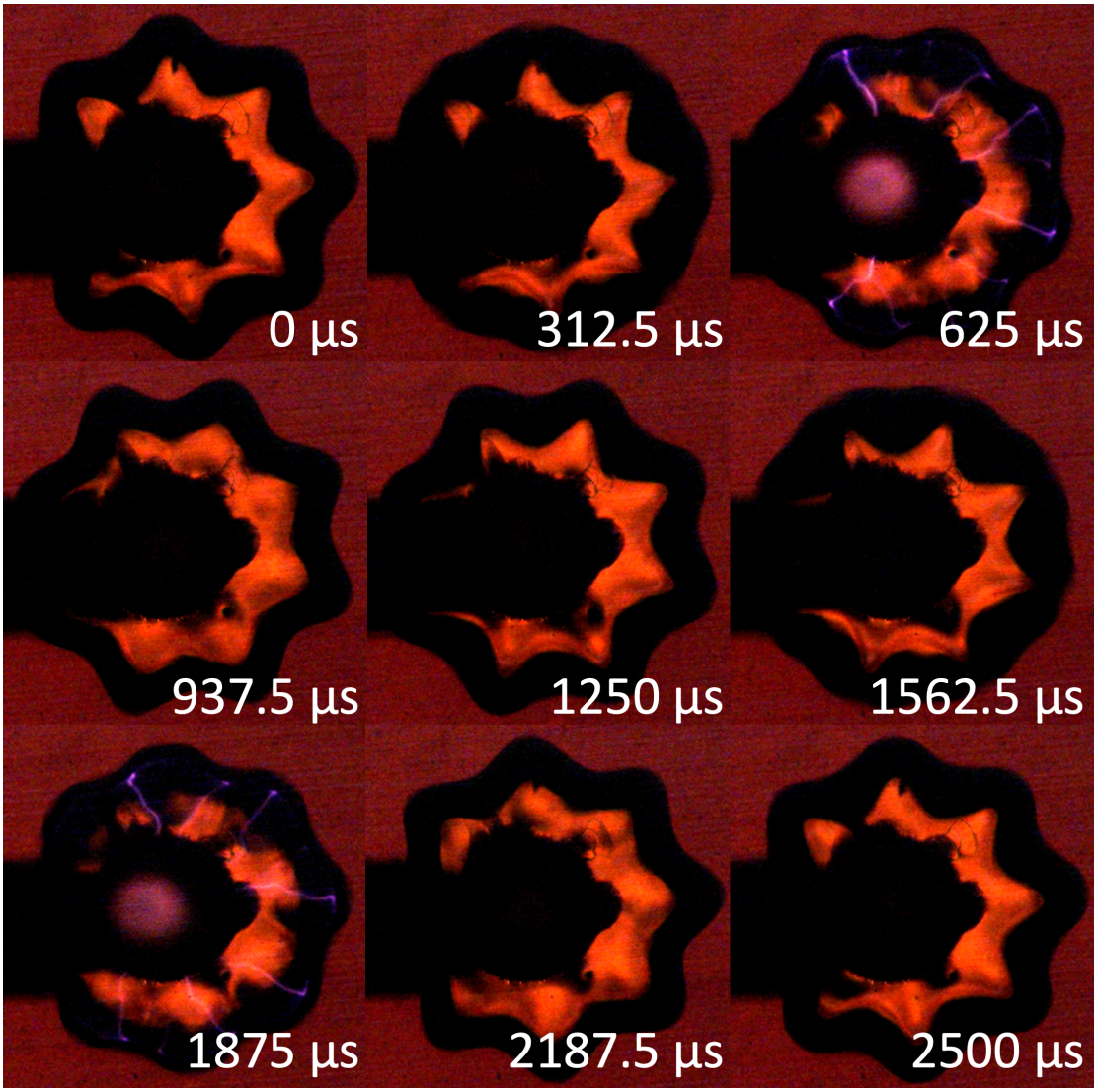

Figure 7.13: Positive feedback between capillary waves on interface and self-organization of streamers

ers can be observed at 625 μs (phase shift of $\pi/2$) and 1875 μs (phase shift of $3\pi/2$). This suggests that plasma comes into contact with the interface when the bubble is least perturbed, transitioning between peaks and troughs. However, close analysis of Fig. 7.13 will show that streamers tend to strike locations where troughs are present. As capillary waves develops on the bubble boundary, this alters the geometry of the interface thus the discharge gap between the boundary and high voltage electrode. With a radial electric field, electric field is enhanced at the troughs, which are closest to the high voltage electrode, leading to formation of streamers likely reaching for the troughs of the capillary waves formed. This observation is also consistent with the hypothesis that streamers interact with the interface mechanically. After streamers strike the interface, locations of contact are pushed radially outward, forming peaks after streamer discharge. Thus the self-organization of plasma results from capillary waves altering the geometry of the interface, but also provides energy to sustain the capillary waves. This coupling between self-organization of plasma and interfacial capillary waves is an example of positive feedback from a fluid effect which ultimately modifies a plasma effect.

The curious occurrence of self-organization has implications in regards to plasma-based water treatment. Since the oscillations are determining in effect the plasma liquid contact area, then two implications for plasma-based water treatment technologies become apparent: 1) plasma-induced fluid effects can have significant impact on the plasma-liquid contact

area and the associated induced reactivity and thus should not be neglected, and 2) the synergistic effect between plasma and liquid via self-organization may be exploited as a means to control and enhance plasma contact area with the liquid boundary.

Chapter 8

Propagation of streamers in bubbles

Bulk liquid conditions can impact the discharge conditions and resulting streamer discharges in the bubble. Bruggeman et al showed that breakdown voltage inside a bubble decreases with increasing conductivity [73]. Hamdan and Cha found that streamer travelled across the axis of the bubble in distilled water (conductivity of 5 μS/cm) [33]. Sommers et al observed that streamers propagation along the surface of bubbles in deionized water (conductivity of 0.07 μS/cm) [67]. A computational study by Babaeva and Kushner concluded that increasing liquid conductivity gives rise to streamer propagation along the surface of the bubble [29].

In this chapter, we investigate streamer discharges inside a bubble under various liquid conductivities. Streamer intensity, inferred from light emission, and propagation mode in the bubble were found to be strong functions of solution conductivity. Streamers tend to propagate along the interface when liquid conductivity is high. Water behaves as a lossy

dielectric when conductivity is low, and charging effects become significant and affect streamer propagation inside the bubble. An attempt was made to also study the effects of relative permittivity of the liquid. However, we were unsuccessful in initiating any visible discharges in bubbles in transformer oil (approximate relative permittivity of 2) at voltages up to 20 kV. The lack of breakdown may be due to the lack of free charge carriers in the oil as well as the fact that the oil is nonpolar so polarization charge density, which can enhance the local electric field at the interface, was absent.

8.1 2-D plasma-in-liquid discharge cell

The 2-D plasma-in-liquid discharge cell is described in Section. 3.3 and shown in Fig. 3.6. Liquids used in this experiment include (1) deionized water, (2) stock conductivity solution from Thermo Scientific with conductivity of 12.9 mS/cm (stock ID#: 011006), and (3) stock conductivity solution from Thermo Scientific with conductivity of 1.413 mS/cm (stock ID#: 01100710).

Streamers were excited using a nanosecond pulsed power supply (Eagle-Harbor Technology). For this study, a single pulse with peak voltage of 20 kV and pulse width of 120 ns was applied. Voltage and current signals were measured using a 2 GHz oscilloscope (LeCroy WavePro 7200), in combination with a Tektronix P6015A high voltage probe and a 6600 Pearson current transformer coil. To capture time-resolved images of the streamer

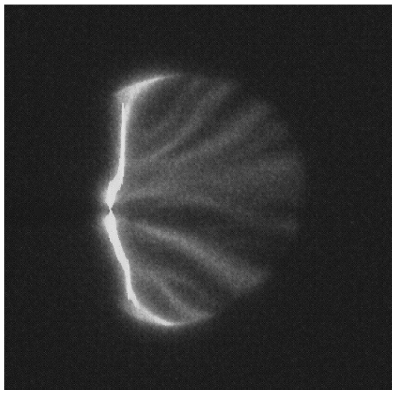

(a) JPEG image exported from Andor software.

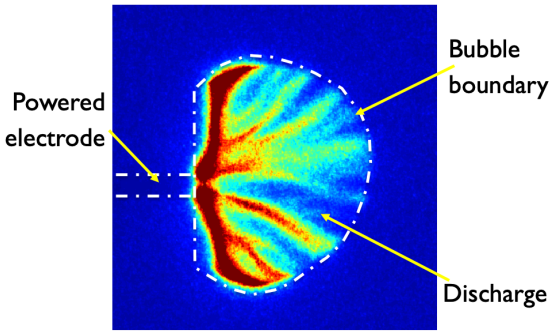

(b) Image of MATLAB post-processed data

Figure 8.1: ICCD image analysis.

discharge, an ICCD camera (Andor iStar 334T) in combination with a Nikon DSLR camera lens (Nikkor Lens AF Micro-Nikkor 60mm f/2.8D) was employed. A delay generator (BNC, Model 565) was used to control the timing offset between the pulse and the camera, where a pulse is sent to the power supply to trigger a discharge and another to trigger the camera. Each image here corresponds to one voltage pulse. Delay between the camera trigger and excitation pulse ranges from 0 to several ms, with sensitivity of 1 ns. Exposure time per frame was set at 5 ns. Images were captured at least ten seconds apart. Images captured were exported to MATLAB as an ASCII file and were post-processed using a custom written script. The raw image rendered by the software Andor Solis [123] is shown in Fig. 8.1a, and the MATLAB post-processed image is shown in Fig. 8.1b. In the post-processed images, red and blue denote high and low intensity of measured luminance respectively.

8.2 Modeling of electric field

ANSYS EM Suite 18.1 Maxwell was used to model the electric field inside the bubble. The 2-D geometry modeled is shown in Fig. 8.2. The potential of the cathode was set to -10 kV, shown in the top of the figure in orange. The anode was modeled as two rectangular electrodes lining the gas injection port, analogous to the cross section of a cylindrical hollow tube, both at excitation potential of +10 kV. Water, as a material, was selected from the software's library, and has a dielectric constant of 81. Conductivity varied in the different cases presented here.

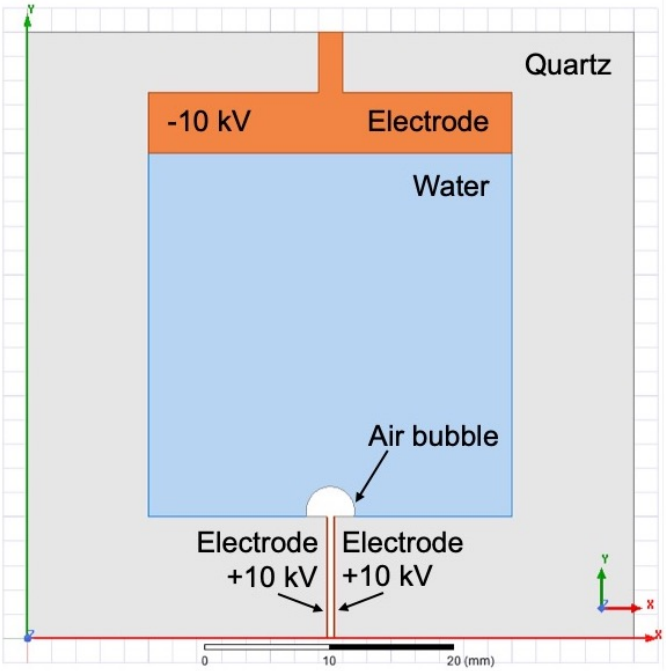

Figure 8.2: Geometry used in Maxwell electric field modeling.

The resulting electric fields inside the bubbles submerged in water with conductivity of 12.9 mS/cm is shown in Fig. 8.3a. Similarly across all three cases (two of them not shown), the magnitude of the electric field is high at the tip of the anode due to geometrical field enhancement. At the contact point between the bubble, water and the plexiglass, sharp angle at the interface enhances the magnitude of the electric field as well. While there is stronger electric field in the bubble in high conductivity water, it was similar in magnitude across all cases, indicating that the difference in discharge behaviors is not due to variations in electric field in the bubble. Sufficient electric field, far exceed the necessary electric field of 30 kV/cm to establish streamer discharges in dry air [117], was observed in all cases.

At high conductivity, the liquid acts as a conductor and results in a small electric field in the liquid phase. As conductivity of liquid decreases, the charge relaxation time lengthens. Water no longer acts as a conductor but more as a lossy dielectric. Thus larger electric field gradients in the liquid phase were observed in the case of water with conductivity of 1.413 mS/cm and deionized water, the latter case is shown in Fig. 8.3b. This suggests that presence of charge carriers in solution might impact discharge behavior in the bubble.

There are two implications as a result of the variation of conductivity altering the electrical characteristics of water. First, the voltage across the bubble is no longer the applied voltage when liquid conductivity is low, but it is reduced owing to polarization of the surrounding liquid. For the case of water of high conductivity, the effective discharge gap is

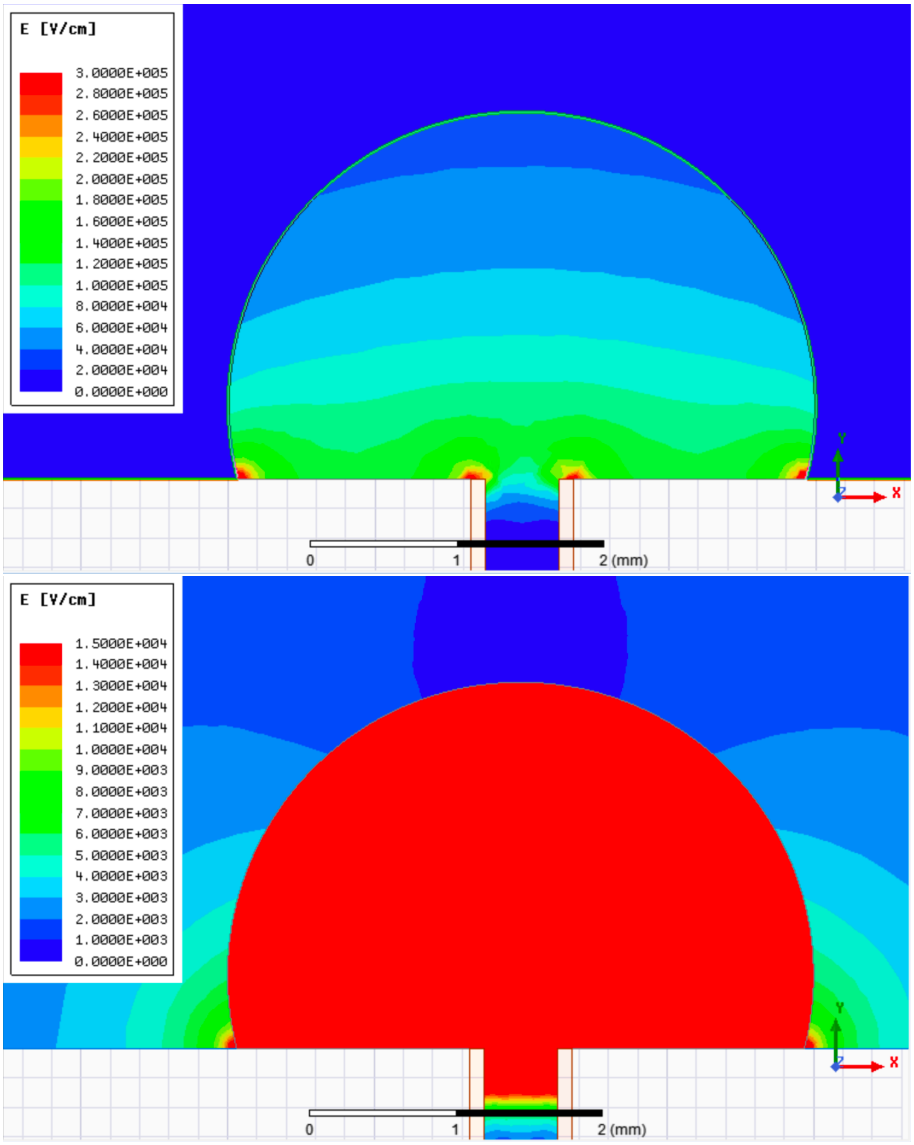

Figure 8.3: Electric field modeled in Maxwell for bubble in (a) water with conductivity of 12.9 mS/cm (b) deionized water (scaled down)

the distance between the anode and the surface of the bubble, appearing as if the liquid is shorting out the gap. Thus the electric field is slightly stronger in cases of higher liquid conductivity. Second, finite fields in the liquid phase for cases of lower conductivities may affect ion transport in the liquid and play a role in affecting discharge behavior. Charges in the interfacial layer can shield out discharges and promote propagation along the axis of the bubble rather than along the interface.

8.3 2D STREAMER PROPAGATION IN A BUBBLE

The time evolution of the propagation of streamers in bubbles in water with high conductivity (12.9 mS/cm) is shown in Fig. 8.4. High electric field at the electrode tip led to initial development of streamers. At 6 ns, both axial and interfacial streamers could be observed. High electric field at the base of the bubble associated with the plexiglass-air interface promotes propagation of streamers traveling perpendicular to the axis of the bubble. The role of charging can be investigated to understand the evolution of the patterns with time. The relaxation time can be determined from the ratio of its permittivity ε to its conductivity κ, $\tau = \frac{\varepsilon}{\kappa}$. In this case, the conductivity of the water is 12.9 mS/cm, which gives a charge relaxation time of 0.55 ns. The short charge relaxation time means that at least over the observation time scales, charge deposited by the streamer onto the surface of the bubble can be dissipated between frames. This suggests that charging effects, which would other-

wise limit magnitude and lifetime of currents, are reduced at higher conductivities. The interfacial streamers can therefore sustain a higher current and thus stall out axial streamers, which can be seen at 20 ns where interfacial streamers became more intense than axial streamers. Refraction of electric field at the interface further enhances local electric field, along with strong electric field at the tip plasma channels, leading to streamers preferentially circumnavigating along the bubble surface towards the cathode. This observation is consistent with Babaeva and Kushner's finding on production surface-hugging streamers in bubbles at large dielectric constant and conductivity [29]. However, it is important to note that while surface hugging streamers dominate, axial streamers persist in all frames with a much weaker intensity. Thus there is sufficient volume ionization in the bubble to sustain streamer formation.

Between 20 ns and 34 ns, the surface-hugging streamers continue to propagate under the influence of its own space charge field and the applied electric field. At later stages of propagation, it is possible to estimate the speed of streamer propagation along the interface. Analysis of the locations of the surface discharge front between 26 and 34 ns gave an estimated average traveling speed of the order of 0.1 mm/ns. This is an order of magnitude lower than that measured by Petrishchev et al [124]. This discrepancy can be attributed to their use of distilled water which has a lower conductivity and thus a larger charge relaxation time. Charge accumulation at the plasma-liquid interface enhances the propagation

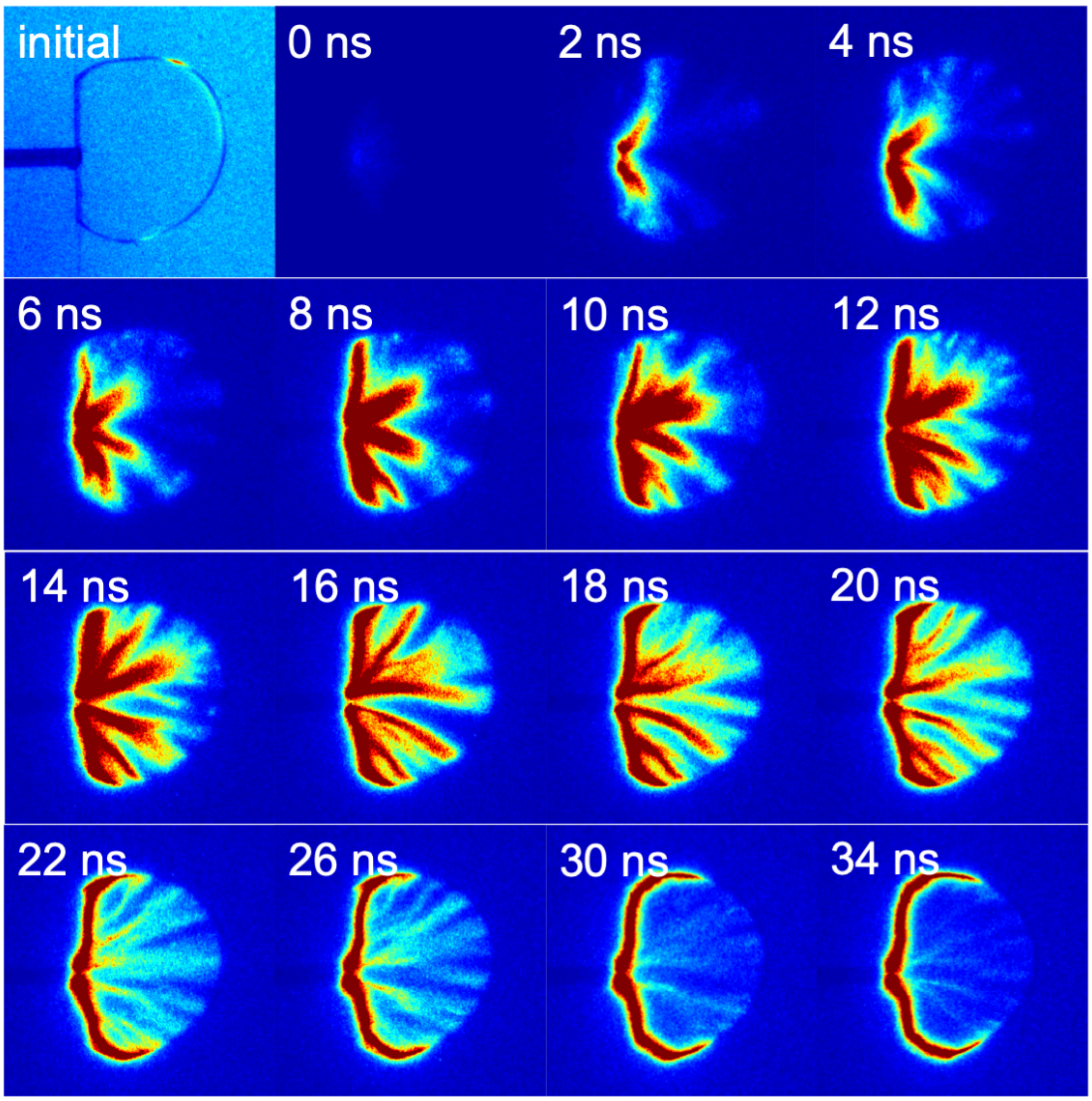

Figure 8.4: Time-resolved images of streamer development in bubble in water with conductivity of 12.9 mS/cm.

of surface ionization wave, while reduced loss of space charge sustains the plasma column. However, the length of observed surface ionization wave did not continue to grow during the pulse but remained at the same length seen at 34 ns during most of the pulse. Maximum distance travelled by the surface ionization wave is likely limited by the energy of the pulse and geometry. By geometry we refer to the angle between the applied electric field and the propagation vector; that is, at the extremes of travel, the propagation vector and the applied electric field are no longer parallel. In this case of maximal length, we can expect that ionization processes and losses balance along the streamer column.

The observed propagation pathways of streamers were supported by the measured voltage and current across the discharge cell, which is shown in Fig. 8.5a for the case with liquid of high conductivity. Short charge relaxation time allowed a positive current to be sustained throughout the entire pulse due to the lack of charge effects in the liquid. The voltage drop after the rise time can be attributed to the large increase of current depositing charges on the surface, lowering the effective voltage drop across the gap, which also leads to a subsequent decrease in the current measured. With no charging effects observed, current reduced quickly as voltage across discharge gap dropped.

In the case of the water with medium conductivity (1413 μS/cm), no strong interfacial streamers could be observed. The propagation of streamers in bubbles in this case is shown in Fig. 8.6. Similar to the previous case, high electric field at the electrode tip led to initial

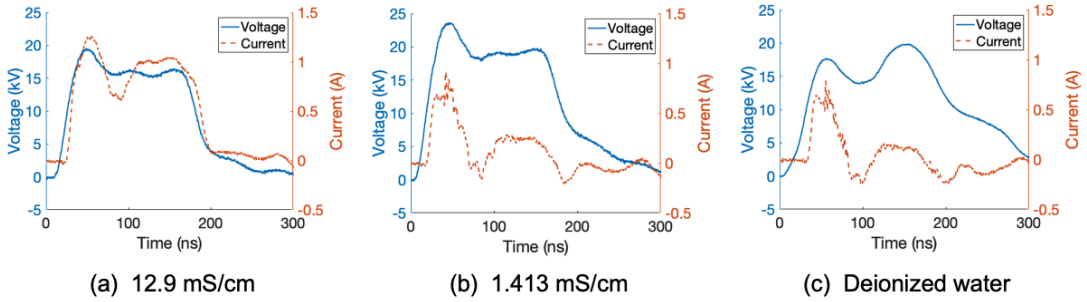

Figure 8.5: Measured current and voltage for a single pulse for a) water with conductivity of 12.9 mS/cm, b) water with conductivity of 1.413 mS/cm, c) deionized water.

breakdown locally, at around 2-6 ns. However, only a localized corona-like discharge can be seen at anode, with weak axial streamers reaching the opposite bubble surface. At 12 ns, only weak surface discharges on the bubble surface and localized discharge at the anode tip could be seen. The conductivity of this liquid is 1413 μS/cm, which gives a charge relaxation time of 5 ns. As a result, the initial development of streamers has the potential to charge the surface and halt the propagation of axial streamers. The presence of dark region between discharge at the anode and surface discharge at bubble surface at 12 ns can be attributed to ions traveling towards cathode losing energy through collisions with gas particles. Electron impact ionization processes at the interface led to faint emission observed at the interface. Slowly, as charges dissipate in the liquid, weak axial streamers can form. However, it appears that charging of the surface led to reduced effective electric field across the discharge gap and resulted in axial streamers of much lower intensity. In summary, two factors likely give rise to the observed weaker discharge development in the case of water with conductiv-

ity of 1413 μS/cm: 1) interfacial charging and 2) reduced concentration of charge carrier in the liquid. The latter factor ultimately limits the maximum current that can develop along the interface as well as the axis. This was also supported with the measured voltage and current during discharge, shown in Fig. 8.5b. Charging effects at the interface became important. Charges deposited on the bubble surface lead to the development of an opposing electric field in the gap and subsequent termination of the discharge, which can be observed as current rapidly decreased.

The evolution of discharge morphology in time with deionized water differed significantly from the high conductivity cases. These differences are attributed to charging effects. The time-resolved propagation of streamers in bubbles in deionized water is shown in Fig. 8.7. Strong electric field at the tip of the electrode still led to initial development of streamers there, similar to previous cases. However, with an approximate conductivity of 0.1 μS/cm, deionized water has a charge relaxation time of 71 μs, about 1000 times longer. Thus charging effect is even more dramatic. The deposited surface charge presumably causes the streamers to stall, which was observed as decreased emission intensity between 4 and 12 ns. Between 12 and 158 ns, there was no discernable signal in the images taken, indicating there is either very weak or no discharges between the gap. A weak localized discharge can be observed after 158 ns. It is important to note that from 158 ns onwards, the photon counts of captured images were scaled up 10 times, comparing to frames shown in

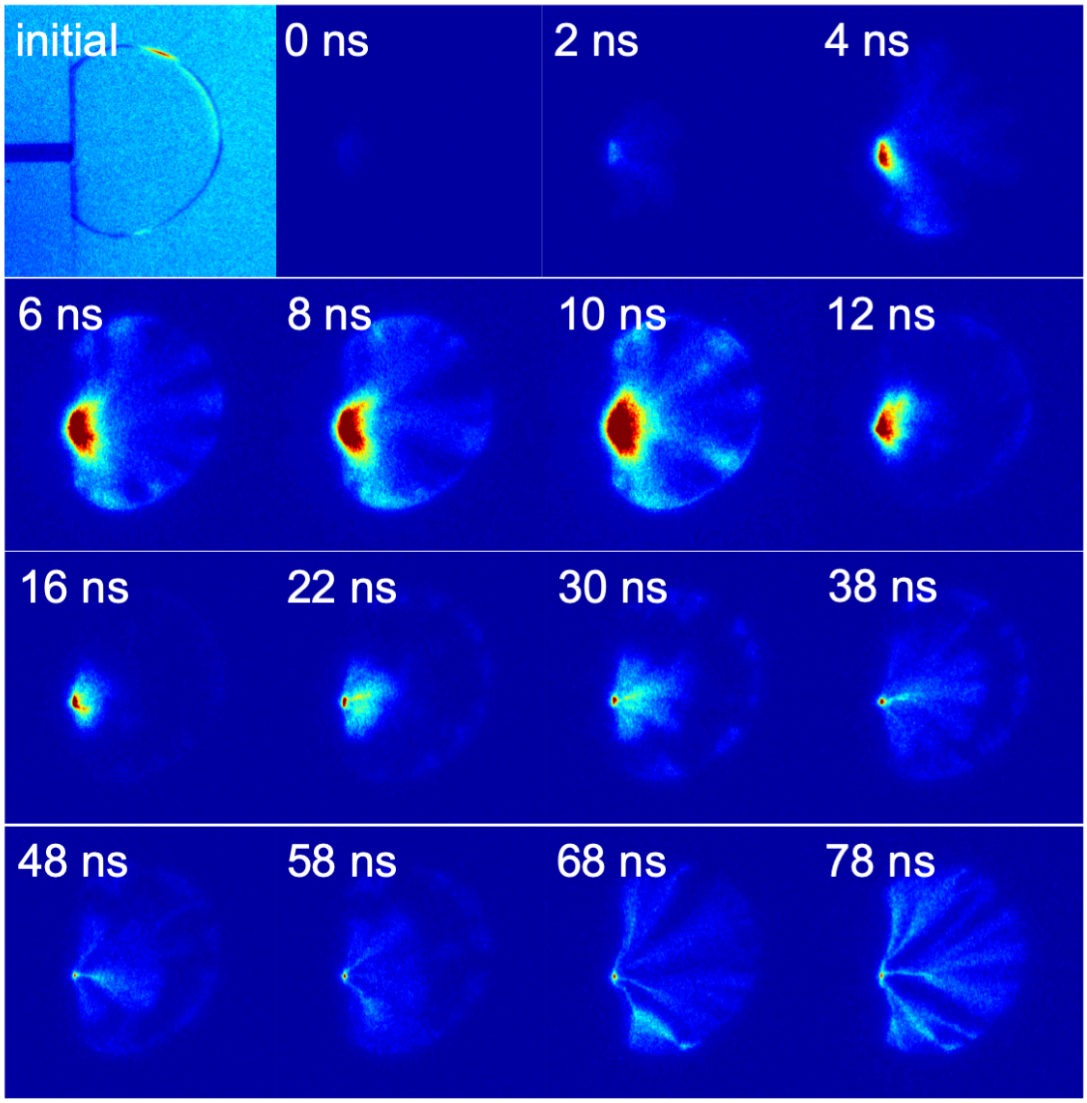

Figure 8.6: Time-resolved images of streamer development in bubble in water with conductivity of 1.413 mS/cm.

0-12 ns, in order to discern discharge morphology observed, indicating that the reformed discharge is much weaker in intensity comparing with the primary discharge. In the measured voltage and current, shown in Fig. 8.5c, sufficient charges were deposited on the bubble surface for restrikes to develop, which was measured as a negative current. However, this was too faint to be measured using the ICCD camera. Restrikes dissipate deposited charges, allowing streamers to develop again between 120-180 ns. The deionized water case highlights the importance of both 1) lifetime of deposited surface charge relative to the evolution time of the discharge streamer and 2) concentration of charge carrier in the liquid on discharge development. The charge carrier concentration in the liquid determines the streamer relaxation time. It may play an additional role in determining the local electric field. Future experiments will be required to ascertain the relative importance of the surface charging as compared to the role of free charge carriers. The importance of finite number of charge carriers is illustrated in this case since the discharge does indeed develop over time scales shorter than the relaxation time of the liquid.

Considering all three cases, the waveform data clearly shows a drop in average current with decreasing conductivity. Integrating the positive area under the curve of the sum between voltage and current, the electrical energy dispensed per pulse was calculated for each case. The energies per pulse for 1) water with conductivity of 12.9 mS/cm, 2) water with conductivity of 1.314 mS/cm, and 3) deionized water are 1.90, 0.85 and 0.45 mJ respectively.

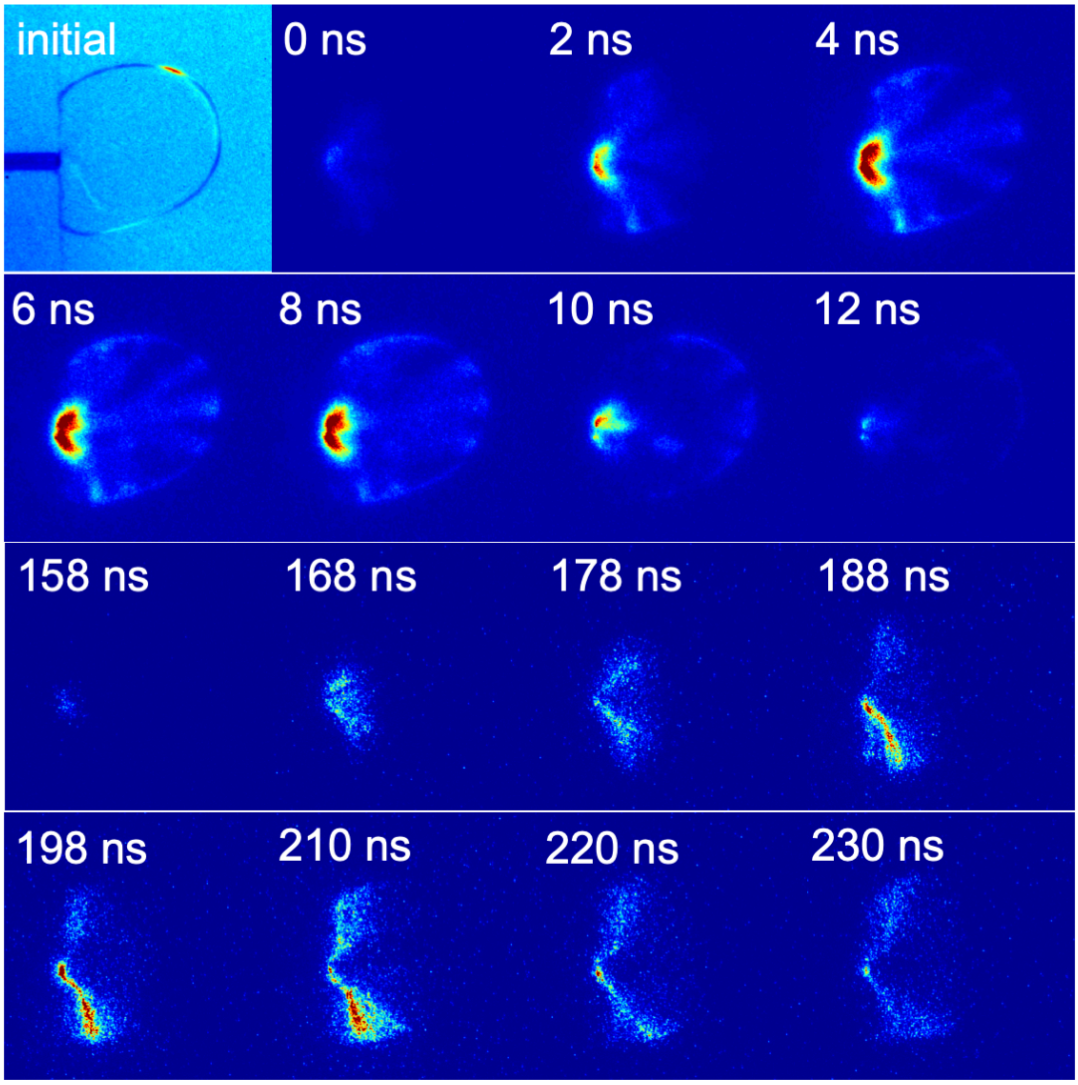

Figure 8.7: Time-resolved images of streamer development in bubble in deionized water.

The higher energy at high conductivity is associated with a larger current. Plasma density and production of reactive species typically scale with discharge current. The higher current also gives rise to increased gas heating. Energy efficiency is an important consideration for plasma to be considered to be a competitive method for water treatment. As such, it is desirable to minimize these heating effects. Realistically, it will be difficult to alter the conductivity of target source water for treatment, as contaminants tend to increase electric conductivity of water. Alternatively, a shorter pulse rise time might be able to trigger production of reactive species while minimizing the loss of charge carriers through development of surface hugging streamers. Having the rise time shorter than the charge relaxation time is a possible means to manage the dissipation.

Chapter 9

Plasma-induced flow in the bulk liquid

Chapter. 6 showed that plasma can drive fluid flow at the plasma liquid boundary, generating forced flows with velocities up to 1.5 mm/s in a 2-D system, leading to formation of sharp velocity shear near the interface and vortices in the bulk liquid. Fluid is drawn into the boundary layer, forced along the interface, and ejected into the bulk liquid. The development of large-scale circulation in bulk liquid can potentially transport plasma-derived reactive species far away from the interface.

The observation of plasma-derived flow is consistent with Marangoni effect. The Marangoni effect arises from a plasma-induced surface tension gradient at the gas-liquid interface. The surface tension gradient be driven by spatial gradients in temperature or species concentration. Fluid of high surface tension pulls more stronger than that of lower surface tension, which leads to fluid flow in the direction away from region of low surface tension into re-

gion of high surface tension. In the case of thermo-capillary convection, which is in the case of only temperature dependence, fluid will flow from hotter to colder regions, as surface tension scales inversely with temperature for water. Miniewicz et al [107] showed that a laser light beam impacted onto a thin layer of liquid trapped between two glass plates behaved like a point-like heat source, leading to local surface tension change due to temperature gradient near the liquid-air surface and development of large-scale Marangoni flow. Streamers in contact with water can locally heat up the interfacial region [125] and lead to surface tension gradient in the gas-liquid interface. Shimizu et al [91] mapped the fluid flow field in an 8-mm deep water layer contained in a glass cell as a result of a streamer discharge on the air-water surface, and observed a maximum velocity of 2.5-3 cm/s towards the streamer contact point.

In Chapter. 8, we have shown that bulk liquid conditions can impact discharge conditions, in particular, water conductivity can alter the propagation of streamers in bubbles. At high conductivity, surface hugging streamers develop and stall out axial streamers, but also lead to larger current drop and increased associated thermal effects. At low conductivity, surface charging becomes a significant effect and screens out external electric field, which terminates the discharge. In this study, we investigate the effects of liquid conductivity on the plasma-induced flow field. Streamer core temperature in gas phase can reach up to 2000 K [126], and can locally heat up the interface region which lead to development

of Marangoni flow in the bulk liquid. The higher conductivity of water resulted in the appearance of a larger number of surface hugging streamers and increased energy dissipated per pulse. This led to a higher degree of localized heating thereby producing conditions necessary for the appearance of surface tension gradients and thus induced flow. In this study, we compared the 2-D velocity flow field as a result of nanosecond pulsed streamer discharges in an air bubble submerged in water with varying conductivities. For the 12.9 mS/cm and 1.413 mS/cm cases, the flow direction appeared to be clockwise on the left side of the bubble, where the induced flow traveled on the surface of the bubble away from the anode into the bulk liquid, with the return flow circulating back to the anode away from the interface. This is contrary to the 0.1 mS/cm case, where the flow direction was opposite. As resulting thermal effects, production of surface hugging streamers, and streamer intensities scale with liquid conductivities, the resulting surface tension gradient in the liquid layer will vary in both intensity and spatially, which can result in different flow directions.

9.1 Experimental methods

The 2-D plasma-in-liquid discharge cell used was described in Section. 3.3 and is shown in Fig. 3.6. Gas used in this study is ambient air. Liquids used in this study included stock conductivity solutions from Thermo Scientific with conductivities of 1) 12.9 mS/cm (catalog #011006), 2) 1.413 mS/cm (catalog #011007), and 3) 0.1 mS/cm (catalog #011008)

A single air bubble was injected into the contained liquid layer via the syringe. Plasma discharges were excited in the bubble using a nanosecond pulsed power supply (Eagle-Harbor Technology). For each measurement, 100 20-kV pulses (+10 kV at anode, and -10 kV at cathode) with pulse width of 120 ns were applied to the cell at a repetition rate of 10 Hz, described in Chapter. 8.

Particle image velocimetry (PIV) was employed to obtain the 2-D fluid flow field in the discharge cell and is shown in Fig. 9.1. A continuous wave 1-W 532 nm dual cavity Nd:YAG laser was used to illuminate the discharge cell. A Powell lens was used to convert the laser beam into a laser sheet. Thermo Scientific Fluoro-Max fluorescent particles with nominal diameter of 10-μm (catalog #36-3) were added into the liquids to visualize the fluid flow. These particles were composed of polystyrene, with Firefli fluorescent red dye incorporated in the polymer matrix. Excitation wavelength was centered at 542 nm and emission wavelength was centered at 612 nm. Density of the particles is 1.05 g/cm3, which is approximately 4.8% more dense than water. This can result in the sinking of particles to the bottom of the recess area, where these particles will experience friction with the quartz plate and do not follow the fluid flow faithfully. However, a high concentration of particles were added to the liquid, and we observed some to be suspended in the liquid layer. Fluorescent signals from stationary particles were subtracted from the signal using an average time filter (further explained in methods of software analysis). Polystyrene also has a dielectric constant of

2.56, which is significantly less than that of water and can potentially impact the resulting electric field. However the electric field is much larger in the gas phase than in the liquid phase, combining with the small amount of particles added by volume and mass, the seeding particles are not expected to impact the electrical properties of the liquid. Additionally, seeding particles can accumulate in regions of high velocities and induce surface tension gradients as well, which can impact the fluid flow measured. This effect was not considered in this study and is left to future work.

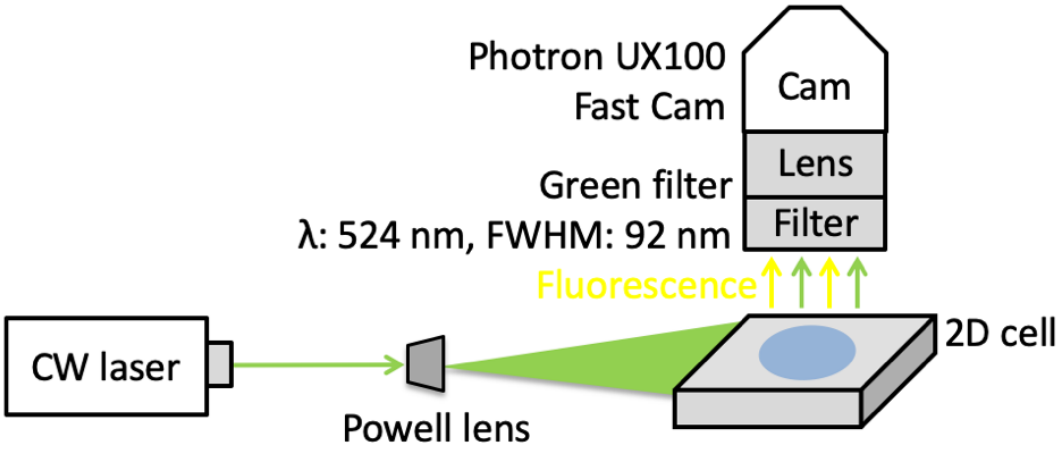

Figure 9.1: Experimental set-up of particle image velocimetry (PIV) with 2-D discharge cell.

A green filter with centered wavelength of 524 nm and FWHM of 92 nm was used to filter out the excitation light. Emitted light was recorded using a fast camera (Photron FASTCAM Mini UX100) in combination with a Nikon DSLR camera lens (Nikkor Lens AF Micro-Nikkor 60 mm f/2.8D). Images were acquired at 50 fps at 1,280 x 1,024 pixel resolu-

tion, yielding an exposure time per frame of 20 ms and a total of 500 images per measurement. The CMOS had 10-μm square pixels. A delay generator (BNC, Model 565) was used to trigger the camera and the power supply simultaneously. Images were captured using the Photron software package and exported as PNG files. The PNG files were cropped and converted into black and white using ImageJ, and analyzed using LaVision DaVis 8.4.0 [127]. Calibration was performed using a grid of dots with diameter of 0.5 mm and center-to-center spacing of 3 mm.

Delay generator was triggered manually through a button push and led to minor oscillation of the optics table, thus first 100 frames captured were discarded. In this study, the 101-300th frames (t = 2-6 sec) were analyzed to resolve the spatiotemporal development of plasma-induced fluid flow. An average time filter was created from all images within a specific data set. Signals from stray light across all frames were used to create this time filter, and were subtracted from all images from this data set. This boosted the signal to noise ratio as adding the average time filter removed recorded light that did not correspond with fluorescent from moving particles.

In order to calculate the fluid flow field, the position of light emission from fluorescent particles were compared between adjacent images, where the nth image is compared with the n+1th image to calculate the displacement of particles. The velocity vectors were calculated as the displacement of particles divided by the time between frames. The discharge

pulse was observed to perturb the boundary, due to momentum transfer from the streamers. Streamers also produced light emission that was recorded as emission from fluorescent particles. As such, the time-series used for flow field calculation utilized images taken in between pulses to minimize the effects of the streamer discharge. The repetition rate of plasma pulse excitation was 10 Hz (100 ms between frames), where the frame rate was 50 fps (20 ms between frames). Since the pulse width was only 120 ns, the bubble boundary was observed to be unperturbed 40 ms post-discharge. Given that the streamers were recorded in frames 1, 6, and so on, represented by frame 5n+1, the frames selected to create the time-series were made up of frames 3, 8, and so on, represented by frame 5n+3, which were taken 40 ms post-discharge. A geometric mask was used to reduce computational domain where fluid was absent (in the bubble) and regions of non-interest (right side of the image, in the shadow of the bubble), shown in Fig. 9.2.

9.2 Results and discussion

Fig. 9.3 shows the time evolution of fluid flow field on the left side of the bubble in water with conductivity of 12.9 mS/cm. Data was normalized to the same velocity scale with a range from 0 to 0.7 mm/s. Two flow patterns can be observed in the first frame (t = 2.04 s). A localized vortex traveling clockwise formed near the anode, on the left side of the bubble. The vortex included high speed flow appeared to go into the anode near the edge of the re-

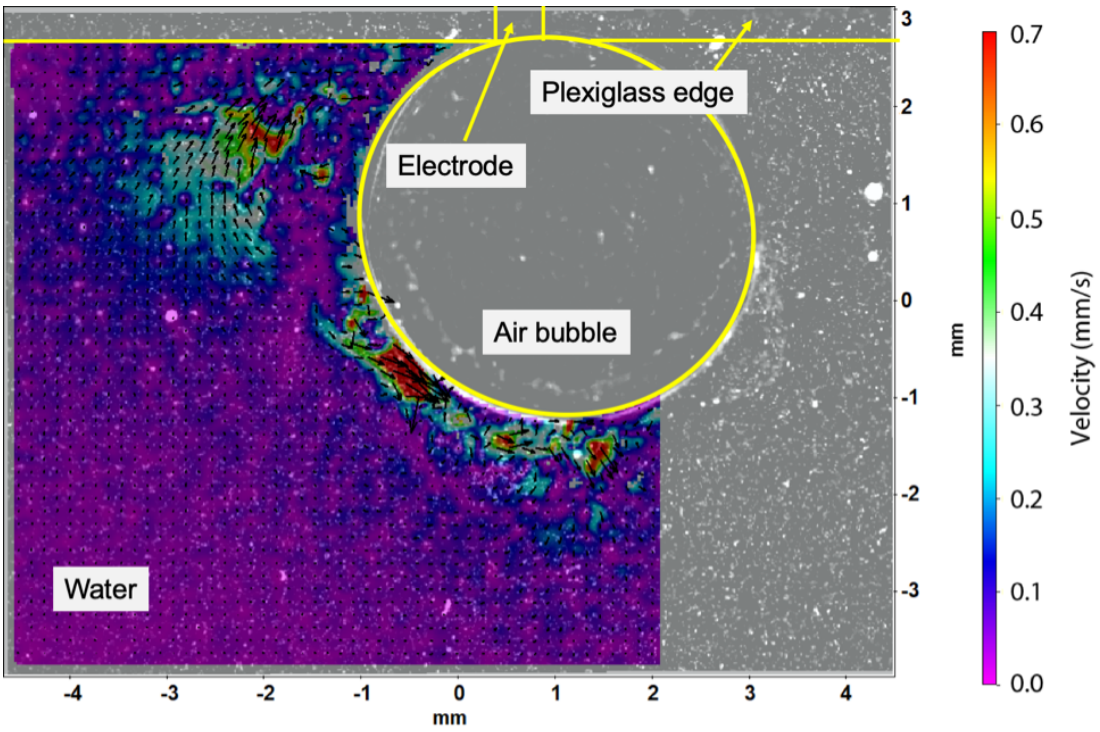

Figure 9.2: Plasma-induced fluid flow field with labeled structures.

cess area and away from the anode along the surface of the bubble. In addition, high speed flow, at approximately 0.7 mm/s, was observed traveling on the surface of the bubble, creating a velocity shear in the interfacial area between the bubble boundary and the bulk liquid. Each frame shown in Fig. 9.3 is separated by 0.5 s (5 pulses, pulse repetition rate: 10 Hz). After 1 second (10 pulses), a well-formed circulation pattern can be observed, which combined both the vortex and the velocity shear at the bubble surface. Fluid was drawn in near the edge of the recess area into the anode, traveled along the bubble interface and into the bulk fluid. Growth of the circulation pattern was clearly observed comparing the images. In

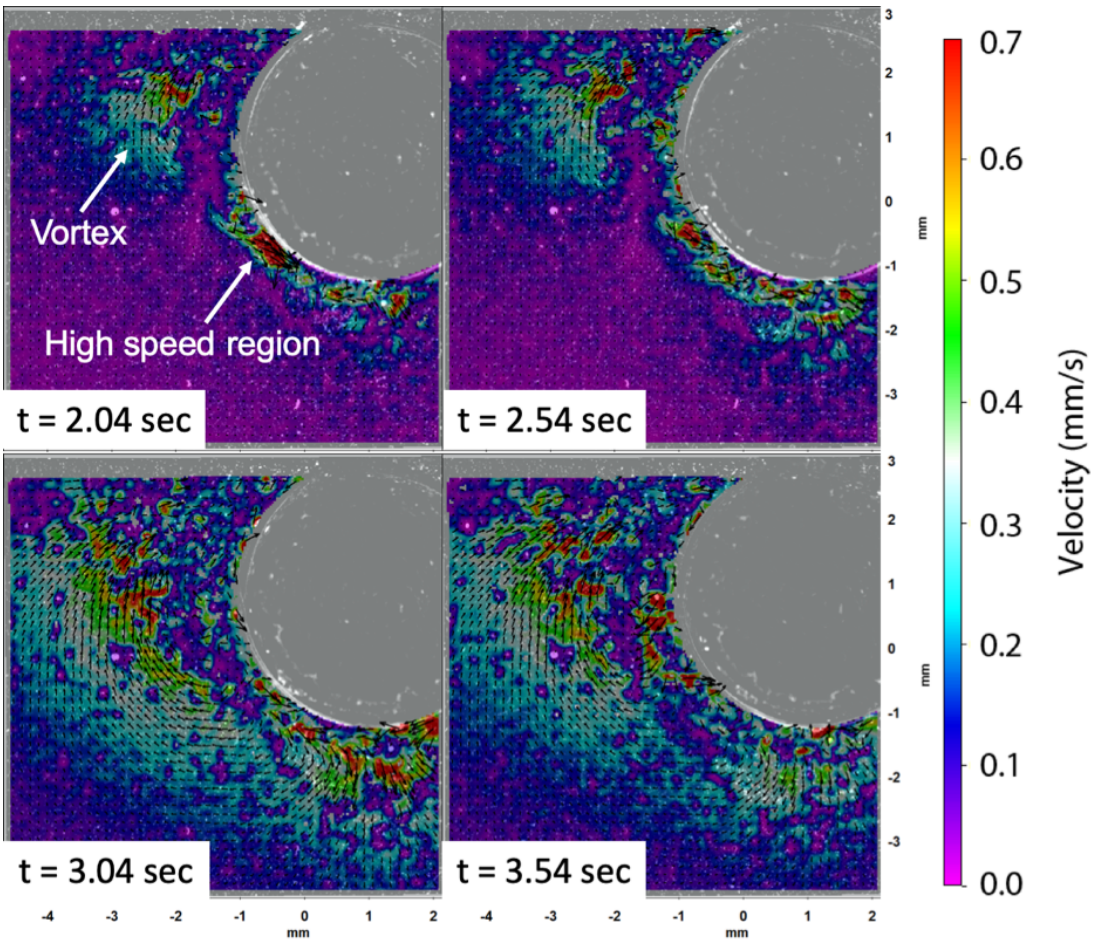

Figure 9.3: Fluid flow field of plasma-induced flow in water with conductivity of 12.9 mS/cm.

frame 1 (t = 2.04 s), majority of the bulk liquid was not driven by plasma-induced flow (purple region near the bottom left), while in frame 3 (t = 3.04 s), significant amount of the bulk liquid now has flow speed of 0.1 mm/s and above. Previous ICCD imaging of the single pulsed discharge observed the development of surface hugging streamers in bubble in high conductivity water (12.9 mS/cm) that traveled on the bubble surface, which increased the

contact area between streamers and the interface. Since energy dispensed per pulse scales positively with liquid electric conductivity, greater heating effects on the bubble surface were expected. This can contribute to the high fluid velocity resulting from Marangoni effects observed on the surface.

Fig. 9.4 shows the time evolution of fluid flow field for the case with 1.413 mS/cm.

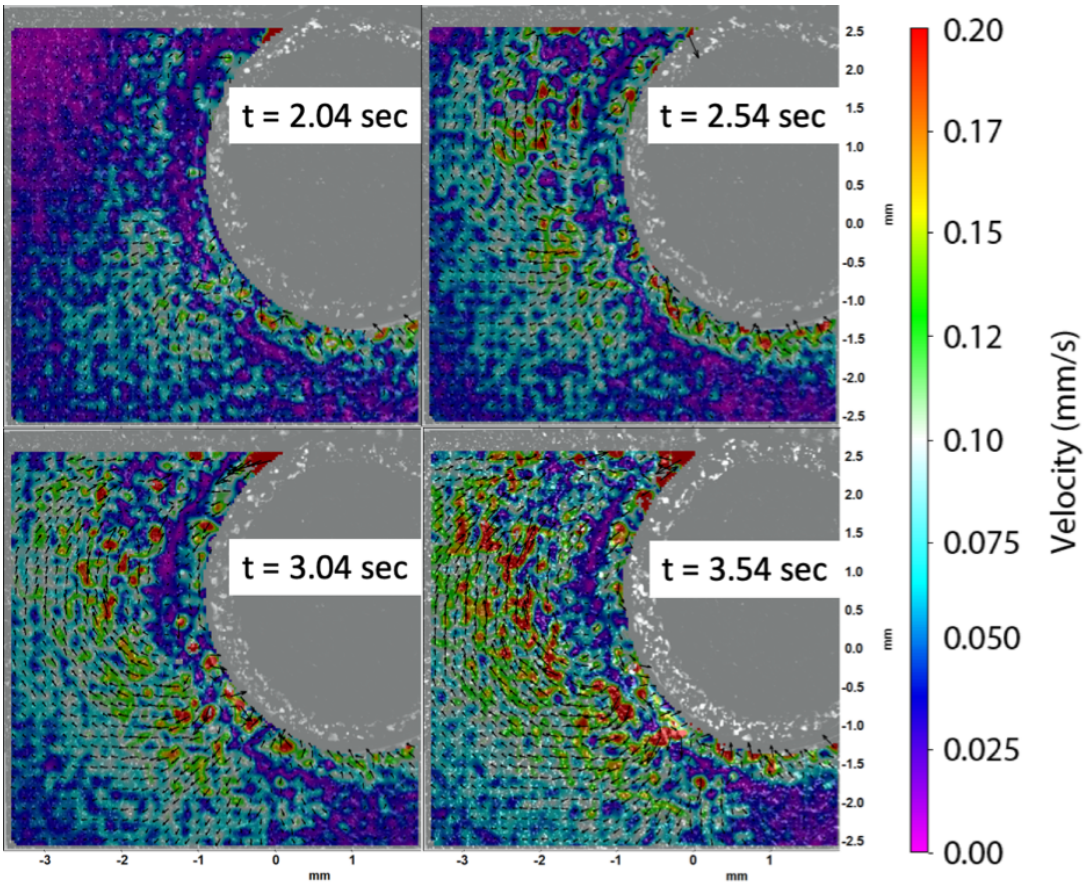

Figure 9.4: Fluid flow field of plasma-induced flow in water with conductivity of 1.413 mS/cm.

Data was normalized to the same velocity scale with a range from 0 to 0.2 mm/s. In this

case, a weak vortex traveling clockwise was observed near the anode, and an outward bulk fluid flow from the bubble surface can be observed in the bottom left of the image. Interestingly, on the bubble surface, there exists a thin layer of fluid that appears to flow into the surface, leaving a stationary layer in between the fluid flow into and away from the surface. The fluid flow velocity increased significantly between frame 1 (t = 2.04 s) and 4 (t = 3.54 s). In frame 1, majority of the bulk liquid has flow speeds of approximately 0.075 mm/s; but at frame 4, a large area in the bulk liquid has flow speeds above 0.12 mm/s. A large circulation pattern formed in the bulk liquid, which drove fluid towards the anode, around the bubble surface and into the bulk liquid again. A clear purple layer can be seen near the bubble interface in this image, which represents the stationary layer. ICCD imaging of the discharges obtained previously showed development of weak streamers reaching across the bubble in medium conductivity water (1.413 mS/cm) which filled the bubble volume. More uniform contact between streamers and bubble surface was observed. Thus charge deposition onto the surface leads to current and energy deposition, and subsequently development of Marangoni flow in the bulk liquid.

Fig. 9.5 shows the time evolution of fluid flow field for the case with 0.1 mS/cm.

Data was normalized to the same velocity scale with a range from 0 to 0.15 mm/s. Contrary to the previous cases, the flow direction is counterclockwise and is opposite to those from the previous cases. Over the course of 15 pulses, between frame 1 and 4, the surface ve-

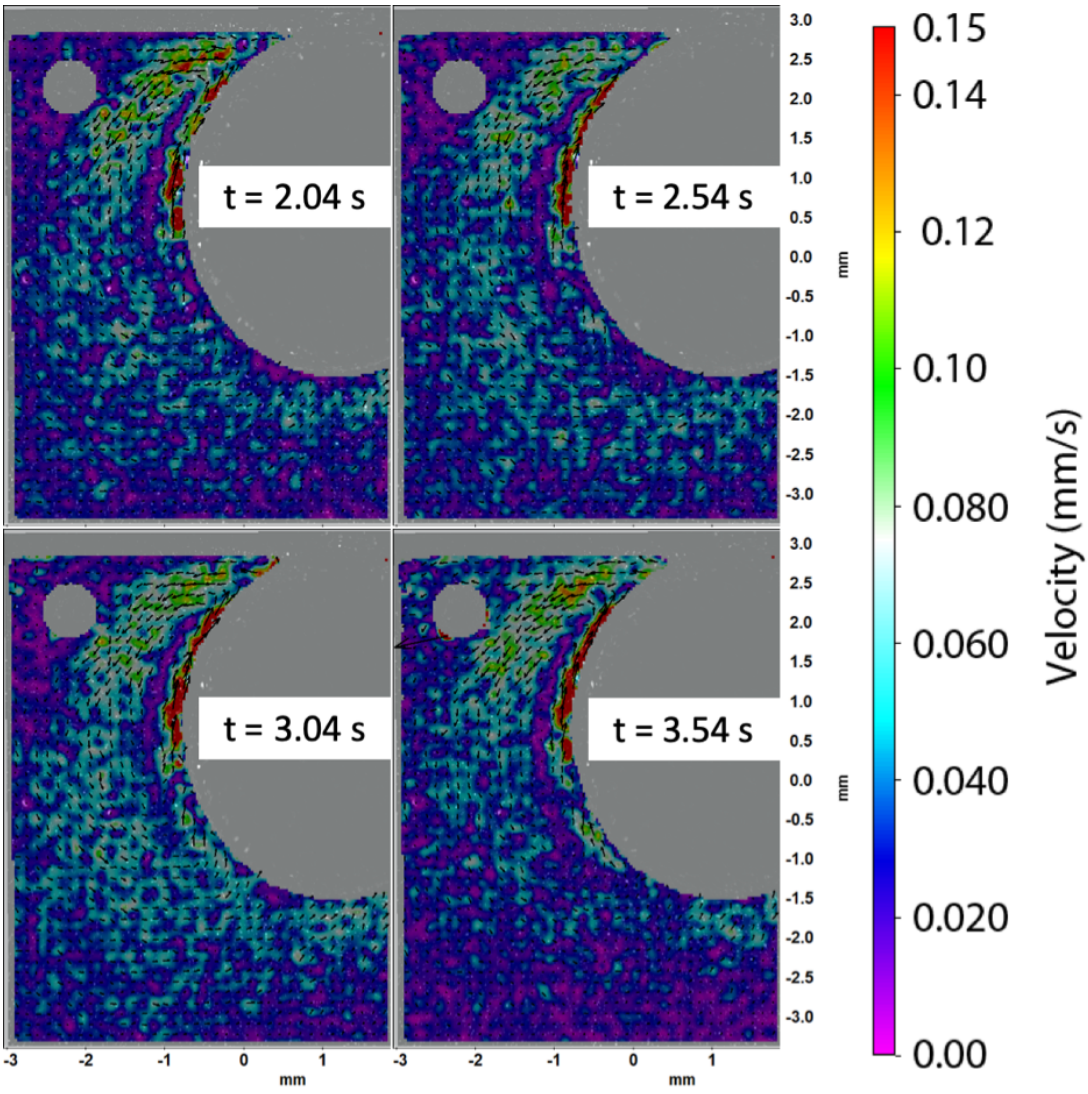

Figure 9.5: Fluid flow field of plasma-induced flow in water with conductivity of 0.1 mS/cm.

locity on the bubble appeared to be more intense, from approximately 0.13 mm/s to over 0.15 mm/s, but the flow fields in the bulk fluid do not appear to vary greatly. Discharge morphology observed in previous experiment obtained from ICCD imaging showed that the discharge primarily remained on the tip of the anode and quickly halted due to surface charging effects. Thus the heating effects appeared local, as streamers do not come into contact with the bubble surface. As a result, the surface tension gradients due to thermal effects remained localized as well. At such low conductivity (of 0.1 mS/cm), water acts a lossy dielectric rather than a conductor, thus joule heating due to conductive current is much lower. This can alter the spatial temperature gradients in the liquid, and potentially affect the fluid flow direction.

Marangoni number, Ma, is the ratio of thermal transport via convection due to gradient in surface tension to that of thermal diffusion

$$Ma = -(\frac{\partial \sigma}{\partial T})\frac{L\Delta T}{\eta \alpha} \tag{9.1}$$

where σ is surface tension, T is temperature, L is thickness of liquid layer, η is viscosity of liquid, and α is thermal diffusivity of liquid. Energies dissipated per pulse for 1) water with conductivity of 12.9 mS/cm, 2) water with conductivity of 1.413 mS/cm and 3) deionized water are 1.9 mJ, 0.85 mJ and 0.45 mJ respectively, as discussed in Chapter 8. With a pulse repetition rate of 10 Hz and after 2 seconds, the energies dissipated are 38 mJ, 17 mJ and 9

mJ respectively. Assuming energy is dissipated primarily as heat and evenly on the bubble surface (radius = 2 mm, circumference = 12.6 cubic mm), and negligible heat diffusion into the bulk liquid at short timescales, the temperature gradient of the interfacial region, liquid layer of approximately 0.5 mm thick from the gas phase region, can be calculated as

$$E = mc\Delta T \tag{9.2}$$

where E is energy dissipated, m is mass of the liquid, c is the specific heat of water, and ΔT is the temperature rise due to heating. Thus we can estimate that the temperature increase to be 2.91 K, 1.30 K and 0.69 K respectively, which yield Marangoni numbers of 1948, 872 and 461 respectively. Marangoni number much larger than 1 represents the dominance of thermal transport due to gradient in surface tension over that of thermal diffusion. In all cases, energy dissipated at the interface is sufficient to drive temperature-based Marangoni flow.

The flow speed observed in this study is much slower compared with those reported by Shimizu [71] and Thagard [69]. This can be attributed to two major differences in terms of discharge geometries and conditions. Shimizu reported using a 7.5 kV pulse with a repetition rate of 5 kHz, over water with low conductivity (1.3 μS/cm), where Thagard reported using a 25 kV pulse with a repetition rate of 60 Hz, over water with high conductivity (1.042 mS/cm). In addition, while the positively biased electrodes were placed above the

liquid layer in both cases, the ground plate was placed under the glass container with the liquid for Shimizu's case, and submerged in the liquid for Thagard's case. The gas used in the head space differed as well, which was ambient air for Shimizu's study, and argon for Thagard's study. The resulting morphology and maximum values of the flow fields measured, as a result, showed great variation. Shimizu reported the observation of a high velocity region at the center with an upward direction towards the contact point between the plasma discharge and the water surface, with a maximum velocity of 2.5-3 cm/s. Thagard observed strong surface flow first traveling inward to the central line from t = 0 to 5 second, but the fluid flow reversed direction from t = 5 s onward, and reported a representative velocity of 0.29 cm/s.

Due to the temperature dependence of Marangoni effects, higher flow speeds can be correlated to increased thermal effects, which is a function of gas type, liquid conductivity, relative permittivity of the discharge gap, pulse voltage and the pulse repetition rate.

The low repetition pulse rate used in this study, 10 Hz, is smaller than those reported by Shimizu (5 kHz) and Thagard (60 Hz). A small repetition pulse rate reduced the power deposited into the liquid layer, thus reducing the associated thermal effects and Marangoni stress. The maximum velocity measured in the high conductivity case is approximately 0.7 mm/s, which is approximately 4 times smaller than that reported by Thagard. This is consistent with the 6 times reduction in repetition frequency used in our study, accounting

for other variables. On the other hand, the maximum velocity measured in the low conductivity case is approximately 0.15 mm/s, and is 200 times smaller than that reported by Thagard, but the repetition frequency used in our study is 500 times smaller. While there are other mitigating factors involved, the observed maximum velocities agree well with those reported by Shimizu and Thagard.

The variation in liquid conductivities appeared to be consistent with our observations as well. Shimizu reported maximum flow direction perpendicular to the interface, pointing towards the discharge region in the water with low conductivity, where Thagard reported maximum surface flow along the interface, pointing away from the discharge region in the water with high conductivity. This suggested correlation between flow direction and liquid conductivity. This relationship was observed in this study as well. Fluid flow appeared to direct towards the discharge region at low conductivity, but travels away from the discharge along the surface at high conductivity. This can be readily explained as an effect due to difference in charge relaxation time. Conductivity κ is inversely proportional to charge relaxation time ($\tau = \frac{\varepsilon}{\kappa}$).

At high conductivity, charges deposited by the plasmas were able to disperse quickly and sustain a high current column, this is representative of the observations made by Thagard. Combining the submerged electrode and the high conductivity of water, plasmas coming into contact with the liquid surface were able to sustain a consistent current drop, and

likely gave rise to a direct current path in the liquid layer as well that bridged the plasmas in contact with the water surface to the submerged electrode. This led to increased joule heating through the central line of the reactor, thus resulting in a radial temperature gradient, where the central line area in the liquid is hotter than that near the edge of the reactor and led to the development of surface flow.

Contrarily, at low conductivity, charges deposited by the plasmas cannot move away quickly and are accumulated near the surface, which is representative of the observed made by Shimizu. With the ground electrode placed outside the glass container with low conductivity water, plasma discharges traveled as an ionization wave on the water surface instead, depositing charges on the water surface. This can result in a high velocity gas flow which drives the circulating flow away from the surface and upward towards the plasma discharge in the central line.

Due to the circular nature of the air bubble, the dependence of flow directions on fluid conductivity is not as straightforward. At high conductivity, more surface hugging streamers developed, which led to increase heating on the surface of the bubble. However, the streamers initiated at the anode did not touch on the other end of the bubble. Thus we can speculate that the temperature gradient is both radial (from the anode) and linear, where there is increased heating in the regions near the bubble surface and the anode. This results in a cold region at the opposite end of the bubble from the anode, thus led to intense

fluid flow on the surface of the bubble traveling away from the anode. At low conductivity, only localized corona discharge was observed. However, since the discharge gas is contained inside a bubble, a gas flow could not develop. Thus fluid flowed from the hotter region, near the anode, towards the edge of the recess area as a result of temperature dependent Marangoni stress. High speed flow was observed on the bubble surface traveling towards the anode, and can be attributed to compressed return flow due to the curved bubble surface.

Chapter 10

Applications

The applications of low temperature atmospheric pressure plasmas are well documented in various research fields, such as plasma medicine [128, 129, 130] and water purification [61, 117]. In this chapter, we report the use of plasmas to remove cyanotoxin from lake water, and the investigation of plasma interference on chemical oxygen demand (COD) tests.

10.1 Removal of cyanotoxin from lake water

Cyanobacteria (blue green algae)-derived algal blooms have risen in public attention in recent years owing to its harmful effects on humans and animals [131]. These blooms occur under favorable conditions of temperature (typically summer), light and where there is an abundance of nutrients such as nitrates and phosphorous. The abundance of nutrients

is often anthropogenic in nature, typically associated agriculture runoff into source water bodies [132]. Under conditions that are still not well-understood, the cyanobacteria will release toxins into the water naturally. The release of toxins can also occur when algal cells are damaged. While, the cyanobacteria produces a range of toxins, the one of chief concern is hepatotoxin microcystin-LR [133, 134, 135]. Here the L and the R represent the variable amino acid groups leucine and arginine, respectively. This large molecule (MW 995.2) (Cayman Chemical) is a hepatotoxin that can cause human and animal disease ranging from liver damage to tumor promotion. Indeed, the introduction of this toxin into source water during an algal bloom in Brazil in 1996 is believed to the source of 51 deaths of patients at a dialysis facility [136]. The National Cancer Actually nominated blue-green algae supplements for study by the National Toxicology program because of concerns regarding the potential carcinogenicity of microcystin-LR [137]. Ordinarily, this toxin biodegrades over time. Some studies however suggest that the degradation occurs naturally over a period of days up to a week, however if left in the dark (sediments of water source) it can persist for years [132]. Also problematic is the bioaccumulation of the microcystin toxin in fish and shell fish. The cyanobacterial proliferation under algal bloom conditions also affects overall water appearance and can lead to dead zones in the source water owing to reduction in oxygen concentration in water associated with decaying algae.

The presence of microystin in source drinking water is problematic for conventional wa-

ter treatment methods. Indeed, the persistence of algal blooms in the Lake Erie Region and in the state of Ohio has even led to drinking water advisories and in cases an outright drinking water ban [138]. The World Health Organization, shortly after the microcystin-derived illnesses and deaths in Brazil, put forth a maximum concentration limit for microcystin of 1 microgram/L [133]. Currently, the US EPA has not established a maximum concentration level for microcystin. In this regard, the substance is unregulated. The U.S. EPA has however placed the substance on its Contaminant Candidate List [139]. On the other hand states can set self-imposed threshold standards for action. The State of Ohio has established that greater than 20 micrograms/L as the no drinking and no contact recreation threshold.

Conventional water treatment methods involve coagulation, flocculation, and filtering followed typically by chlorination. Mechanical processing of fragile cyanobacteria can lead to cell membrane damage (lysis) leading to the release of the toxins, which compounds the removal problem [132, 138]. While chlorination can be an effective means of decomposing microcystin, microcystin-derived disinfection byproducts which form in the process are themselves a toxicity problem [140]. In general, granular activated charcoal/carbon (GAC) has shown great promise in the removal of microcystin [141, 142, 143]. The use of GAC however requires careful management and backwashing to flush out accumulated contaminants. Additionally, it has been shown that GAC loses effectiveness in the presence of chlorine and heavy natural organic matter concentrations, which compete for absorption sites [131].

It has also been shown that bioremediation may also be effective in the removal of microcystin [132, 144]. One attractive attribute borne out of bioremediation studies is the absence of cytotoxic byproducts after treatment [132]. On the other hand, the long treatment times may preclude this approach from practical implementation. Interestingly, it has been shown that GAC microcystin-LR removal may actually be assisted by the presence of a bioremediating layer on the carbon particle surface [145].

In recent times, there has been a great deal of interest in advanced oxidation methods as a means to remove organic toxins in water via a process known as mineralization [146, 147, 49, 148]. Here the toxins are reduced to carbon dioxide, water and inorganic salts via multiple reactions with hydroxyl radicals produced in solution. Advanced oxidation cannot only be used against those recalcitrant organics beyond the range of conventional or bioremediation methods, but in general it is not known to produce toxic intermediates. Advanced oxidation has been investigated as a means of addressing the microcystin toxin [149, 150]. Decomposition mechanisms via hydroxyl radicals has been studied using pulsed radiolysis. In that work, it was found that addition to the microcystin benzene ring and abstraction of aliphatic hydrogen are two key mechanisms that destroy the biological activity of the substance [151].

Ozone, another advanced oxidation species, has shown great effectiveness at decomposing microcystin. Disinfection byproducts however are a concern for ozone-based methods.

The use of UV with titanium oxide has also shown great promise microcystin degradation without the production of disinfection byproducts. Scale up of this method however has not been demonstrated in regards to actual implementation in a pilot plant [142]. In general, it should be pointed out from a practical standpoint, advanced methods would likely be implemented with filtration processes as well. Here the filtration stage would remove the algal bloom cells and naturally occurring organics. Those cells that are damaged in the initial coagulation and filtering stage would invariably introduce microcystin into solution in addition to that which is already in solution. Advanced methods could be introduced as an additional stage to specifically address the microcystin.

In recent years, interest in using non-equilibrium, atmospheric pressure plasmas as a means for degradation of organics in solution has received a great deal of attention. Plasmas in contact with water produce hydroxyl radicals directly via mechanisms such as dissociative attachment, direct bombardment, or the production and subsequent decomposition of hydrogen peroxide. Hydroxyl radical itself is highly reactive particularly with organic compounds (contaminants) and thus has a very short lifetime. The presence of peroxide and ozone serve as additional sources in the production the hydroxyl radical. Equations prevailing in the hydroxyl production cycle may be summarized as:

$$e^- + H_2O \longrightarrow OH^\bullet + H^\bullet + e^-$$

$$OH^\bullet + OH^\bullet \longrightarrow H_2O_2$$

$H_2O_2 + UV \longrightarrow 2\,OH^{\bullet}$

$H_2O_2 + e^-_{(aq)} \longrightarrow OH^- + OH^{\bullet}$

$OH^{\bullet} + H_2O_2 \longrightarrow H_2O + HO_2^{\bullet}$

$HO_2 \cdot + H_2O_2 \longrightarrow O_2 + H_2O + OH^{\bullet}$

And via ozone produced in the plasma: $O_3 + UV \longrightarrow O_2 + O(^1D)$

$O(^1D) + H_2O \longrightarrow 2\,OH^{\bullet}$

Plasma production in bubbles in water can also produce ozone as well as air is used as the working gas. These plasmas introduce UV light into solution as well. Altogether, these advanced oxidation mechanism, which all occur simultaneously, can be brought bear on the decomposition of microcystin in solution. Work aimed at microcystin destruction in a glow discharge has been reported [152]. In that work, small volume microcystin solutions were treated by an electrolytic glow discharge apparatus. In the work reported here, we utilize a nanosecond pulse driven underwater plasma jet with air as the feed gas to decompose samples of microcystin-LR solution [153]. With the plasma jet, plasma generated reactants are directly injected into solution without diffusion losses or sensitivity to liquid surface layer conditions. Additionally, electrolytic processes and particle formation at the electrode, as what would occur in glow discharge configurations is avoided. The time-resolved degradation of the microcystin was tracked using enzyme-linked immunosorbent assay (ELISA) test kit and high-pressure liquid chromatography-mass spectrometry. To access the chem-

istry behind the observed degradation, the production rate of hydrogen peroxide, a key advanced oxidation agent, is tracked as a function of time using a Hach hydrogen peroxide test kit. Decomposition products are also tracked as a function of time using high-pressure liquid chromatography-mass spectrometry. Additionally, the prospect of scale-up of this apparatus for a future piloting test is commented upon.

10.1.1 Methods

10.1.1.1 Preparation of samples

Microcystin-LR (MC-LR) used in this investigation was purchased from Cayman Chemical, USA (Item 10007188), with 100 μg compound suspended in 20μL ethanol. The chemical structure of MC-LR is shown in Fig. 10.1 [154]. As can be seen in the figure, the molecule consists of seven-member peptide ring.

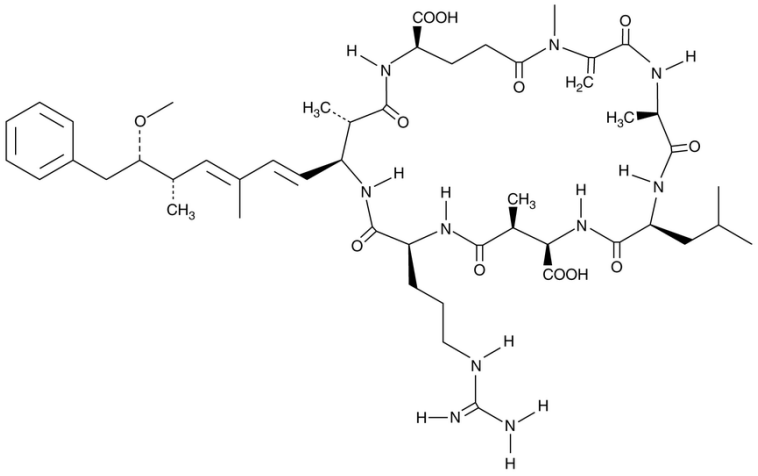

Figure 10.1: Chemical structure of MC-LR purchased.

A small amount of MC-LR in ethanol was dissolved in 500mL of ultra-pure type-1 water, obtained from a Milli-Q system (Millipore Corporation, USA). This initial sample concentration was found to be 26.658 ng/mL, using an ELISA MC-LR test kit testing samples diluted 10 fold. The ELISA test is currently an accepted method of detecting microcystin in water at water treatment plants. In the test, microcystin in solution binds with a known concentration of antigens in the wells of a microtiter plate. The microcystin competes for binding with a microcystin-analogue protein bound to the walls of the wells. After this process step, the sample is washed. The wall bound antigens are then functionalized and detected optically. In this manner, the concentration of the microcystin is detected indirectly. In this work, approximately 20 mL of sample is distributed into each amber glass vials for testing. Amber glass vials are used to preserve the MC-LR from light driven decomposition.

10.1.1.2 Experimental set-up

Microcystin samples were treated with the underwater dielectric barrier discharge (DBD) plasma jet, shown in Fig. 10.2. Stripped 16 AWG high voltage wire was threaded through dielectric (glass) tube with inner diameter of 4.06 mm and acted as the high voltage electrode. A coiled wire wrapped around the tip of the glass tube acted as the ground electrode. A tee connector was connected to the end of the glass tube to allow for gas injection into the tube to form bubbles near the opening of the submerged tube. Application of high voltage

to the central electrode produces streamer plasma in the bubbles. An external mechanical pump was used to supply air at a flow of approximately 1.4 L/min. The device was powered using a high voltage nanosecond pulsed power modulator (FID GmbH, FPG 10-10KM) capable of providing positive voltage pulses of up to 15 kV at a repetition rate as high as 10 kHz. For these tests, peak voltage was 13.3 kV at a repetition rate of 5.13 kHz. In this work, the DBD plasma jet apparatus was operated in a 40-mL amber glass vial containing the microcystin sample.

Samples are treated for various time intervals, ranging from 30 seconds to 30 minutes. Though boiling will not destroy microcystin, the treatment vial was placed in a water bath to stabilize process temperature and to prevent evaporation.

Concentrations of remaining MC-LR were then measured using an ELISA kit. As previously mentioned, the ELISA kit works via competitive binding with the target molecule, and quantification of samples concentration via spectrophotometry is compared with measurements of standards with known concentrations. Therefore, if concentration of target compound in samples exceeds that of the most concentrated standard, the response will only be qualitative. Similarly, near the limit of response elicited by the negative standard, which contains no microcystin but is used to account for fluctuations in spectrophotometry measurements, the response can only be qualitative.

Given the long lifetime of hydrogen peroxide, its concentration was measured as a func-

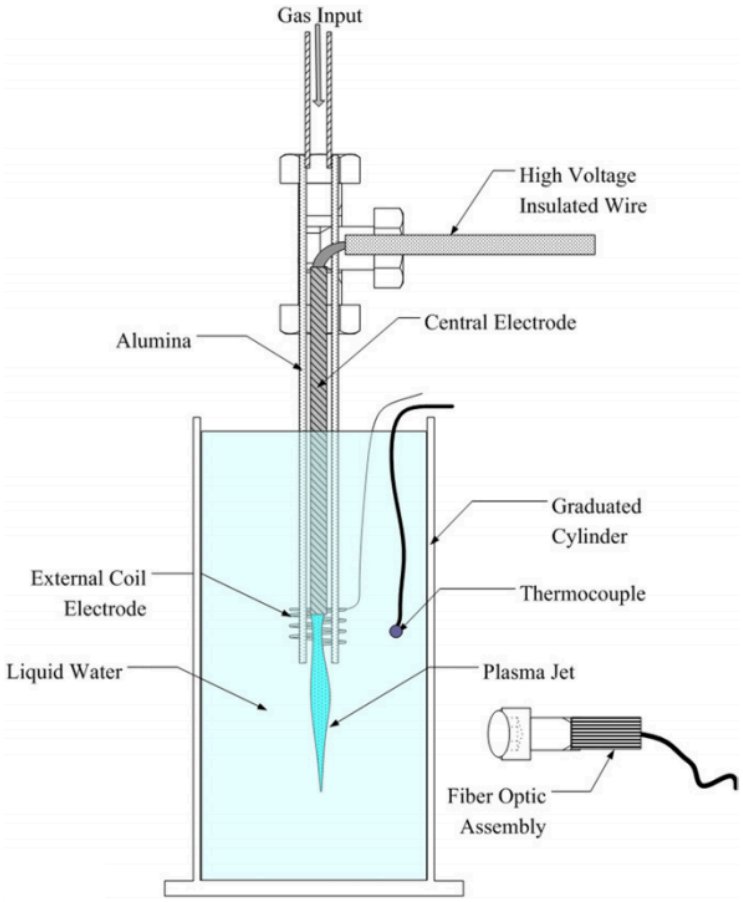

Figure 10.2: Experimental set-up

tion of time as an indicator of the presence of oxidative species that drive decomposition of organic compounds in water. Hydrogen peroxide concentration was measured using a titration test kit manufactured by Hach (model HYP-1, cat. No. 22917-00). The concentration of hydrogen peroxide was detected by dissolving ammonium molybdate (a catalyst) and sulfite 1 reagent powder in the test solution and titrating it against sodium thiosulfate. Sulfite 1 reagent powder contains a known amount of iodide and starch. On contact with hydrogen

peroxide in solution, iodide reduces hydrogen peroxide to produce iodine and water; the iodine is then trapped within the starch molecule to form a complex that appears dark blue when dissolved in water. Sodium thiosulfate can titrate iodine, thus the amount of sodium thiosulfate that is used to extract all the iodine trapped can be used to infer the amount of hydrogen peroxide in the solution.

Fragments of microcystin-LR post-treatment were analyzed using TOF/Q-TOF Mass Spectrometer made by Agilent Technologies by Department of Chemistry at University of Michigan. An Agilent Zorbax Eclipse Plus C-18 column (2.1mm x 50 mm x 1.8 micron) was used, where solvent A is water with 0.1% formic acid and solvent B is 95% acetonitrile with 5% water with 0.1% formic acid. The spectrometer was run in the 2 GHz extended dynamic range mode with low mass range, which is M/Z from 50 to 1700. During each run, 20 μL of sample was injected with flow rate at 0.4 mL/min; where the sample stayed at 95% of solvent A and 5% of solvent B for 2 minutes and slowly increased in gradient to 100% acetonitrile from 2 to 15 minutes.

10.1.2 Results and discussion

10.1.2.1 Quantification of MC-LR reduction using the ELISA test

The concentration of MC-LR remaining in solution as a function of plasma treatment time for two experiments is shown in Fig. 10.3. As noted, red lines are placed on the plot to

indicate the sensitivity boundaries of the method. Only qualitative trends can be inferred outside these boundary lines.

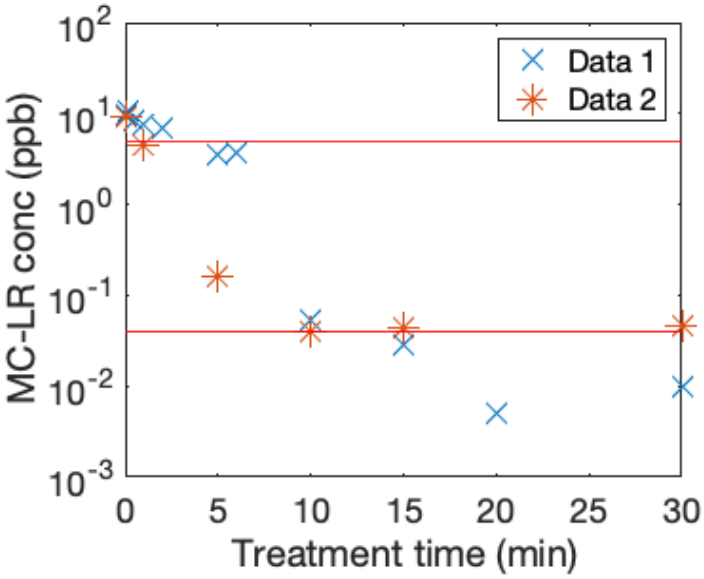

Figure 10.3: Concentration of remaining MC-LR in samples treated with plasma for various times.

Data set 2 was obtained with peak voltage of 13.3kV with a repetition rate of 5.13kHz, where the parameters in data set 1 were at approximate levels but were not obtained quantitatively.

For those samples with remaining concentration of MC-LR within the acceptable range, the percentage removal of MC-LR is calculated. In both data sets, the removal percentage was greater than 99 percent after 10 minutes of testing. The variability shown in the data after the 5 minute is possibly due to the lower peak voltage and repetition rate for data set 1, resulting in lower energy deposition, thus lower percentage removal.

Such high percentage removal rates are attributed to the active groups' susceptibility to ozone, UV rays and hydroxyl radicals produced in the discharge. Previous research has shown that advanced oxidation methods can be effective at the removal of microcystin. In particular, UV-peroxide and ozone-peroxide combinations give rise to rapid decomposition.

The actual degradation mechanism is believed to be multi-stage, at least under conditions that prevail when the plasma is active; discussed here in [155] where UV, ozone, and hydroxyl radicals are all present. It has been shown that under such conditions generated conventionally (non-plasma), UV light gives rise to geometrical isomerization of the toxin and in particular disrupting the biologically active portion of the molecule. Hydroxyl radicals then further attacks and destroys the molecular structure [156].

Joule heating of the water remains a major mechanism of energy loss in this apparatus, which results in the long treatment time, in the order of minutes, to achieve removal rate of over 99% in our samples. Shorter pulse width and rise time of high voltage power supplies can mitigate some heating effects. Combining plasma treatment with biological methods of organic decontamination can also be promising due to potential synergistic effects between bacteria and plasma-based reactive species, this is left to future work.

10.1.2.2 Production of hydrogen peroxide

Photolysis and direct electron impact of the more stable hydrogen peroxide molecule as previously stated leads to the production of more OH. OH attacks organics via processes such as hydrogen abstraction which gives rise to the formation of organic peroxides. Its presence is therefore an indicator of advanced oxidation of the microcystin. The production rate of hydrogen peroxide during discharge operation was therefore assessed. To access hydrogen peroxide production, ultra-pure type-1 water was treated using the same discharge cell. Using a Hach hydrogen peroxide test kit, samples diluted to 10 to 30 folds were tested. Samples were diluted because the test kit has a test range of 1-10mg/L, and the sample concentrations exceeded the possible maximum concentration detectable. Multiple dilution ratios were used to calculate the extrapolated concentration to minimize error.

For samples treated for 1 minute, with 2:1 and 5:1 dilutions, concentrations of hydrogen peroxide were averaged to be 190.5 mg/L with a standard deviation of 10.6 mg/L. For samples treated for 5 minutes, with one 14:1 and two 29:1 dilutions, concentrations of hydrogen peroxide were averaged to be 566.7 mg/L with a standard deviation of 106.9 mg/L. The magnitude of hydrogen peroxide production is of similar magnitude of that reported previously [2].

The sharp increase in concentration of hydrogen peroxide correlates directly with the production of OH radicals, which are highly reactive and can attack various active groups

in the MC-LR compound. The presence of the peroxide is a clear indicator of the presence of a necessary precursor to a number of advanced oxidations processes. A model for the degradation pathways is somewhat complicated in that a number of advanced oxidation processes are likely active during treatment. Additionally, the presence of decomposition intermediates further complicates analysis. Such a model is left to future work.

10.1.2.3 High-pressure liquid chromatography-mass spectrometry

High-pressure liquid chromatography-mass spectrometry was used to gain some insight into decomposition pathways. A sample of ultra pure type-1 water was used to establish a baseline of species existed in the system and sample solvent. Untreated sample was found to contain microcystin-LR (M/Z 995.2), as shown in Fig. 10.4, whereas its level was undetected in any of the treated samples. One of which, sample treated for 30 seconds, is shown in Fig. 10.5 at similar acquisition time for comparison, no microcystin-LR was detected but some fragments and complex were observed in low levels. Fragments of M/Z in the proximity of 457 and 485 were detected in most of the treated samples in low levels. With low concentrations of microcystin in the starting samples, it is difficult to infer much more owing to the resulting low concentration of the intermediates in the treated sample. However, the presence of intermediates and complexes can likely lead to the production of disinfection byproducts. Future work is required to characterize these fragments to access their toxicity in order to avoid extra environmental burden.

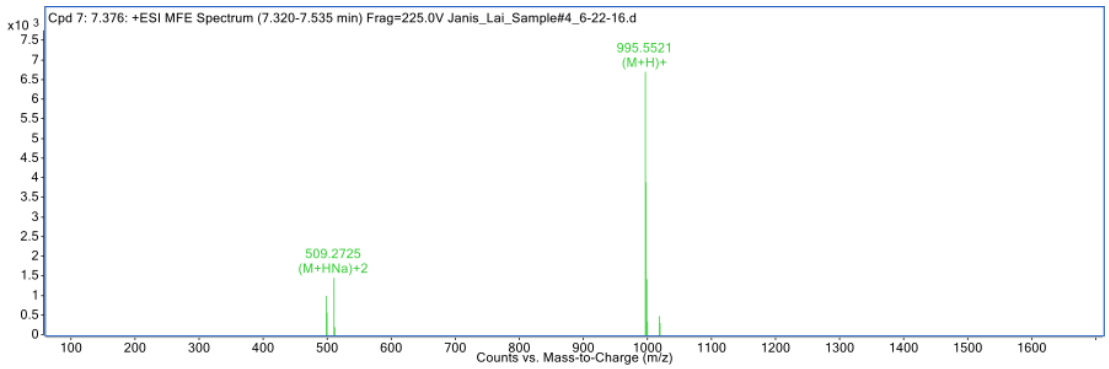

Figure 10.4: Mass spectrometry of untreated microcystin sample, at acquisition time from 7.320-7.535 min.

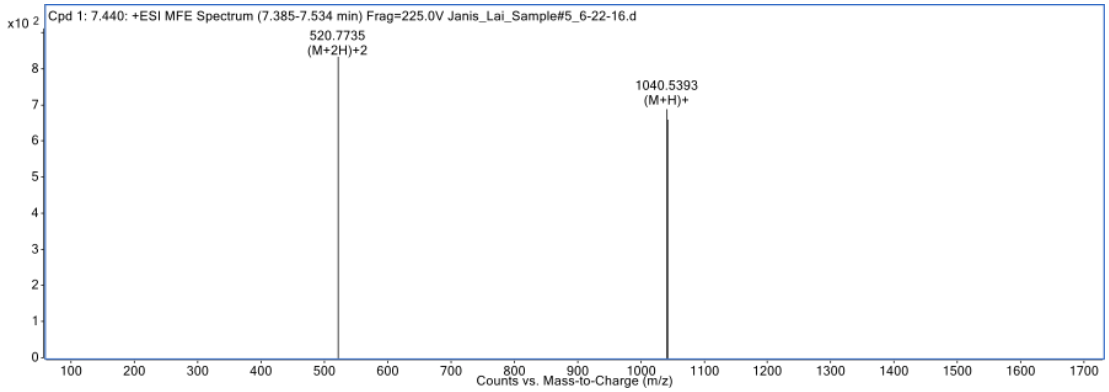

Figure 10.5: Mass spectrometry of microcystin sample, treated for 10 seconds, at acquisition time from 7.385-7.534 min.

10.2 Validity of COD tests on plasma-treated water

Chemical oxygen demand (COD) is a common benchmark test used in wastewater treatment industry to measure the amount of organic matter in samples. The amount of organics is inferred from the amount of oxygen consumed in the test between the sample and the reagent. Potassium dichromate oxidizes the organics in the water, which leads to a yellow-to-green color change observed in the process (shown in Fig. 10.6). This color change is

measured using a photometer. This test is effective in quantifying the amount of oxidizable pollutants found in wastewater.

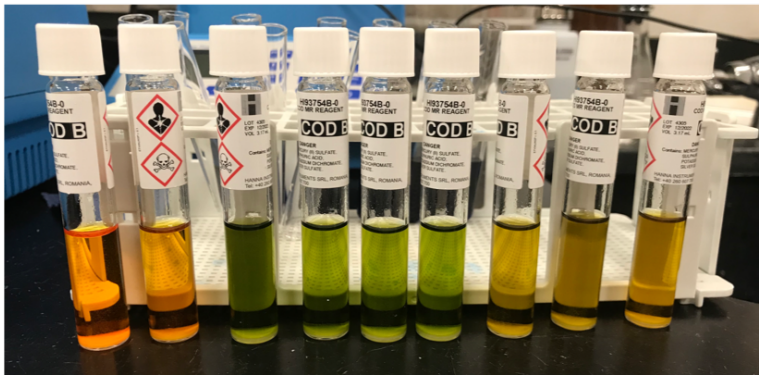

Figure 10.6: COD test vials reacting with samples, showing spectrum of colors.

Presence of oxidative species such as hydrogen peroxide is known to interfere with the test and results in an overestimated COD value [157]. Plasma in contact with water can initiate advanced oxidation processes that removes organic materials via oxidation with reactive species such as hydroxyl radicals, ozone, hydrogen peroxide and UV light. As plasma-based water purification methods are being developed for water and drinking water treatment, the validity of COD tests on such samples must be established. In this experiment, COD tests were performed on water with varying chemical loads of dyestuffs to investigate the effects of plasma treatment on COD measurements.

10.2.1 Methods

10.2.1.1 Pollutant analog

Methylene blue is a chemical commonly used as a dye and a medication. Its molecular formula is $C_{16}H_{18}N_3SCl$ and it has a molecular weight of 319.85 g/mol. Having a peak absorbance at 664 nm, the concentration of dissolved methylene blue in water can be measured using spectrophotometry.

The digestion process of methylene blue during COD test can be seen as

$$4\,C_{16}H_{18}N_3SCl + 73\,O_2 \longrightarrow 64\,CO_2 + 18\,H_2O + 12\,NH_3 + \text{residues}$$

That is, 73 moles of oxygen is required to oxidize 4 moles of methylene blue. This translate to 1.825 mg/L of oxygen is required to oxidize 1 mg/L of methylene blue.

Methyl red is a chemical commonly used for pH indication and chemical detection. Its molecular formula is $C_{15}H_{15}N_3O_2$, it has a molecular weight of 269.3 g/mol and peak absorbance at 410 nm.

The digestion process of methyl red during COD test can be seen as

$$2\,C_{15}H_{15}N_3O_2 + 31\,O_2 \longrightarrow 30\,CO_2 + 6\,H_2O + 6\,NH_3$$

That is, 31 moles of oxygen is required to oxidize 2 moles of methyl red. That translates to 1.841 mg/L of oxygen is required to oxidize 1 mg/L of methyl red.

10.2.1.2 Experimental set-up

The plasma jet described in Sec. 10.1.1.2. In this study, ambient air was used, and flow rates were set at either 100 or 500 sccm. The plasma jet is connected to a nanosecond pulsed power supply (FID, Gmbh). Two voltage and frequency settings were used: 1) 10 kV, 2.25 kHz, denoted as the low setting, and 2) 13 kV, 10 kHz, denoted as the high setting. Waveform of the high setting is shown in Fig. 10.7.

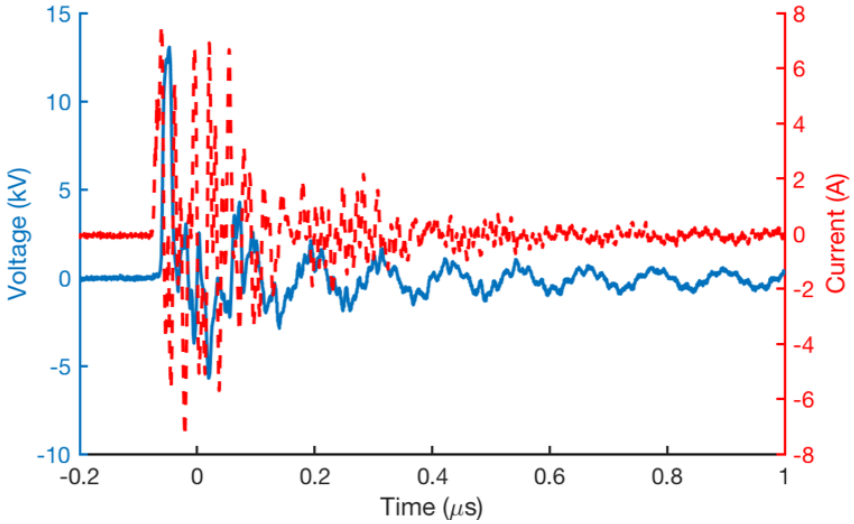

Figure 10.7: Waveform of the high voltage/frequency setting.

Hanna Instrument's COD medium range reagent vials in combination with Hanna Instrument's multi-parameter wastewater & water photometer with COD and pH meter were used to measure COD values of samples. Solutions were diluted 1 to 10 fold before testing to ensure the measurements were not out of range.

Shimadzu UV-1601 UV-Vis spectrophotometer was used to measure the concentrations of methylene blue and methyl red in water. Solutions are diluted 300-1000 fold before testing.

10.2.2 Degradation of methylene blue

At low voltage and frequency setting, the discharge was localized inside the glass tube of the plasma jet hence did not come into direct contact with the liquid. The time-resolved COD and spectrophotometry measurements for the case of low settings are both shown in Fig. 10.8. Both measurements showed linear reduction of concentration of methylene

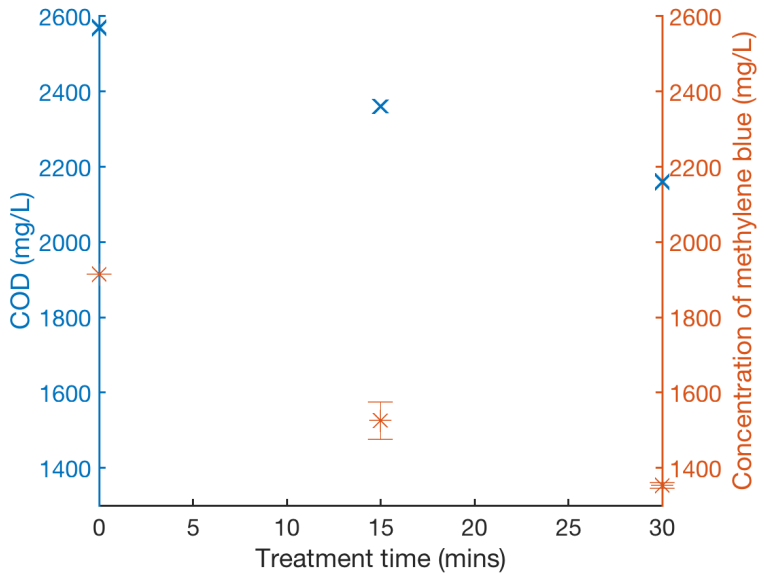

Figure 10.8: COD and spectrophotometry measurement of concentration of methylene blue at low setting.

blue as a function of time. Localized discharge relies heavily on diffusion of gas phase reac-

tive species into the bulk liquid for decomposition. Lack of contact between the discharge and the liquid surface led to less in-situ production of reactive species at the bubble liquid interface. Thus interference from oxidative species such as peroxide is limited.

At high voltage, intense streamers were observed in the bubble attached to the end of the plasma jet. The time-resolved COD and spectrophotometry measurements for the case of high settings are both shown in Fig. 10.9. While concentration of methylene blue mea-

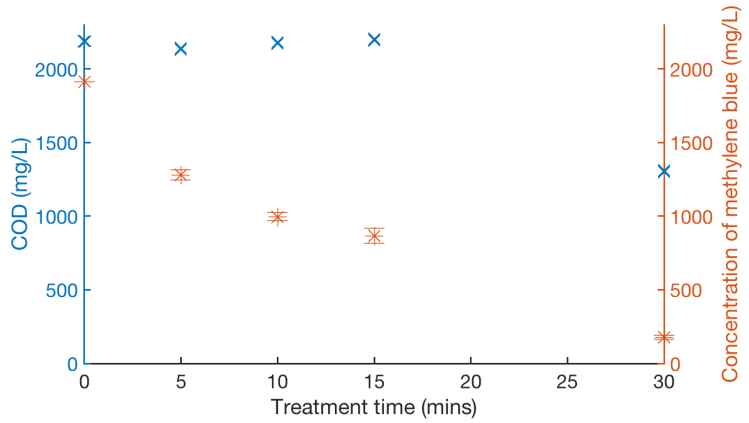

Figure 10.9: COD and spectrophotometry measurement of concentration of methylene blue at high setting.

sured via spectrophotometry showed steady decline in time, COD value remained high in treatment times up to 15 minutes, and showed a steep decline with treatment time of 30 minutes. The discrepancy between reduction trends in both measurements can be attributed to two effects. Presence of plasma discharges coming in contact with bubble liquid interface can lead to in-situ production of oxidative species at the plasma-liquid interface. Thus high concentration of oxidative species can interfere with COD values, overestimat-

ing the amount of organic matter measured. Additionally, presence of decomposition fragments from methylene blue can cause the increase of COD value while spectrophotometry showed that methylene blue was being decomposed.

In future work, appropriate measures used to quench hydrogen peroxide and other oxidative species can help quantify the interference effect.

10.2.3 Degradation of methyl red

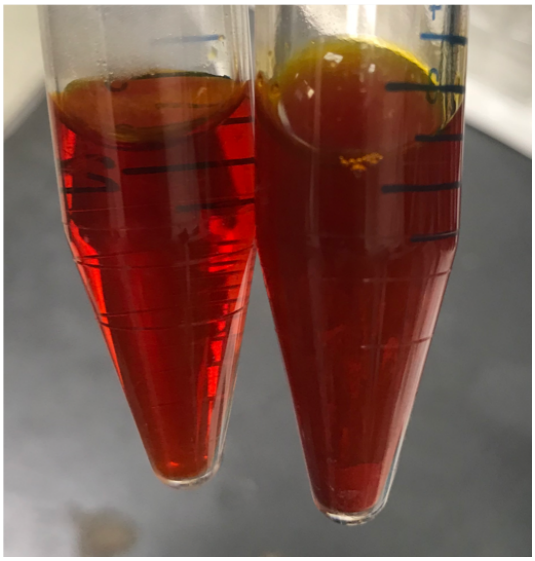

Figure 10.10: Untreated (left) and plasma-treated (right) methyl red solutions.

High voltage and frequency setting was used to treat solutions with dissolved methyl red. While untreated solutions remain clear, turbidity was observed in treated solutions, shown in Fig. 10.10. This turbidity can result from precipitation of methyl red from solution due to plasma treatment. 5-minute plasma treatment of methyl red solutions yielded

a 23% reduction of COD value from 6,360 mg/L to 4,890 mg/L, and a 37% reduction of spectrophotometry measurement from 4000 mg/L to 2494 $\pm$ 98 mg/L. In particular, the presence of precipitation processes in plasma treatment of methyl red indicated that degradation pathways of methyl red and methylene blue are different.

In future work, advanced chemical analytical techniques such as liquid chromatography can be used to corroborate the presence of disinfection fragments and further understand the degradation pathways of methyl red and methylene blue.

Chapter 11

Conclusions

11.1 Research summary

The goal of this dissertation was to investigate the associated chemistry and physics at the plasma-liquid interface between a gas bubble and its surrounding liquid region using a 2-D analogous apparatus. Rising demand in the development of plasma-based water purification methods requires thorough understanding of plasma-driven processes at the plasma-liquid interface. Discharges in bubbles are of interest because of the potential to maximize the plasma-liquid interface and reduce the voltage required for breakdown, thus are considered to be an energy efficient method of transporting reactivity from plasma to liquid phase. However, bubbles in liquids do not lend itself well to diagnostics due to the interference effects from surrounding liquid. The first part of this dissertation, therefore, was to describe the development and implementation of a 2-D discharge cell. In this cell, two clear

plates were used to contain a thin layer of liquid, where a single trapped bubble was injected using a precision syringe. Nanosecond pulsed power supply was connected to the injection syringe and was used to excite plasma discharges in the bubble. In this geometry, the liquid, plasma and interface regions are available for simultaneous optical interrogation.

Chemical probes, such as methyl orange and potassium iodide-starch solutions, were used in early experiments to study the production and transport of plasma-derived chemistry in the bulk liquid. Results suggested that discharge excitation mode can impact the transport of reactivity from the plasma into the bulk, with smooth diffusion occurring for microdischarges and large-scale circulation playing a key role in transport for streamer discharges. Optical emission spectra of the visible plasma region revealed the consumption of nitrogen over time, suggesting compositional changes in the bubble. Next, we altered the gas type in the bubble from air to argon, and observed similar traveling oxidation and acidic fronts in the bulk liquid. This indicated that in the absence of nitrogen and oxygen, electron impact ionization and ion charge exchange processes at the interface likely contribute significant amount of acidity and reactive species at the interface. Indigo trisulfonate solutions were used in combination with absorption spectrophotometry to visualize and quantify the production and transport of oxidative species, primarily ozone and hydroxyl radicals, into the liquid layer. Calibrated measurement showed the amount of indigo dye consumed to be in the order of several hundreds micro-mole per liter (μM) in regions sur-

rounding the bubble. The transport of reactive species in liquid was enhanced by the fluid flow initiated by streamers in contact with the interface.

Next, optical diagnostics methods, shadowgraph and particle image velocimetry (PIV), were used to study the observed fluid effects near the bubble. PIV results showed sharp velocity shear in regions with thickness of 1.5 mm surrounding the bubble; such velocity shear is often an indicator of the presence of Kelvin-Helmholtz (KH) perturbation. Analysis of the instability showed that it was stable. Interfacial perturbations create vortices in the shearing layers, which may be the origin of the mechanism that transports the plasma-derived reactive species further into the bulk liquid when streamers are present. Shadowgraph measurements showed that a clear density gradient was initiated by the plasma in the bulk liquid, and showed that the interface is indeed active and compresses the liquid outward. More importantly, it indicated the presence of the active boundary layer, which apparently is a lower density region local to the interface, at least in the presence of streamers.

We also observed the mechanical perturbation of the interface in one of the spectrophotometry measurements. Nanosecond pulsed plasma streamers in bubbles were observed to not only perturb the interface, but eventually drive the development of capillary waves that propagate along the interface. The capillary waves appear to be driven by plasma discharges, damped by viscosity and restored by surface tension. For the 2-D geometry, we

found that the capillary wave mode n, defined by the amount of points on the resulting star polygon, is dependent on both bubble diameter and plasma excitation frequency. Additionally, resonant capillary waves can be observed in adjacent bubbles, which indicates that capillary waves on the interface can give rise to acoustic oscillations and drive large-scale fluid effects in the bulk liquid. Interestingly, the formation of capillary waves also leads to self-organization of subsequent streamer strikes, likely due to the perturbed interface altering the electric field in the bubble. This selective contact further sustains the capillary waves. Thus this observed coupling between self-organization of plasma streamers and interfacial capillary waves appears synergistic, and provides insight into a controllable approach to maximizing the plasma liquid contact area, a key consideration for plasma liquid technologies such as water purification and plasma medicine.

Lastly, an investigation was performed to study the effects of bulk liquid conditions on discharge morphology in the bubble and plasma-driven fluid flow in the bulk liquid. Refraction of electric field lines at the gas-liquid interface can enhance the local electric field, and promote propagation of streamers along the interface. Fast ICCD imaging showed that the liquid conductivity of the solution has significant impact on the propagation of discharges in bubbles. This effect is attributed to both variation in relaxation time and the presence of charge carriers with varying conductivity. High electrical liquid conductivity allows charges to disperse quickly. As a result, interfacial streamers stall out axial stream-

ers. In liquids of lower conductivity, effects of surface charge become dominant, and halt propagation of streamers in the bubble.

Energy dissipated per pulse also scales positively with increasing liquid conductivity due to increased current and gas heating. Increased thermal effects at the interface can give rise to a local temperature thus surface tension gradient in the liquid region, which drives Marangoni flow. Plasma-driven fluid flow was measured using PIV. At high conductivity, intense surface flow was observed which later developed into a large-scale vortex in the bulk liquid, with maximum velocity reaching up to 0.7 mm/s. At low conductivity, maximum velocity was observed to be localized on the bubble surface, at approximately 0.15 mm/s, but traveled in the opposite direction.

Comparison with available literature found that flow velocity depends on liquid conductivity, plasma pulse frequency, gas type, relative permittivity of the discharge gap, pulse voltage and pulse width. Positive correlation between observed flow velocities and liquid conductivity suggests that increased thermal effects can drive higher observed flow speeds, and points to the possibility of high contribution of Marangoni effects in plasma-driven fluid flow.

From a practical standpoint, the findings are interesting. In order to implement water treatment reactors using plasma in bubbles, the water quality has to be considered due to its impact on resulting plasma and liquid characteristics, such as reaction rates of reactive

species produced and rates of mixing. While water with relatively high electric conductivity may produce more reactive species and drives high induced flow speeds, one can expect more energy dissipation in this case as well thus it will be less energy efficient.

Surface water, a source of drinking water, tends to have higher conductivity than that of deionized water due to presence of minerals and organic compounds. To minimize power consumption and associated thermal effects while generating reactive species, one may need to use shorter excitation pulses for plasma production. In this case, shorter pulse width and rise time can minimize the development of surface hugging streamers, which is a major charge dissipation mechanism. However, this will result in reduced plasma-induced flow and thus fluid mixing, and can lead to dead zones in treatment volume. These attributes must be carefully considered in designing a plasma-based reactor for water treatment. While research has shown that plasma is effective against various contaminants resistant against conventional treatment methods, there is an increasing need to focus future research efforts on designing efficient high throughput reactors capable of processing sufficiently large volumes of water for municipalities and industries.

Diagnostics methods discussed in this dissertation have minimum response time in the order of microseconds, thus are inadequate to study the production of ultraviolet (UV) and vacuum ultraviolet (VUV) photons by streamers. Positive streamer heads are photon-driven and can trigger photochemical reactions, such as photolysis, within tens of nanosec-

onds upon impact with the interface. Short mean free paths, in the order of few micrometers, of UV and VUV photons in the liquid render them difficult to probe chemically and optically. However, given the high contribution of photoionization to the production of hydroxyl radicals, it is thus important to develop diagnostics methods to characterize UV-catalyzed processes at the interface.

To conclude, the 2-D discharge cell has emerged as an effective tool to study transport processes at the plasma-liquid interface by providing direct optical access to the region and reducing the dimensionality of plasma-liquid systems. This work hopes to serve as a basis for future studies that will further expand on our understanding of transport processes at the interface in 3-D plasma-liquid systems.

11.2 Future work

The 2-D framework for probing the plasma-liquid interface is amendable to various optical and chemical diagnostics methods not reported in this dissertation. The following describes a few open questions that can be pursued.

1) Spatiotemporally resolved optical emission spectroscopy: Optical emission spectroscopy is a widely used diagnostics methods to characterize the species present in the plasma region. Due to the short lifetime of hydroxyl radicals, it is often hard to accurately quantify its production and transport at the interface. Hydroxyl radicals have a detectable emission line at

309 nm [47], and can be readily measured in the gas phase. An Abel inversion method was previously reported for use in making spatially resolved measurements [158]. Combining the use of the Abel inversion method with the 2-D discharge cell can allow spatiotemporally resolved measurement of production of plasma-derived species in the bubble. Especially of interest is the production of hydroxyl radicals and singlet oxygen in the absence of gas phase oxygen, for example as a result of using rare gases in the bubble. This can provide insight into the contribution of electron impact reactions and ion charge exchange reactions at the interface, and the time evolution of gas composition in the bubble as a result of plasma ignition.

2) Fast ICCD imaging of streamers traveling between droplets: While a plasma-liquid system consists of a single air bubble injected in a thin layer of liquid was investigated in this dissertation, the 2-D discharge cell can be used to investigate other multiphase plasma-liquid systems as well. One such example is the study of streamer propagation between droplets. The misting of plasma-activated water is increasingly of interest for use in plasma food processing and agriculture [21, 22]. Thus it is important to understand the propagation of streamers between liquid surfaces and the penetration depth of various long-lived reactive species, such as hydrogen peroxide, into droplets. The precise control of plasma-derived reactivity into droplets and aerosols will be crucial to effectively control fertilizing and antimicrobial attributes of plasma activated water.

3) Parameter sweep of discharge conditions and resulting plasma-driven flow: Chapter. 9 showed that plasma-derived fluid flow depends highly on discharge conditions, such as effective relative permittivity of the discharge gap, excitation pulse width, excitation voltage, excitation frequency, gas type, liquid conductivity, and liquid composition (i.e. presence of surfactants). While we postulated that plasmas-driven flow is a result of temperature dependent Marangoni flow, a thorough parameter sweep of these conditions and the measurement of resulting plasma-driven flow will give valuable insight into the plasma-driven processes at the interface and mechanisms behind plasma-driven fluid flow.

4) Computational modeling of plasma-derived Marangoni effects: Marangoni effects can result from both temperature and concentration gradient. However, it is difficult to isolate the contribution of thermal effects and production of reactive species in experiments, both of which can result from plasmas coming into contact with a liquid surface. Thus computational models are attractive options for characterizing the contribution of these competing effects, and can be used to provide insights to the mechanisms of which plasma can drive Marangoni flow in the bulk liquid.

References

[1] Matthew J Traylor, Matthew J Pavlovich, Sharmin Karim, Pritha Hait, Yukinori Sakiyama, Douglas S Clark, and David B Graves. Long-term antibacterial efficacy of air plasma-activated water. *Journal of Physics D: Applied Physics*, 44(47):472001, 2011.

[2] Sarah N Gucker, John E Foster, and Maria C Garcia. An investigation of an underwater steam plasma discharge as alternative to air plasmas for water purification. *Plasma Sources Science and Technology*, 24(5):055005, 2015.

[3] John Foster, Bradley S Sommers, Sarah Nowak Gucker, Isaiah M Blankson, and Grigory Adamovsky. Perspectives on the interaction of plasmas with liquid water for water purification. *IEEE Transactions on Plasma Science*, 40(5):1311–1323, 2012.

[4] S Ognier, C Fourmond, S Bereza, and S Cavadias. Treatment of polluted water by gas-liquid discharge plasma reactor: Role of ozone and active species. *High Temperature Material Processes: An International Quarterly of High-Technology Plasma Processes*, 13(3-4), 2009.

[5] John E Foster. Plasma-based water purification: Challenges and prospects for the future. *Physics of Plasmas*, 24(5):055501, 2017.

[6] Susan B Watson, Carol Miller, George Arhonditsis, Gregory L Boyer, Wayne Carmichael, Murray N Charlton, Remegio Confesor, David C Depew, Tomas O Höök, Stuart A Ludsin, et al. The re-eutrophication of lake erie: Harmful algal blooms and hypoxia. *Harmful algae*, 56:44–66, 2016.

[7] Hans W Paerl and Jef Huisman. Blooms like it hot. *Science*, 320(5872):57–58, 2008.

[8] Ian R Falconer. Potential impact on human health of toxic cyanobacteria. *Phycologia*, 35(sup6):6–11, 1996.

[9] Geoffrey A Codd, Steven G Bell, Kunimitsu Kaya, Clive J Ward, Kenneth A Beattie, and James S Metcalf. Cyanobacterial toxins, exposure routes and human health. *European Journal of Phycology*, 34(4):405–415, 1999.

[10] J Rositano, BC Nicholson, and P Pieronne. Destruction of cyanobacterial toxins by ozone. *Ozone: Science & Engineering*, 20:223–238, 1998.

[11] Jiajia Fan, Lionel Ho, Peter Hobson, and Justin Brookes. Evaluating the effectiveness of copper sulphate, chlorine, potassium permanganate, hydrogen peroxide and ozone on cyanobacterial cell integrity. *Water research*, 47(14):5153–5164, 2013.

[12] John C Volin, Ferencz S Denes, Raymond A Young, and Scott MT Park. Modification of seed germination performance through cold plasma chemistry technology. *Crop science*, 40(6):1706–1718, 2000.

[13] Li Ling, Jiang Jiafeng, Li Jiangang, Shen Minchong, He Xin, Shao Hanliang, and Dong Yuanhua. Effects of cold plasma treatment on seed germination and seedling growth of soybean. *Scientific reports*, 4:5859, 2014.

[14] Dayonna P Park, Kevin Davis, Samid Gilani, Christal-Anne Alonzo, Danil Dobrynin, Gary Friedman, Alexander Fridman, Alexander Rabinovich, and Gregory Fridman. Reactive nitrogen species produced in water by non-equilibrium plasma increase plant growth rate and nutritional yield. *Current Applied Physics*, 13:S19–S29, 2013.

[15] Sang Hye Ji, Taesoo Kim, Kamonporn Panngom, Young June Hong, Anchalee Pengkit, Dae Hoon Park, Min Ho Kang, Sang Hark Lee, Jun Sup Im, Ju Sung Kim, et al. Assessment of the effects of nitrogen plasma and plasma-generated nitric oxide on early development of coriandum sativum. *Plasma Processes and Polymers*, 12(10):1164–1173, 2015.

[16] Wladimir An, Kurt Baumung, and Hansjoachim Bluhm. Underwater streamer propagation analyzed from detailed measurements of pressure release. *Journal of applied physics*, 101(5):053302, 2007.

[17] Sander Bekeschus, Anke Schmidt, Klaus-Dieter Weltmann, and Thomas von Woedtke. The plasma jet kinpen–a powerful tool for wound healing. *Clinical Plasma Medicine*, 4(1):19–28, 2016.

[18] Gregory Fridman, Alexey Shereshevsky, Monika M Jost, Ari D Brooks, Alexander Fridman, Alexander Gutsol, Victor Vasilets, and Gary Friedman. Floating electrode

dielectric barrier discharge plasma in air promoting apoptotic behavior in melanoma skin cancer cell lines. *Plasma Chemistry and Plasma Processing*, 27(2):163–176, 2007.

[19] Kamonporn Panngom, Ku Youn Baik, Min-Kyung Nam, JH Han, H Rhim, and EH Choi. Preferential killing of human lung cancer cell lines with mitochondrial dysfunction by nonthermal dielectric barrier discharge plasma. *Cell death & disease*, 4(5):e642, 2013.

[20] KG Kostov, V Rocha, CY Koga-Ito, BM Matos, MA Algatti, Roberto Yzumi Honda, ME Kayama, and Rogério Pinto Mota. Bacterial sterilization by a dielectric barrier discharge (dbd) in air. *Surface and Coatings Technology*, 204(18-19):2954–2959, 2010.

[21] Yunbin Jiang, Kimberly Sokorai, Georgios Pyrgiotakis, Philip Demokritou, Xihong Li, Sudarsan Mukhopadhyay, Tony Jin, and Xuetong Fan. Cold plasma-activated hydrogen peroxide aerosol inactivates escherichia coli o157: H7, salmonella typhimurium, and listeria innocua and maintains quality of grape tomato, spinach and cantaloupe. *International journal of food microbiology*, 249:53–60, 2017.

[22] R Burlica, RG Grim, K-Y Shih, D Balkwill, and BR Locke. Bacteria inactivation using low power pulsed gliding arc discharges with water spray. *Plasma Processes and Polymers*, 7(8):640–649, 2010.

[23] Ayman A Abdelaziz, Tatsuo Ishijima, and Chedly Tizaoui. Development and characterization of a wire-plate air bubbling plasma for wastewater treatment using nanosecond pulsed high voltage. *Journal of Applied Physics*, 124(5):053302, 2018.

[24] Seth A Norberg, Wei Tian, Eric Johnsen, and Mark J Kushner. Atmospheric pressure plasma jets interacting with liquid covered tissue: touching and not-touching the liquid. *Journal of Physics D: Applied Physics*, 47(47):475203, 2014.

[25] H Taghvaei, VSSK Kondeti, and Peter J Bruggeman. Decomposition of crystal violet by an atmospheric pressure rf plasma jet: The role of radicals, ozone, near-interfacial reactions and convective transport. *Plasma Chemistry and Plasma Processing*, pages 1–21, 2019.

[26] Ulrich Kogelschatz. Dielectric-barrier discharges: their history, discharge physics, and industrial applications. *Plasma chemistry and plasma processing*, 23(1):1–46, 2003.

[27] Takashi Saito, Taichi Sugai, and Yasushi Minamitani. Investigation of quantity of active species generated by pulsed streamer discharges among electrodes with droplets for water treatment. In *2012 IEEE International Power Modulator and High Voltage Conference (IPMHVC)*, pages 500–503. IEEE, 2012.

[28] PJ Bruggeman, CA Leys, and JA Vierendeels. Electrical breakdown of a bubble in a water-filled capillary. *Journal of Applied Physics*, 99:116101, 2006.

[29] Natalia Yu Babaeva and Mark J Kushner. Structure of positive streamers inside gaseous bubbles immersed in liquids. *Journal of Physics D: Applied Physics*, 42(13):132003, 2009.

[30] Kunihide Tachibana, Yuki Takekata, Yusuke Mizumoto, Hideki Motomura, and Masafumi Jinno. Analysis of a pulsed discharge within single bubbles in water under synchronized conditions. *Plasma Sources Science and Technology*, 20(3):034005, 2011.

[31] BS Sommers and JE Foster. Plasma formation in underwater gas bubbles. *Plasma Sources Science and Technology*, 23(1):015020, 2014.

[32] Sarah N Gucker, Bradley S Sommers, and John E Foster. Plasma production in isolated bubbles. *IEEE Transactions on Plasma Science*, 42(10):2636–2637, 2014.

[33] Ahmad Hamdan and Min Suk Cha. Ignition modes of nanosecond discharge with bubbles in distilled water. *Journal of Physics D: Applied Physics*, 48(40):405206, 2015.

[34] Katrin R Siefermann, Yaxing Liu, Evgeny Lugovoy, Oliver Link, Manfred Faubel, Udo Buck, Bernd Winter, and Bernd Abel. Binding energies, lifetimes and implications of bulk and interface solvated electrons in water. *Nature chemistry*, 2(4):274, 2010.

[35] B Abel, Ua Buck, AL Sobolewski, and W Domcke. On the nature and signatures of the solvated electron in water. *Physical Chemistry Chemical Physics*, 14(1):22–34, 2012.

[36] U Schindewolf. Formation and properties of solvated electrons. *Angewandte Chemie International Edition in English*, 7(3):190–203, 1968.

[37] Paul Rumbach, David M Bartels, and David B Go. The penetration and concentration of solvated electrons and hydroxyl radicals at a plasma-liquid interface. *Plasma Sources Science and Technology*, 27(11):115013, nov 2018.

[38] Petr Lukes, Monica Magureanu, and Vasile I Pârvulescu. *Plasma chemistry and catalysis in gases and liquids*. Wiley Online Library, 2012.

[39] Yudai Minagawa, Naoki Shirai, Satoshi Uchida, and Fumiyoshi Tochikubo. Analysis of effect of ion irradiation to liquid surface on water molecule kinetics by classical molecular dynamics simulation. *Japanese Journal of Applied Physics*, 53(1):010210, 2013.

[40] Amanda M Lietz and Mark J Kushner. Air plasma treatment of liquid covered tissue: long timescale chemistry. *Journal of Physics D: Applied Physics*, 49(42):425204, 2016.

[41] Juliusz A Kruszelnicki, Amanda M Lietz, and Mark J Kushner. Atmospheric pressure plasma activation of water droplets. *Journal of Physics D: Applied Physics*, 2019.

[42] Bruce R Locke and Selma Mededovic Thagard. Analysis and review of chemical reactions and transport processes in pulsed electrical discharge plasma formed directly in liquid water. *Plasma Chemistry and Plasma Processing*, 32(5):875–917, 2012.

[43] Tetsuji Oda. Non-thermal plasma processing for environmental protection: decomposition of dilute vocs in air. *Journal of electrostatics*, 57(3-4):293–311, 2003.

[44] M Tezuka and M Iwasaki. Liquid-phase reactions induced by gaseous plasma. decomposition of benzoic acids in aqueous solution. *Plasmas & Ions*, 2(1):23–26, 1999.

[45] Hiroshi Katayama, Hiroyuki Honma, Naoyuki Nakagawara, and Koichi Yasuoka. Decomposition of persistent organics in water using a gas–liquid two-phase flow plasma reactor. *IEEE Transactions on Plasma Science*, 37(6):897–904, 2009.

[46] Edelsys Codorniu-Hern□ndez and Peter G Kusalik. Mobility mechanism of hydroxyl radicals in aqueous solution via hydrogen transfer. *Journal of the American Chemical Society*, 134(1):532–538, 2011.

[47] Pankaj Attri, Yong Hee Kim, Dae Hoon Park, Ji Hoon Park, Young J Hong, Han Sup Uhm, Kyoung-Nam Kim, Alexander Fridman, and Eun Ha Choi. Generation mechanism of hydroxyl radical species and its lifetime prediction during the plasma-initiated ultraviolet (uv) photolysis. *Scientific reports*, 5:9332, 2015.

[48] Anto Tri Sugiarto, Shunsuke Ito, Takayuki Ohshima, Masayuki Sato, and Jan D Skalny. Oxidative decoloration of dyes by pulsed discharge plasma in water. *Journal of Electrostatics*, 58(1-2):135–145, 2003.

[49] William H Glaze, Joon-Wun Kang, and Douglas H Chapin. The chemistry of water treatment processes involving ozone, hydrogen peroxide and ultraviolet radiation. *Ozone: Science & Engineering*, 9:335–352, 1987.

[50] Henry Drysdale Dakin. On the use of certain antiseptic substances in the treatment of infected wounds. *British medical journal*, 2(2852):318, 1915.

[51] Petr Lukes, Austin T Appleton, and Bruce R Locke. Hydrogen peroxide and ozone formation in hybrid gas-liquid electrical discharge reactors. *IEEE Transactions on Industry Applications*, 40(1):60–67, 2004.

[52] William H Glaze. Drinking-water treatment with ozone. *Environmental science & technology*, 21(3):224–230, 1987.

[53] Vand Camel and A Bermond. The use of ozone and associated oxidation processes in drinking water treatment. *Water research*, 32(11):3208–3222, 1998.

[54] Rip G Rice, C Michael Robson, G Wade Miller, and Archibald G Hill. Uses of ozone in drinking water treatment. *Journal-American Water Works Association*, 73(1):44–57, 1981.

[55] G Neretti, M Taglioli, G Colonna, and C Borghi. Characterization of a dielectric barrier discharge in contact with liquid and producing a plasma activated water. *Plasma Sources Science and Technology*, 26(1), 2017.

[56] K Oehmigen, M Hähnel, R Brandenburg, Ch Wilke, K-D Weltmann, and Th Von Woedtke. The role of acidification for antimicrobial activity of atmospheric pressure plasma in liquids. *Plasma Processes and Polymers*, 7(3-4):250–257, 2010.

[57] Monica Magureanu, Corina Bradu, Daniela Piroi, Nicolae Bogdan Mandache, and Vasile Parvulescu. Pulsed corona discharge for degradation of methylene blue in water. *Plasma Chemistry and Plasma Processing*, 33(1):51–64, 2013.

[58] Wei Tian and Mark J Kushner. Atmospheric pressure dielectric barrier discharges interacting with liquid covered tissue. *Journal of Physics D: Applied Physics*, 47(16):165201, 2014.

[59] PJ Bruggeman, Mark J Kushner, Bruce R Locke, Johannes GE Gardeniers, WG Graham, David B Graves, RCHM Hofman-Caris, Dragana Maric, Jonathan P Reid, Elisa Ceriani, et al. Plasma–liquid interactions: a review and roadmap. *Plasma sources science and technology*, 25(5):053002, 2016.

[60] J Ch Chang, Susan F Ossoff, David C Lobe, Mark H Dorfman, Constance M Dumais, Robert G Qualls, and J Donald Johnson. Uv inactivation of pathogenic and indicator microorganisms. *Appl. Environ. Microbiol.*, 49(6):1361–1365, 1985.

[61] John E. Foster. Plasma-based water purification: Challenges and prospects for the future. *Physics of Plasmas*, 24:055501, 2017.

[62] Keiichi Kondo and Nobuaki Ikuta. Spatio-temporal gas temperature rise in repetitive positive streamer corona in air. *Journal of the Physical Society of Japan*, 59(9):3203–3216, 1990.

[63] Doug Breden and LL Raja. Gas heating effects in a nanosecond-pulse streamer discharge interacting with a supersonic $o_2 - h_2$ flow. *IEEE Transactions on Plasma Science*, 39(11):2250–2251, 2011.

[64] John Zeleny. Instability of electrified liquid surfaces. *Phys. Rev.*, 10:1–6, Jul 1917.

[65] Geoffrey Ingram Taylor. Disintegration of water drops in an electric field. *Proceedings of the Royal Society of London. Series A. Mathematical and Physical Sciences*, 280(1382):383–397, 1964.

[66] Peter Bruggeman, Leigh Graham, Joris Degroote, Jan Vierendeels, and Christophe Leys. Water surface deformation in strong electrical fields and its influence on electrical breakdown in a metal pin–water electrode system. *Journal of Physics D: Applied Physics*, 40(16):4779, 2007.

[67] Bradley S Sommers, John E Foster, N Yu Babaeva, and Mark J Kushner. Observations of electric discharge streamer propagation and capillary oscillations on the surface of air bubbles in water. *Journal of Physics D: Applied Physics*, 44(8):082001, 2011.

[68] BS Sommers and JE Foster. Nonlinear oscillations of gas bubbles submerged in water: implications for plasma breakdown. *Journal Physics D: Applied Physics*, 45:415203, 2012.

[69] Selma Mededovic Thagard, Gunnar R Stratton, Mikhail Vasilev, Patrick Conlon, and Douglas Bohl. An experimental investigation of the liquid flow induced by a pulsed electrical discharge plasma. *Plasma Chemistry and Plasma Processing*, 38(4):719–741, 2018.

[70] Christian WJ Berendsen, Eddie M van Veldhuizen, Gerrit MW Kroesen, and Anton A Darhuber. Marangoni flows induced by atmospheric-pressure plasma jets. *Journal of Physics D: Applied Physics*, 48(2):025203, 2014.

[71] Tetsuji Shimizu, Yutaka Iwafuchi, Gregor E Morfill, and Takehiko Sato. Formation of thermal flow fields and chemical transport in air and water by atmospheric plasma. *New Journal of Physics*, 13(5):053025, 2011.

[72] Peter Bruggeman, Tiny Verreycken, Manuel A Gonzalez, James L Walsh, Michael G Kong, Christophe Leys, and Daan C Schram. Optical emission spectroscopy as a diagnostic for plasmas in liquids: opportunities and pitfalls. *Journal of Physics D: Applied Physics*, 43(12):124005, 2010.

[73] Peter Bruggeman, Christophe Leys, and Jan Vierendeels. Experimental investigation of dc electrical breakdown of long vapour bubbles in capillaries. *Journal of Physics D: Applied Physics*, 40(7):1937, 2007.

[74] Toshiyuki Kawasaki, Kota Kawano, Hiroshi Mizoguchi, Yuto Yano, Keisuke Yamashita, Miho Sakai, Takako Shimizu, Giichiro Uchida, Kazunori Koga, and Masaharu Shiratani. Visualization of the distribution of oxidizing substances in an atmospheric pressure plasma jet. *IEEE Transactions on Plasma Science*, 42(10):2482–2483, 2014.

[75] S Zhang, A Sobota, EM Van Veldhuizen, and Peter J Bruggeman. Gas flow characteristics of a time modulated appj: the effect of gas heating on flow dynamics. *Journal of Physics D: Applied Physics*, 48(1):015203, 2014.

[76] Katrin Oehmigen, Tomáš Hoder, Christian Wilke, Ronny Brandenburg, Marcel Hahnel, Klaus-Dieter Weltmann, and Thomas von Woedtke. Volume effects of atmospheric-pressure plasma in liquids. *IEEE Transactions on Plasma Science*, 39(11):2646–2647, 2011.

[77] Philip Geoffrey Saffman and Geoffrey Ingram Taylor. The penetration of a fluid into a porous medium or hele-shaw cell containing a more viscous liquid. *Proceedings of the Royal Society of London. Series A. Mathematical and Physical Sciences*, 245(1242):312–329, 1958.

[78] John E Foster, Brandon Weatherford, Eric Gillman, and Benjamin Yee. Underwater operation of a dbd plasma jet. *Plasma Sources Science and Technology*, 19(2):025001, 2010.

[79] ANSYS. ANSYS Maxwell. https://www.ansys.com/products/electronics/ansys-maxwell.

[80] Jan CT Kwak, Jan AA Ketelaar, PPE Maenaut, and AJH Boerboom. Electrical mobilities of lithium-6, calcium-45, and nitrate ions in liquid mixtures of lithium nitrate and calcium nitrate. *The Journal of Physical Chemistry*, 74(19):3449–3451, 1970.

[81] Matthew J Traylor, Matthew J Pavlovich, Sharmin Karim, Pritha Hait, Yukinori Sakiyama, Douglas S Clark, and David B Graves. Long-term antibacterial efficacy of air plasma-activated water. *Journal of Physics D: Applied Physics*, 44(47):472001, 2011.

[82] Zoran Falkenstein and John J Coogan. The development of a silent discharge-driven excimer uv light source. *Journal of Physics D: Applied Physics*, 30(19):2704, 1997.

[83] Seiji Samukawa, Masaru Hori, Shahid Rauf, Kunihide Tachibana, Peter Bruggeman, Gerrit Kroesen, J Christopher Whitehead, Anthony B Murphy, Alexander F Gutsol, Svetlana Starikovskaia, et al. The 2012 plasma roadmap. *Journal of Physics D: Applied Physics*, 45(25):253001, 2012.

[84] Sugata P Tan and Mohammad Piri. Modeling the solubility of nitrogen dioxide in water using perturbed-chain statistical associating fluid theory. *Industrial & Engineering Chemistry Research*, 52(45):16032–16043, 2013.

[85] P Lukes, E Dolezalova, I Sisrova, and M Clupek. Aqueous-phase chemistry and bactericidal effects from an air discharge plasma in contact with water: evidence for the formation of peroxynitrite through a pseudo-second-order post-discharge reaction of h202 and hno2. *Plasma Sources Science and Technology*, 23(1):015019, 2014.

[86] ZC Liu, DX Liu, C Chen, D Li, AJ Yang, MZ Rong, HL Chen, and MG Kong. Physicochemical processes in the indirect interaction between surface air plasma and deionized water. *Journal of Physics D: Applied Physics*, 48(49):495201, 2015.

[87] Sarah N Gucker, John E Foster, and Maria C Garcia. An investigation of an underwater steam plasma discharge as alternative to air plasmas for water purification. *Plasma Sources Science and Technology*, 24(5):055005, 2015.

[88] Martin Böckmann and Stefan C Müller. Growth rates of the buoyancy-driven instability of an autocatalytic reaction front in a narrow cell. *Physical review letters*, 85(12):2506, 2000.

[89] Bradley S Sommers, John E Foster, N Yu Babaeva, and Mark J Kushner. Observations of electric discharge streamer propagation and capillary oscillations on the surface of air bubbles in water. *Journal of Physics D: Applied Physics*, 44(8):082001, 2011.

[90] KJ Ptasinski and PJAM Kerkhof. Electric field driven separations: Phenomena and applications. *Separation science and technology*, 27(8-9):995–1021, 1992.

[91] Tetsuji Shimizu, Yutaka Iwafuchi, Gregor E Morfill, and Takehiko Sato. Formation of thermal flow fields and chemical transport in air and water by atmospheric plasma. *New Journal of Physics*, 13(5):053025, 2011.

[92] Jasper FM Van Rens, Jan T Schoof, Fanny C Ummelen, Daan C Van Vugt, Peter J Bruggeman, and EM Van Veldhuizen. Induced liquid phase flow by rf ar cold atmospheric pressure plasma jet. *IEEE Transactions on Plasma Science*, 42(10):2622–2623, 2014.

[93] Geoffrey Ingram Taylor. The force exerted by an electric field on a long cylindrical conductor. *Proceedings of the Royal Society of London. Series A. Mathematical and Physical Sciences*, 291(1425):145–158, 1966.

[94] Wei Tian and Mark J Kushner. Atmospheric pressure dielectric barrier discharges interacting with liquid covered tissue. *Journal of Physics D: Applied Physics*, 47(16):165201, 2014.

[95] Heinz Bader and Jürg Hoigné. Determination of ozone in water by the indigo method. *Water Research*, 15:449–456, 1981.

[96] Joseph M Rutkowski, Lizzie Y Santiago, Abdellaziz Ben-Jebria, and James S Ultman. Development of an assay for ozone-specific antioxidant capacity. *Inhalation toxicology*, 15(13):1369–1385, 2003.

[97] Chung-Fan Chiou, Benito J Mariñas, and Jeffrey Q Adams. Modified indigo method for gaseous and aqueous ozone analyses. *Ozone: science & engineering*, 17(3):329–344, 1995.

[98] Michael R Straka, Gilbert Gordon, and Gilbert E Pacey. Residual aqueous ozone determination by gas diffusion flow injection analysis. *Analytical Chemistry*, 57(9):1799–1803, 1985.

[99] D Kuvshinov, A Siswanto, J Lozano-Parada, and WB Zimmerman. Efficient compact micro dbd plasma reactor for ozone generation for industrial application in liquid and gas phase systems. *World Acad. Sci. Eng. Technol*, 8:80–83, 2014.

[100] J Hoigne and H Bader. The role of hydroxyl radical reactions in ozonation processes in aqueous solutions. *Water research*, 10(5):377–386, 1976.

[101] M Anbar, D Meyerstein, and P Neta. The reactivity of aromatic compounds toward hydroxyl radicals. *The Journal of Physical Chemistry*, 70(8):2660–2662, 1966.

[102] M Anbar, D Meyerstein, and P Neta. Reactivity of aliphatic compounds towards hydroxyl radicals. *Journal of the Chemical Society B: Physical Organic*, pages 742–747, 1966.

[103] Janis Lai and John E Foster. 2-d bubble test cell for the study of interactions at the plasma-liquid interface. *IEEE Transactions on Plasma Science*, 44:1127–1136, 2016.

[104] howpublished = `https://imagej.nih.gov/ij/` National Institutes of Health, title = ImageJ.

[105] Janis Lai, Victor Petrov, and John E Foster. Understanding plasma?liquid interface instabilities using particle image velocimetry and shadowgraphy imaging methods. *IEEE Transactions on Plasma Science*, 49:875–881, 2018.

[106] LaVision. DaVis 8.2.2. `https://www.lavision.de/en/products/davis-software/`.

[107] A Miniewicz, S Bartkiewicz, H Orlikowska, and K Dradrach. Marangoni effect visualized in two-dimensions optical tweezers for gas bubbles. *Scientific reports*, 6:34787, 2016.

[108] Toshiyuki Kawasaki, Wataru Eto, Masaki Hamada, Yasutaka Wakabayashi, Yasufumi Abe, and Keisuke Kihara. Detection of reactive oxygen species supplied into the water bottom by atmospheric non-thermal plasma jet using iodine-starch reaction. *Japanese Journal of Applied Physics*, 54(8):086201, 2015.

[109] Tomáš Hoder, Mirko Černák, Jean Paillol, Detlef Loffhagen, and Ronny Brandenburg. High-resolution measurements of the electric field at the streamer arrival to the cathode: A unification of the streamer-initiated gas-breakdown mechanism. *Physical Review E*, 86(5):055401, 2012.

[110] Zdenek Bonaventura, Anne Bourdon, Sébastien Célestin, and VP Pasko. Electric field determination in streamer discharges in air at atmospheric pressure. *Plasma Sources Science and Technology*, 20(3):035012, 2011.

[111] Stefan Maehlmann and Demetrios T Papageorgiou. Numerical study of electric field effects on the deformation of two-dimensional liquid drops in simple shear flow at arbitrary reynolds number. *Journal of Fluid Mechanics*, 626:367–393, 2009.

[112] PW Hammerton and Andrew P Bassom. The effect of a normal electric field on wave propagation on a fluid film. *Physics of Fluids*, 26(1):012107, 2014.

[113] Yohan Seepersad, Mikhail Pekker, Mikhail N Shneider, Danil Dobrynin, and Alexander Fridman. On the electrostrictive mechanism of nanosecond-pulsed breakdown in liquid phase. *Journal of Physics D: Applied Physics*, 46(16):162001, 2013.

[114] Akira Miura and PL Pritchett. Nonlocal stability analysis of the mhd kelvin-helmholtz instability in a compressible plasma. *Journal of Geophysical Research: Space Physics*, 87(A9):7431–7444, 1982.

[115] Bradley S Sommers, John E Foster, N Yu Babaeva, and Mark J Kushner. Observations of electric discharge streamer propagation and capillary oscillations on the surface of air bubbles in water. *Journal of Physics D: Applied Physics*, 44:082001, 2011.

[116] Jie Xu and Daniel Attinger. Acoustic excitation of superharmonic capillary waves on a meniscus in a planar microgeometry. *Physics of Fluids*, 19(10):108107, 2007.

[117] John E Foster, Selman Mujovic, Joseph Groele, and Isaiah M Blankson. Towards high throughput plasma based water purifiers: design considerations and the pathway towards practical application. *Journal of Physics D: Applied Physics*, 51:293001, 2018.

[118] Michael Keidar, Dayun Yan, Isak I Beilis, Barry Trink, and Jonathan H Sherman. Plasmas for treating cancer: opportunities for adaptive and self-adaptive approaches. *Trends in biotechnology*, 36(6):586–593, 2018.

[119] Michael Faraday. Xvii. on a peculiar class of acoustical figures; and on certain forms assumed by groups of particles upon vibrating elastic surfaces. *Philosophical Transactions of the Royal Society of London*, 121:299–340, 1831.

[120] Lord Rayleigh. Vii. on the crispations of fluid resting upon a vibrating support. *The London, Edinburgh, and Dublin Philosophical Magazine and Journal of Science*, 16:50–58, 1883.

[121] Kern E Kenyon. Capillary waves understood by an elementary method. *Journal of Oceanography*, 54(4):343–346, 1998.

[122] Fabian Denner. Frequency dispersion of small-amplitude capillary waves in viscous fluids. *Physical Review E*, 94:023110, 2016.

[123] Andor, Oxford Instruments Group. Solis Software. `https://www.andor.com/scientific-software/solis-software`.

[124] Vitaly Petrishchev, Sergey Leonov, and Igor V Adamovich. Studies of nanosecond pulse surface ionization wave discharges over solid and liquid dielectric surfaces. *Plasma Sources Science and Technology*, 23(6):065022, 2014.

[125] IV Lisitsyn, H Nomlyama, S Katsuki, and H Akiyama. Thermal processes in a streamer discharge in water. *IEEE Transactions on Dielectrics and Electrical Insulation*, 6(3):351–356, 1999.

[126] NA Popov. Formation and development of a leader channel in air. *Plasma Physics Reports*, 29(8):695–708, 2003.

[127] LaVision. DaVis 8.4.0. `https://www.lavision.de/en/products/davis-software/`.

[128] Georg Bauer. Signal amplification by tumor cells: Clue to the understanding of the antitumor effects of cold atmospheric plasma and plasma-activated medium. *IEEE Transactions on Radiation and Plasma Medical Sciences*, 2:87–98, 2018.

[129] Sander Bekeschus, Anne Mueller, Vandana Miller, Udo Gaipl, and Klaus-Dieter Weltmann. Physical plasma elicits immunogenic cancer cell death and mitochondrial singlet oxygen. *IEEE Transactions on Radiation and Plasma Medical Sciences*, 2(2):138–146, 2018.

[130] Zhitong Chen, Li Lin, Eda Gjika, Xiaoqian Cheng, Jerome Canady, and Michael Keidar. Selective treatment of pancreatic cancer cells by plasma-activated saline solutions. *IEEE Transactions on Radiation and Plasma Medical Sciences*, 2(2):116–120, 2018.

[131] US EPA. Cyanobacteria and cyanotoxins: Information for drinking water systems. 2014.

[132] Daniel J Conley, Hans W Paerl, Robert W Howarth, Donald F Boesch, Sybil P Seitzinger, Karl E Havens, Christiane Lancelot, and Gene E Likens. Controlling eutrophication: nitrogen and phosphorus, 2009.

[133] Maria G Antoniou, Armah A De La Cruz, and Dionysios D Dionysiou. Cyanotoxins: new generation of water contaminants, 2005.

[134] Geneva World Health Organization. Cyanobacterial toxins: Microcystin-lr in drinking-water. *Guidelines for drinking-water quality*, 2003.

[135] Wayne W Carmichael. The toxins of cyanobacteria. *Scientific American*, 270(1):78–86, 1994.

[136] Wayne W Carmichael, SM Azevedo, Ji Si An, RJ Molica, Elise M Jochimsen, Sharon Lau, Kenneth L Rinehart, Glen R Shaw, and Geoff K Eaglesham. Human fatalities from cyanobacteria: chemical and biological evidence for cyanotoxins. *Environmental health perspectives*, 109(7):663–668, 2001.

[137] National Cancer Institute. Nci nomination: Blue-green algae. *National Toxicology Program, U.S. Department of Health and Human Services*, 2000.

[138] John R Kasich, Governor Mary Taylor, Lt Governor, Craig W Butler, and Director?Ohio Environmental. Public water system harmful algal bloom response strategy. *Ohio Environmental Protection Agency*, 2014.

[139] US EPA. 2015 drinking water health advisories for two cyanobacterial toxins. 2015.

[140] Wansong Zong, Feng Sun, Haiyan Pei, Wenrong Hu, and Ruoting Pei. Microcystin-associated disinfection by-products: The real and non-negligible risk to drinking water subject to chlorination. *Chemical Engineering Journal*, 279:498–506, 2015.

[141] Ian R Falconer, Maria TC Runnegar, Tom Buckley, Van L Huyn, and Peter Bradshaw. Using activated carbon to remove toxicity from drinking water containing cyanobacterial blooms. *Journal-American Water Works Association*, 81(2):102–105, 1989.

[142] Lionel Ho, Anne-Laure Gaudieux, Stella Fanok, Gayle Newcombe, and Andrew R Humpage. Bacterial degradation of microcystin toxins in drinking water eliminates their toxicity. *Toxicon*, 50(3):438–441, 2007.

[143] Winn-Jung Huang, Bai-Ling Cheng, and Yung-Ling Cheng. Adsorption of microcystin-lr by three types of activated carbon. *Journal of Hazardous Materials*, 141(1):115–122, 2007.

[144] Lionel Ho, Daniel Hoefel, Christopher P Saint, and Gayle Newcombe. Isolation and identification of a novel microcystin-degrading bacterium from a biological sand filter. *Water research*, 41(20):4685–4695, 2007.

[145] Haixiang Wang, Lionel Ho, David M Lewis, Justin D Brookes, and Gayle Newcombe. Discriminating and assessing adsorption and biodegradation removal mechanisms during granular activated carbon filtration of microcystin toxins. *Water research*, 41(18):4262–4270, 2007.

[146] JH Carey. An introduction to advanced oxidation processes (aop) for destruction of organics in wastewater. *Water Quality Research Journal*, 27(1):1–22, 1992.

[147] I Oller, S Malato, and JAb Sánchez-Pérez. Combination of advanced oxidation processes and biological treatments for wastewater decontamination?a review. *Science of the total environment*, 409(20):4141–4166, 2011.

[148] BA Wols and CHM Hofman-Caris. Review of photochemical reaction constants of organic micropollutants required for uv advanced oxidation processes in water. *Water research*, 46(9):2815–2827, 2012.

[149] Fares Al Momani, Daniel W Smith, and Mohamed Gamal El-Din. Degradation of cyanobacteria toxin by advanced oxidation processes. *Journal of hazardous materials*, 150(2):238–249, 2008.

[150] Virender K Sharma, Theodoros M Triantis, Maria G Antoniou, Xuexiang He, Miguel Pelaez, Changseok Han, Weihua Song, Kevin E O?Shea, A Armah, Triantafyllos Kaloudis, et al. Destruction of microcystins by conventional and advanced oxidation processes: a review. *Separation and Purification Technology*, 91:3–17, 2012.

[151] Weihua Song, Tielian Xu, William J Cooper, Dionysios D Dionysiou, Armah A de la Cruz, and Kevin E O ?Shea. Radiolysis studies on the destruction of microcystin-lr in aqueous solution by hydroxyl radicals. *Environmental science & technology*, 43(5):1487–1492, 2009.

[152] Hong Zhang, Qing Huang, Zhigang Ke, Linfang Yang, Xiangqin Wang, and Zengliang Yu. Degradation of microcystin-lr in water by glow discharge plasma

oxidation at the gas–solution interface and its safety evaluation. *Water research*, 46(19):6554–6562, 2012.

[153] John E Foster, Brandon Weatherford, Eric Gillman, and Benjamin Yee. Underwater operation of a dbd plasma jet. *Plasma Sources Science and Technology*, 19(2):025001, 2010.

[154] Cayman Chemical. Microcystin-lr.

[155] Sandra Perez and Diana S Aga. Recent advances in the sample preparation, liquid chromatography tandem mass spectrometric analysis and environmental fate of microcystins in water. *TrAC Trends in Analytical Chemistry*, 24(7):658–670, 2005.

[156] Iain Liu, Linda A Lawton, and Peter KJ Robertson. Mechanistic studies of the photocatalytic oxidation of microcystin-lr: an investigation of byproducts of the decomposition process. *Environmental science & technology*, 37(14):3214–3219, 2003.

[157] I Talinli and GK Anderson. Interference of hydrogen peroxide on the standard cod test. *Water research*, 26(1):107–110, 1992.

[158] R Alvarez, A Rodero, and MC Quintero. An abel inversion method for radially resolved measurements in the axial injection torch. *Spectrochimica Acta Part B: Atomic Spectroscopy*, 57(11):1665–1680, 2002.